Universidade do Minho
Escola de Engenharia

Gonçalo Garrett Miranda Ribeiro Barbosa

Surface functionalization with anti-bacterial and bioactive compounds using hybrid techniques (subtractive and addictive) via laser for the improvement of knee prostheses properties.

october 2022

Surface functionalization with anti-bacterial and bioactive compounds using hybrid techniques (subtractive and addictive) via laser for the improvement of knee prostheses properties.

Gonçalo Barbosa

UMinho | 2022

Universidade do Minho
Escola de Engenharia

Gonçalo Garrett Miranda Ribeiro Barbosa

Surface functionalization with antibacterial and bioactive compounds using hybrid techniques (subtractive and addictive) via laser for the improvement of knee prostheses properties

Master's Dissertation
Integrated master's in biomedical engineering
Biomaterials, Rehabilitation and Biomechanics

Work developed under supervision of
Professor Doctor Óscar Samuel Novais Carvalho
Professor Doctor Filipe Samuel Correia Pereira da Silva
Professor Doctor Joana Rita Oliveira Faria Marques

october 2022

COPYRIGHT AND CONDITIONS OF USE OF THE WORK BY THIRD PARTIES

This is an academic work that may be used by third parties provided that internationally accepted rules and good practices regarding copyright and related rights are respected.

Therefore, this work may be used under the terms of the license set out below.

If the user needs permission to use the work under conditions not foreseen in the license indicated, he/she should contact the author, through RepositóriUM of the University of Minho.

Licence granted to users of this work

Attribution-NonCommercial-ShareAlike

CC BY-NC-SA

https://creativecommons.org/licenses/by-nc-sa/4.0/

STATEMENT OF INTEGRITY

I hereby declare having conducted this academic work with integrity. I confirm that I have not used plagiarism or any form of undue use of information or falsification of results along the process leading to its elaboration.

I further declare that I have fully acknowledged the Code of Ethical Conduct of the University of Minho.

ACKNOWLEDGMENTS

This dissertation represents the end of a long cycle, not only from an academic point of view but also from a personal standpoint. There were ups and downs in this journey, and I would like to express my gratitude to all the people that helped me, in one way or another, when times were hard. Thus...

To my supervisor, Professor Óscar Carvalho, for all the words of wisdom, enthusiasm, guidance and support transmitted throughout this dissertation. A big thank you!

To my co-supervisor, Diana Faria, for the friendliness, patience, dedication, experience and overall crucial help provided during this work, always available when needed. A big thank you!

To Professor Filipe Samuel for the opportunity to do this work, and for the valuable suggestions shared. A big thank you for the trust provided.

To professor Joana Marques and PhD students Beatriz Fernandes and Mariana Cruz, for all the help provided in the realization of the cell viability tests.

To professor Sérgio Carvalho, for the counselling and assistance provided during the friction tests.

To technician Sónia Gonçalves, from the textile department, for the friendliness and availability provided during the wettability measurements.

A big thank you to all the collaborators in the Microfabrication and Integrated Systems Laboratory for all the help, good mood, availability and encouragement demonstrated.

To my girlfriend, Carolina Silva, for all the love, advice and constant support shown from the very beginning. I can always count on you.

To all my university friends, who were always there for me during this journey. They were fundamental in the initial times of adaptation to a new reality, and were a constant presence in all the moments, good and bad, of my academic life. Thank you, you have never let me down.

And above all, my unconditional gratitude to my family, for all the support, belief and personal values transmitted, as well as the opportunity to study and grow as a person. A thank you is never enough for all you have done for me, and I hope going forward I can make you proud.

ABSTRACT

Knee arthroplasty is a surgical procedure that consists in the removal of the entirety or part of the knee joint, extracting damaged cartilage and replacing it with a prosthesis or implant. Thus, knee prostheses are devices that replace the function of the joint. They have different components, each with a specific function and composed of different materials. However, their longevity is still relatively short, about 15 years, and the use of materials with inadequate mechanical properties can lead to the appearance of undesirable phenomena that contribute to an even earlier prosthesis removal.

That being said, it is important to find solutions to improve not only the functionality of these implants, but also their longevity. Therefore, this work focuses on the modification of materials typically used in these implants, such as zirconia and titanium, through a hybrid (subtractive and additive) laser processing technique. Patterns were thus created on the surface of the materials, and bioactive compounds (hydroxyapatite and mineral trioxide aggregate) were incorporated into them, in order to improve the bioactivity and consequent functionality and longevity of the knee prostheses.

Firstly, samples of the base materials in question were created and textured using different strategies and varying laser parameters such as power, speed and number of passes. The bioactive materials were then deposited and incorporated on the surface of the samples using different techniques, such as CO2 laser sintering, conventional furnace method or deposition using a spatula. Finally, mechanical tests were performed in order to analyse and evaluate the properties of the produced samples. These include SEM-EDS, wettability, friction tests and cell viability tests.

Results show that the laser texturing was considered an effective and reliable method to produce different structures throughout the samples without compromising its mechanical properties. The employed functionalization techniques were successful, as mechanically interlocked and thick coatings were created. The incorporation of said coatings had a significant effect on the surface energy of the samples, since wettability tests showed that contact angle of the samples is reduced after the addition of the bioactive layer. Friction tests comproved the adherence of bone to the surface of functionalized samples, while biological tests revealed the bioactive potencial of the MTA coating.

In conclusion, textured samples were successfully produced and afterwards functionalized using different techniques. These surfaces showed promising results in both mechanical and biological tests, as this new approach for the development of functionalized knee prostheses is validated.

Keywords: Surface Functionalization; Hybrid Laser; Bioactivity; Knee Prostheses; Zirconia; Titanium

RESUMO

A artroplastia do joelho é um procedimento cirúrgico que consiste na remoção da totalidade ou de parte da articulação do joelho, retirando cartilagem danificada e substituindo a mesma por uma prótese ou implante. Assim, as próteses do joelho são dispositivos que substituem a função da articulação, possuindo diferentes componentes, cada um deles com uma função específica e compostos por materiais distintos. No entanto, a sua longevidade é ainda relativamente curta, de cerca de 15 anos, e a utilização de materiais com propriedades mecânicas desadequadas levam ao aparecimento de fenómenos indesejáveis que contribuem para a remoção da prótese de forma precoce.

É então importante encontrar soluções para melhorar não só a funcionalidade destes implantes, mas também a sua longevidade. Assim, este trabalho foca-se na modificação de materiais tipicamente usados nestes implantes (zircónia e titânio) através de uma técnica de processamento híbrida (subtrativa e aditiva), via laser. Foram assim criados padrões na superfície dos materiais, e incorporados neles compostos bioativos (hidroxiapatite e agregado de trióxido mineral), de modo a melhorar a bioatividade e consequente funcionalidade e longevidade das próteses do joelho.

Primeiramente, foram criadas e texturizadas as amostras dos materiais base em questão, utilizando diferentes estratégias e variando parâmetros do laser, como a potência, velocidade e número de passagens. Os materiais bioativos foram posteriormente incorporados na superfície das amostras através de diferentes técnicas, como sinterização a laser, forno ou deposição com recurso a uma espátula. Por último, foram efetuados testes mecânicos de modo a analisar e avaliar as propriedades das amostras produzidas, como o SEM-EDS, molhabilidade, testes de fricção e testes de viabilidade celular.

Resultados mostram que a texturização a laser foi considerada um método eficiente na produção de diferentes estruturas superficiais. As técnicas de funcionalização foram bem-sucedidas, já que camadas espessas de bioativos foram aprisionadas na superfície. A adição destes materiais afetou a energia da superfície, já que os testes de molhabilidade mostraram uma redução do ângulo de contacto após deposição. Testes de fricção comprovam a adesão de osso na superfície das amostras funcionalizadas, enquanto que os testes biológicos revelaram o potencial bioativo do revestimento de MTA.

Concluindo, amostras texturizadas foram produzidas e posteriormente funcionalizadas através de técnicas variadas. Estas superfícies demonstraram resultados promissores tanto em termos biológicos como mecânicos, sendo a abordagem de funcionalização proposta validada.

Palavras-Chave: Funcionalização Superficial; Laser Híbrido; Bioatividade; Prótese; Zircónia; Titânio

TABLE OF CONTENTS

LIST OF FIGURES

LIST OF TABLES

LIST OF ABREVIATIONS AND SYMBOLS

ECM – Extracellular Matrix

KA – Knee Arthroplasty

TKR – Total Knee Replacement

PKR – Partial Knee Replacement

ZrO_2 – Zirconia

Ti_6Al_4V – Titanium-Aluminum-Vanadium alloy

Cp Ti – Pure Titanium

CoCrMo – Cobalt-Chromium-Molybdenum alloys

UHMWPE – Ultra-high Molecular Weight Polyethylene

PR – Patellar Resurfacing

PE – Polyethylene

PCL – Posterior Cruciate Ligament

ACL – Anterior Cruciate Ligament

Ab – Albumin

RGD – Arginine-Glycine-Aspartic Acide Peptide

FA – Focal Adhesion Point

IgG – Immunoglobin G

OH – Hydroxyl

COOH – Carboxyl Groups

CHAP – Hydroxy Carbonate Apatite

HBDC – Human-Bone Derived Cells

SAMs – Self-Assembled Monolayers

WCA – Water Contact Angle

hFOB – Human Fetal Osteoblastic Cells

OTS – Octadecyltrichlorosilane

HOBs – Primary Human Osteoblasts

bAECs - Bovine Aortic Endothelial Cells

LST – Laser Surface Texturing

YAG – Yttrium-Aluminum-Garnet

Hap – Hydroxyapatite

TCP – Tricalcium Phosphate

CaO – Calcium Oxide

$Ca_4(PO_4)_2O$ – Tetracalcium Phosphate

MTA – Mineral Trioxide Agreggate

PC – Portland Cement

Y-PSZ – Yttria-stabilised Zirconia Powder

SLC – Sisma Laser Controller

OM – Optical Microscopy

SEM – Scanning Electron Microscopy

EDS – Energy Dispersive X-ray Spectroscopy

R_a – Mean Surface Roughness

R_z – Average Maximum Peak to Valley

ACA – Apparent Contact Angles

PBS – Phosphate Buffered Saline

COF – Coefficient of Friction

XRD – X-ray Diffraction

CHAPTER I

SCOPE AND AIM OF THE THESIS

This chapter presents the scope of this dissertation. It includes a short background and the motivation that led to the development of this work, as well as the goals/aims that are meant to be completed. Additionally, it is also presented a brief description of the structure of the present thesis.

1) Background and Motivations

The knee joint replacement procedure stands out as one of the safest and most effective treatments in the current biomedical panorama. However, there is still room for progression, since despite the tremendous evolution in terms of implant design, surgical technique and materials used, this process still shows clear problems and limitations.

One of the most worrying factors worldwide is the constant decrease in the age of patients submitted to this operation. In fact, the increase in the number of candidates to surgery under 55 years of age has clear implications on the durability of the implants used. Currently, knee prostheses still have a limited longevity: recent implants have an expected life span of 20 to 25 years, and the number of users presenting associated complications after 15 years is dramatically increasing [31,32,33]. Thus, the need for revision surgery is practically inevitable for young patients in the current context.

The causes of implant failure are many, but aseptic loosening stands out as one of the main causes of this insufficient longevity. Additionally, the phenomena of osteolysis, ineffective secondary fixation and stress shielding, caused by the inability of the implant to adequately fixate and respond to stresses established on it, are especially worrying among patients. Thus, and although this is a problem that is slowly being overcome, due to the development of materials with improved mechanical properties, it is still essential to develop alternatives that may overcome certain difficulties, especially in the biological parameter.

The introduction of advanced technologies capable of producing surfaces with well-defined patterns, in the order of micro and nanometres, opened new research opportunities, namely new strategies in the areas of tissue engineering and regenerative medicine. Among them, laser processing techniques stand out from the rest, due to their simplicity, precision, reproducibility and low cost.

From this point of view, the main challenge now lies in the development and design of new approaches that combine different methods and technologies in order to create functional and biocompatible surfaces capable of improving the osseointegration process and stimulate in a controlled way the response of the surrounding biological tissues. This will decrease the need for revision surgery, reducing the number of implant failures and providing patients with a safer and more functional implant.

2) Goals/Aims

Therefore, this work will be focused on the surface functionalization of different materials, such as Ti6Al4V and ZrO2, through a hybrid processing technique, additive and subtractive, and the creation of different patterns on their surface. Subsequently, bioactive compounds will be incorporated into the textured materials, in order to enhance the bioactivity of the implant. The main area of study will be knee prostheses, more specifically the functionalization of the tibial component, but the results obtained may be interesting for application in other types of implants (such as dental implants, for example). Thus, the main function of this modification will be to promote osteointegration of the prosthesis, preserving and increasing its overall stability in the short and long term during the bone regeneration process.

Based on the central objective of this dissertation, it was necessary to adopt a work strategy and establish a sequence of detailed objectives. Thus, the specific objectives of the present study are:

- To investigate the applicability of laser processing in the production of the different patterns;
- To optimise the laser texturing process in order to obtain feasible and defined patterns;
- To investigate the different techniques of incorporating different bioactive compounds in the textured materials;
- To characterise the surface morphology, topography and chemical composition of the patterns produced through SEM/EDS;
- To explore how surface functionalisation affects the wettability of the samples through contact angle measurements;
- Evaluate the tribological performance and structural integrity of the patterns produced through friction tests against bone, mimicking the insertion of an implant;
- To explore and quantify the osteogenic capacity of the samples after processing, through cell viability tests.

3) Organization of the Dissertation

This document is divided into five chapters that show all the research and practical work developed so far.

Chapter I presents the main motivations for the development of this work. The various objectives of this work are also listed, as well as a presentation of the overall structure of the dissertation.

Chapter II includes a study of the state of the art regarding the knee and knee prosthesis. In it, the anatomy of the knee is presented and described, the arthroplasty procedure and its different approaches are studied, and the different components that make up a knee prosthesis are analysed. Additionally, some of the limitations of current implants are identified and described, as well as the main causes for their failure, and the most popular surface modification techniques today are explored. The fundamental interactions between cells and biomaterials are addressed, as well as the impact of surface properties on their behaviour. Finally, the most popular surface modification techniques currently available are explored, as well as the different steps of the hybrid laser processing used in this work.

Chapter III explores the different steps of the experimental procedure of this work. The materials used are presented and their modification processes are described, by explaining the different strategies used and the varied parameters, using different schemes. Additionally, the morphological and mechanical tests are presented and elaborated in detail.

In chapter IV, the results of the procedures described in the previous chapter are exposed and discussed, in a sequential order. Positive and negative aspects are pointed out, reasons why some samples are disregarded are explained, and those that best fit the objectives of the work are chosen. The coating and sintering processes are analysed, as well as the results obtained in the sessile drop, friction, strength and cellular viability tests.

Finally, Chapter V presents the main conclusions drawn from this work, as well as some suggestions for future works.

CHAPTER II

STATE OF THE ART

This chapter includes a state-of-the-art study of the knee and knee prosthesis. The anatomy of the knee is presented and described, the arthroplasty procedure and its different approaches are studied, and the different components that make up a knee prosthesis are analysed. Some of the limitations of current implants are identified and described, as well as the main causes of implant failure. The fundamental interactions between cells and biomaterials are addressed, as well as the impact of surface properties on their behaviour. Finally, the most popular surface modification techniques currently available are explored, as well as the different steps of the hybrid laser processing used in this work.

1) Anatomy of the Knee

1.1) The Bone

The bone is a calcified, connective tissue, characterized by a combination of various types of tissues, such as cartilage, fibrous tissue, bone marrow and osseous tissue. Bones are vascular and heavily innervated, typically through adjacent arteries and veins that enter the internal cavity of the bone, supplying the marrow and spongy bone. The bone has a wide array of functions, as they act as reservoirs of calcium and phosphorus, protect vital organs, contain blood-producing cells, and support the loads applied during locomotion, as well as the mechanical action of soft tissues (contraction and distention of muscles) [1,2]. Figure 1 presents the various levels of organization of bone tissue, from macro to nanostructure.

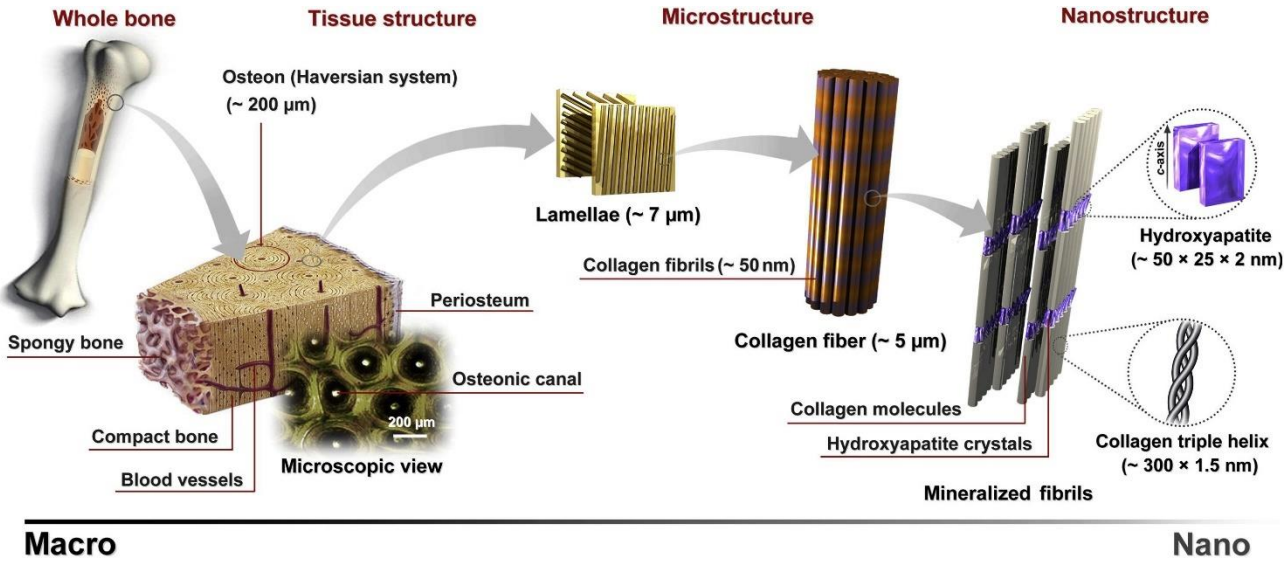

Figure 1 - Hierarchical structural organization of bone. Adapted from [3].

There are two types of bone, compact (or cortical) and spongy (or cancellous). Compact bone is denser and mechanically more resistant, forming the outer shell of all bones and surrounding spongy bone, that consists of spicules of bone enclosing cavities containing blood-forming cells (bone marrow). Compact bone is lamellar in structure, described as a well-organized network of collagen fibers and deposits of inorganic material, such as hydroxyapatite (Hap). On the other hand, cancellous bone comprises of bone-related cells and a mineralized extracellular matrix (ECM) [1,4]. In addition, all bones are covered externally (except in the area of a joint) by a fibrous connective tissue membrane called the periosteum. This membrane receives blood vessels that supply the outer layers of compact bone, regulated by the presence of vasomotor nerves [1,2].

When it comes to the bone microflora, there are four types of cells: osteogenic cells (bone stem cells), mesenchymal (bone-forming cells), osteocytes (osteoblasts preserved in the osseous matrix and responsible for normal bone metabolism) and osteoclasts (responsible for dissolution and resorption of old bone) [4]. Therefore, these cells are fundamental in the maintenance of the bone tissue.

The bone undergoes remodelling throughout life. This process can be the result of the action of osteoblasts and osteoclasts in defects such as microfractures, or the continuous old bone replacement by new tissue, so that it adapts to mechanical loads and strain [4]. This renewal can be divided into three consecutive phases: resorption phase, in which old bone is removed through the action of the osteoclasts; reversal phase, in which mononuclear cells prepare the surface and provide signals for bone differentiation and migration; and the formation phase, in which new bone is deposited by the action of osteoblasts [2,4].

1.1.1) Osseointegration Mechanisms

Osseointegration is defined as a structural and functional connection between living bone and the surface of a load bearing implant, without the formation of a biofilm or an interposing fibrous soft tissue. The process itself is quite complex and there are many factors that influence the formation and maintenance of bone at the implant surface [5] (figure 2).

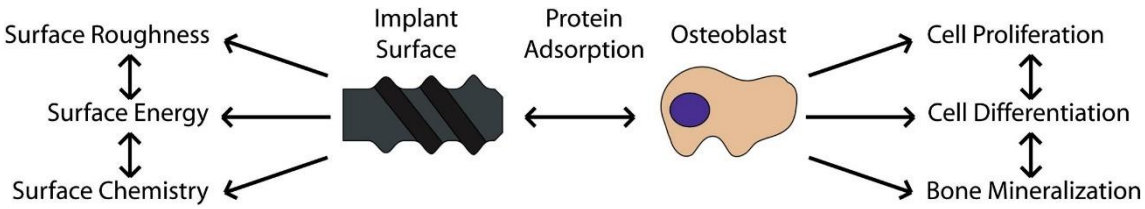

Figure 2 - Mechanical factors that tend to affect different cell functions, such as differentiation, proliferation and, in the case of osteoblasts, bone mineralization. Adapted from [6].

The insertion of an implant causes trauma to the bone tissue, activating the bone's natural wound healing mechanism [5,7]. Therefore, the primary healing process in the implant system is similar to primary bone healing. One of the first events to occur when an implant is inserted is the adsorption of proteins and plaquettes to the surface of the material, which promotes the formation of fibrin clots, facilitating cell migration towards the prosthesis [6]. It has been shown that enhancing the roughness of the surface enhances the strength of fibrin clot adherence, which in turn facilitates wound contraction and healing

response [7]. Blood is also present between the fixture and the bone, which leads to a mild inflammatory response and the formation of a blood clot. Through the activity of phagocytic cells, the later evolves into a premature ECM that surrounds the implant [7]. At this point, the implant is barely attached to the bone through mechanisms of friction (primary stability), as can be observed in figure 3. Until 2-4 weeks after insertion, the implant is at its lowest stability, in which clinical problems typically occur. This is due to the transition from primary to secondary stability (stability dip).

After the establishment of the fibrin network and the ECM around the implant, bone growth can be induced on two different fronts: on the surface of the bone near the implant (distance osteogenesis) or directly on the surface of the implant (contact osteogenesis). This leads to an increase in the secondary stability, also known as biomechanical stability, and the degree of osseointegration is dependent on the percentage of bone-to-implant contact [6,7]. Afterwards, the bone remodelling cycle is activated, resorbing newly formed bone to resolve microcracks and priming the surface for new bone formation (more organized, compact and stronger) [6]. In general, at the end of 3-6 weeks the prosthesis is biologically and mechanically integrated into the bone.

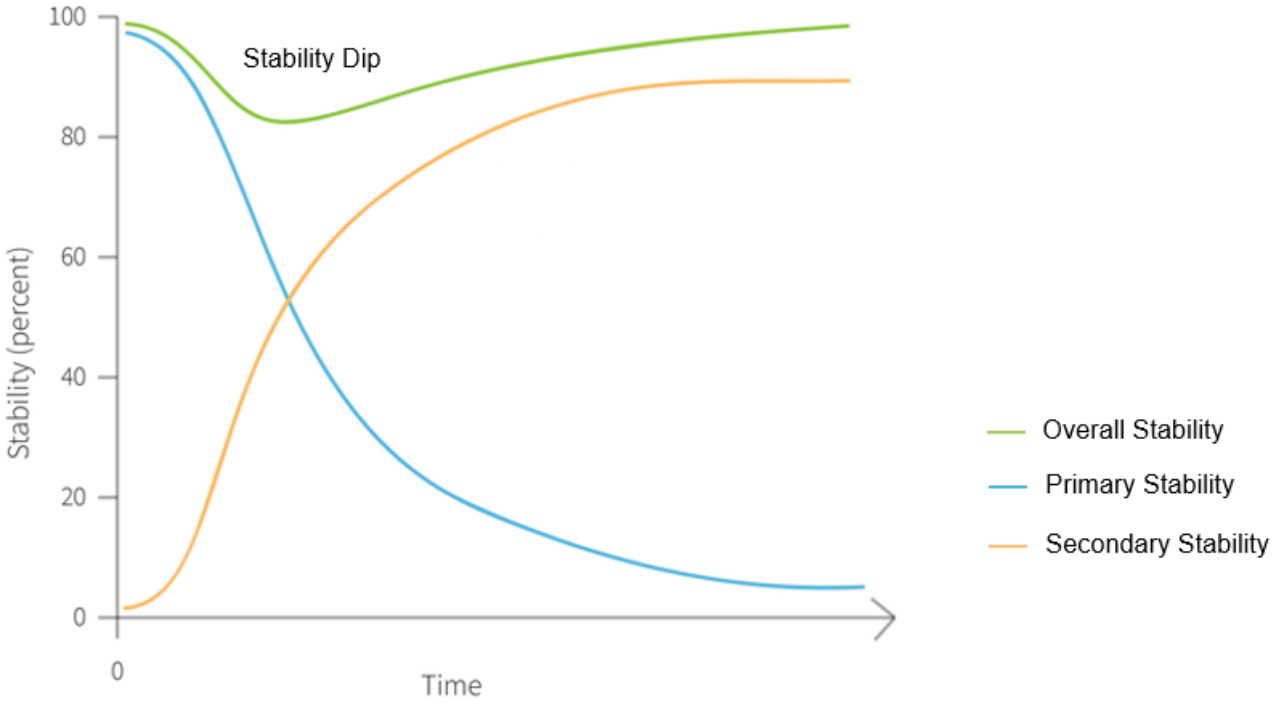

Figure 3 - Evolution of the primary (friction) and secondary (osseointegration) stability after prostheses insertion. Overall stability dips 2-4 weeks after surgery, and posteriorly recovers. Adapted from [9].

1.2) Knee Joint

The knee joint is the largest synovial joint in the human body (figure 4). Located between the femur and the tibia, it is responsible for the efficient performance of the flexion and extension motions of the leg, acting as a "hinge". The knee joint consists of two sub-articulations: the one between the femur and the tibia, whose function is weight bearing; and the one between the femur and the kneecap, which allows the anterior femoral muscle to be directed anteriorly to the tibia, avoiding tendon wear [1].

The extremities of the tibia and femur (femoral condyles) are covered with (hyaline) cartilage, which facilitates movement and reduces friction in the joint. In fact, during flexion and extension motion, the femoral condyles glide over the tibia, alternating between a flat (extension) and curved (flexion) surface, as depicted in figure 2 [1]. Two fibrocartilaginous menisci (medial and lateral meniscus), one on each side, located between the femoral condyles and the tibia, accommodate the shape changes during joint motion [1]. Like all joints, it is further reinforced by two collateral ligaments, one on each side: the fibular collateral ligament and tibial collateral ligament, which stabilize the knee during "hinge" movements [1]. Additionally, two firm and strong ligaments connect the ends of the femur and tibia, keeping them in opposite positions throughout the movement. They are called cruciate ligaments, since they intersect in the sagittal plane, one being the anterior cruciate ligament and the other the posterior. Finally, there is also the patellar ligament, which connects the tibia to the kneecap [1].

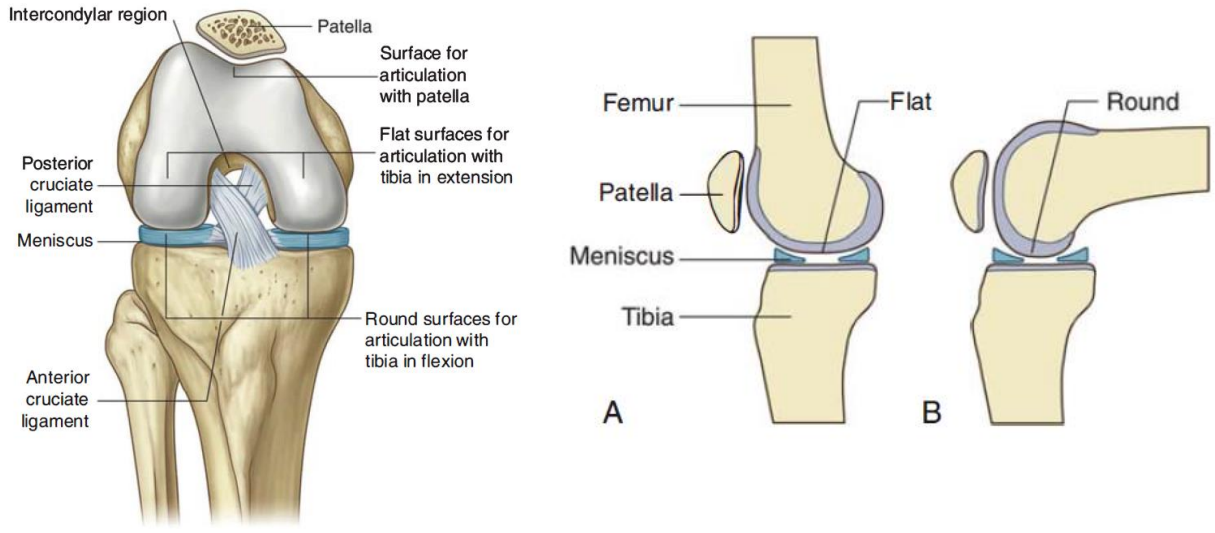

Figure 4 - Anatomical representation of the knee, as well as a schematic representation of the mechanisms of extension (A) and flexion (B) of the leg. Adapted from [1].

2) Knee Arthroplasty

Knee arthroplasty (KA) is one of the most successful surgical procedures for restoring knee functionality and provide pain-free mobility for patients with severe joint diseases such as osteoarthritis or inflammatory arthritis. With origins in the 1960s, KA is a procedure of increasing popularity in developed countries, and the average age of patients requiring this procedure has steadily decreased in recent decades, as it is increasingly indicated for patients below the age of 55 [10]. Some risk factors are, among others, bone density and morphology, gender, ethnicity, genetic factors, trauma, age, and obesity, with the last two being pointed out as the main cause of the recorded increase: the population in developed countries is getting older and older, and obesity rates have been rising for several years [11].

There are two types of KA, as shown in figure 5: total knee replacement (TKR), in which the entire joint is removed, and partial knee replacement (PKR), which seeks to replace only some affected parts of the joint [12].

2.1) Total Knee Replacement (TKR)

Considered the gold standard of KA, it is used in most patients, with rates reaching around 90% in several European countries [13]. This procedure consists of the removal of the damaged cartilage present in the femur and tibia, as well as some underlying bone, and replacing it with metal and plastic components that recreate the natural surface of the joint. The patella can also be removed and replaced with a button composed of a plastic material [14]. The approach typically used in surgery is the medial pararotular approach: the surgeon makes an incision in the centre of the knee (smaller in minimally invasive techniques), cutting deeper tissues, such as the quadriceps tendon, to reach the tibia and femur. The knee is bent 90 degrees to facilitate access to the joint, the affected areas are removed, and the bones are cut to fit the implant properly. Since this is a complex and detailed process, computerized auxiliary tools can be used to align the cuts made [14]. After implant insertion, the knee is extended and the incision closed.

The indications for this type of procedure are not governed by age or gender, but rather by the type of condition presented by the patient. Thus, it is typically reserved for patients with chronic and debilitating symptoms that continue to persist despite exhaustion of all conservative and non-operative treatment modalities [14].

2.2) Partial Knee Replacement (PKR)

PKR is a procedure that consists of the removal of only a small portion of the affected joint, rather than replacing all three joint components, as is the case with TKR. This method can thus be applied exclusively to one (unicompartmental) or two (bicompartmental) of the medial, lateral, or patellofemoral compartments of the knee, and the rest of the procedure is quite similar to that described for TKR: removal of the affected cartilage and underlying bone, replacing them with a metallic or plastic component that allows the natural anatomy of the joint to be recreated and its function to be restored [15].

However, the indications for this procedure are somewhat more limited than those for TKR: indicated only for patients who are not obese, over 60 years of age, relatively active, and who experience joint pain only when walking or weight bearing [16].

There has been growing interest in PKR in recent years, as some studies seem to indicate that this strategy leads to a more functional outcome for patients than TKR [17] [18]. In addition to preserving the remaining healthy compartments of the knee, this strategy is less invasive than TKR, which typically leads to less blood loss, lower risk of developing infections, faster patient recovery, and less pain experienced during the procedure [19]. However, it is also important to note the high revision rate present in this procedure, that is, there is a greater need for a second surgery to remove, add or exchange one or more components of the implemented prosthesis [10] [17].

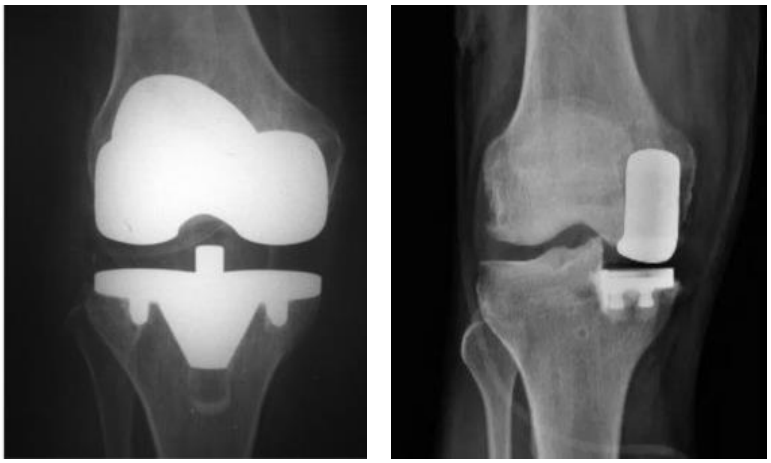

Figure 5 - Total and partial knee prosthesis, respectively. Adapted from [20].

3) Prostheses and Current Trends

3.1) Bulk Materials

The materials used in biomedical applications are called biomaterials. These can be defined as natural or synthetic materials integrated partially or totally into a living structure or biomedical device, whose purpose is to diagnose, treat, augment, replace or repair any tissue, organ or function of the body [21]. Depending on their function and the site where they are implemented, these materials need to exhibit different specific properties in order to ensure that they can perform their function properly and without causing adverse reactions in the surrounding tissues [21]. Thus, adequate mechanical and physical properties, high corrosion and wear resistance, biocompatibility and biofunctionality are some of the main concerns when selecting a biomaterial [21].

3.1.1) Zirconia (ZrO_2)

Zirconia (ZrO_2) is a ceramic material that has been the subject of study and interest as a possible substitute for metallic alloys for biomedical implants, such as knee, hip or tooth [22,23]. More particularly, the addition of 2 to 3 mol% yttria (Y2O3) to the chemical composition of zirconia seems to stabilize its tetragonal phase, giving rise to a biomaterial with optimized mechanical properties [24]: high bending strength (900 to 1200 MPa), toughness (7 to 10 MPa/m2), wear resistance and biocompatibility [25]. Furthermore, zirconia is considered an inert material, which means that it does not develop adverse reactions when implemented in the patient's body. However, this property may prove unfavourable for its use as a biomaterial: several studies point to a lower osseointegration capacity, since bone has difficulties to grow on the zirconia surface and fix the implant [26].

3.1.2) Titanium (Ti_6Al_4V)

Among all metallic materials, titanium is considered the most suitable for use in prosthetics and implants. The two most popular forms are pure titanium (Cp Ti) and titanium-aluminum-vanadium alloy (Ti_6Al_4V), the latter being the most used in knee prostheses. These materials have a lower density (4.5 g/cm3) and Young's modulus (110 GPa) than other metals, such as steel or aluminium, so they have a more elastic behaviour and can mimic the natural joint more easily, decreasing the probability of stress shielding and bone resorption [27]. Additionally, they have a higher corrosion resistance, since they spontaneously form a stable oxide layer on their surface, which also contributes to their high biocompatibility [28]. However, the fact that they are bioinert considerably decreases their osseointegration capacity, and despite having lower modulus of elasticity values than many other

materials, the difference between titanium and bone is still very high, with a ratio of approximately 5.5-1 [29].

3.2) Design and Components of Current Implants

The concept of a knee implant has undergone several changes over the years, from its conception in the 1950s to the present day. In fact, the first implants to ever be developed were made of only one metallic component [30] and were not very realistic. Thus, the evolution of the implant design, resembling as much as possible the natural geometry of the joint, and the adaptation of different materials with specific functions allowed the reduction of wear and tear of the prosthesis, as well as a considerable improvement of the user's mobility [31]. Figure 6 shows a typical knee prosthesis and its components.

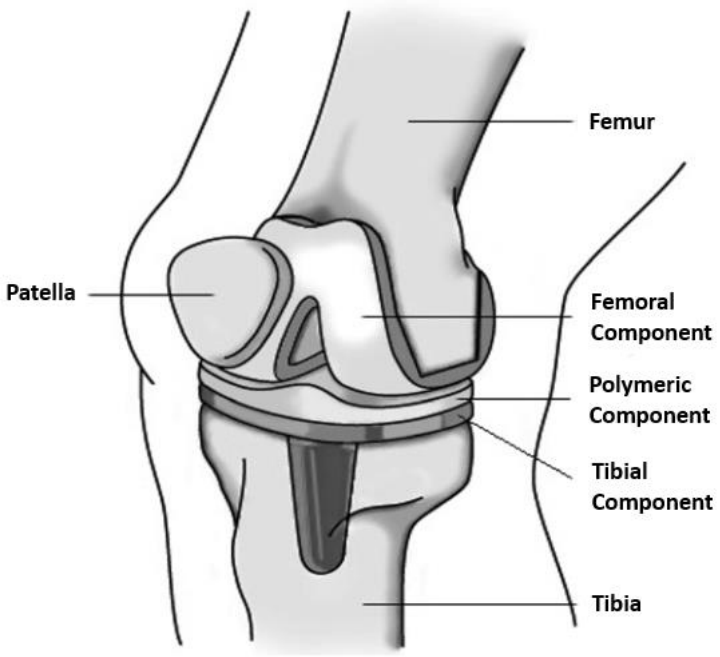

Figure 6 - Schematic representation of a knee prostheses and its respective components. Adapted from [32].

Thus, knee implants can be divided into:

3.2.1) Femoral Component

The femoral component of the implant replicates the anatomy of the distal femur, thereby replacing the lower end of the femur (femoral condyle). The prosthesis curves around the end of the femur and has an inner groove so that the patella can move smoothly against the bone as the knee bends and aligns, which prevents its lateral displacement [33].

The most common knee implants feature a metallic femoral component, typically cobalt-chromium or titanium alloys [31]. However, different ceramic materials have been studied and developed as an alternative to metal alloys for various implants, due to their high biocompatibility, excellent mechanical properties and inertness, such as zirconia [34,35].

3.2.2) Tibial Component

The tibial component resembles a small flat platform, placed on top of the bone and stabilized by a short stem inserted into the tibial medullary canal. Additionally, a polymeric separator is placed between the femur and tibia and attached to the tibial platform so that its upper surface is congruent with the face of the femoral component [33]. This flexible separator replaces the function of cartilage, since it has a smooth, sliding surface that allows the displacement of the femoral and tibial elements and the consequent acts of knee flexion and extension [31,33].

In the tibial component, the choice of metal is a little less rigorous, since there is reduced traction or friction during movement, due to the action of the polymeric component. Still, and similarly to the femoral component, it is typically composed of titanium or cobalt-chromium-molybdenum (CoCrMo) alloys [31]. On the other hand, the polymeric separator typically contains ultra-high molecular weight polyethylene (UHMWPE), a thermoplastic polymer widely used in implants and several medical devices, since it has high tenacity and low friction coefficient [36].

3.2.3) Patellar Component

The patellar component resembles the natural knee cap. Cupped in shape, it is fitted underneath the patient's natural patella and inserted into the groove in the femoral element [37,38]. Thus, it is crucial that these two components are properly aligned for proper functioning [33]. Like the plastic separator, this component is typically made of ultra-high molecular weight polyethylene (UHMWPE) [31,33]. The replacement technique is called patellar resurfacing (PR), and also involves removal of the femoral trochlea and damaged cartilage [38].

This element is not present in all knee prostheses. In fact, the frequency of its use tends to vary considerably: while most European countries, such as Sweden or Norway, report very low rates of RP (4 to 15%), this type of procedure is standard practice in the United States, with rates around 80% [39]. Thus, there is no consensus on the usefulness of this resurfacing procedure, and its use is quite controversial. Some studies point to its effectiveness in reducing the incidence of anterior knee pain, while others highlight a higher prevalence of fractures, joint damage, and secondary instability [40]. Thus, PR

is not a simple surgical option; it relies on the properties of the patella in question (height, thickness, size, and alignment), the surgical technique, the predictable outcome, and the experience of the surgeon [41].

The creation of functional models whose geometries maximized the surface area of the metallic components of these prostheses made it possible to reduce the stress on the most sensitive parts, as is the case of polyethylene (PE) [42], and different anatomical models made it possible to retain and consequently preserve the posterior cruciate ligament (PCL) and anterior cruciate ligament (ACL) if they are healthy (cruciate retaining) [31]. In the 1970s, the mobile-bearing model also appeared, designed to reduce wear between the tibial and polyethylene components and to provide a greater range of motion, especially for younger and more active patients. In this model, the PE component can rotate slightly inside the tibial plate, which allows for increased contact area, reduced contact stresses, and increased medial and lateral displacement angle [43]. However, these advantages are still debatable [44-46]. Regarding their fixation, implants can still be cemented, if they are fixed in the joint using polymethylmethacrylate, a synthetic adhesive; or uncemented, if they are simply pressed onto the bone [47]. Cemented implants are considered the gold standard, typically achieving better results [48].

3.3) Current implant limitations

Despite the remarkable evolution of knee prostheses reported above, namely in terms of design, materials used and consequent functioning, it is important to note that these devices still present some limitations after implementation in the user. In fact, 15-20% of patients who have undergone total knee replacement consider themselves dissatisfied, obtaining little benefit or describing a poor outcome after the intervention [49]. Additionally, annual registries from several countries report a revision rate of 3-5% in the first 10 years of use, with this percentage nearly doubling after 15 years [50,51,52]. Although still more common among older patients (older than 65 years), the need for revision surgery in young patients has gradually increased in recent years, with no apparent explanation: some theories point to an increased reliance on the procedure or an increased prevalence of osteoarthritis in this age group [10].

The prevalence of the causes of this revision surgery varies widely depending on the country analysed [49-51]. They can be biological/pathological (such as infections, arthrofibrosis or progressive arthritis) or technical/mechanical complications (such as aseptic loosening, periprosthetic fracture or implant instability). Thus, table 1 presents some of the reasons that motivate the need for further surgery, as well as their consequences and prevalence, obtained from the registries of some developed countries [49-51].

Table 1 - Main causes of revision surgery and respective prevalence (%).

Factor	Causes	Prevalence (%)
Infection	Biofilm formation on the implant surface [55]	30 to 35
Aseptic Loosening	Ineffective fixation, stresses on the implant [55]	20 to 25
Anterior Knee Pain	Muscle imbalances, incorrect positioning/design [55]	10 to 15
Instability	Soft tissue failures, incorrect positioning [53].	5 to 10
Periprosthetic Fracture	Old age, osteoporosis [54]	5 to 10
Arthrofibrosis	Excessive inflammatory response [55]	2 to 5
Progressive Arthritis	Evolution and spread of arthritis in the patient [55]	2 to 5

Thus, among the causes presented it is important to highlight:

3.3.1) Infection

One of the factors with the greatest growth in recent years, the development of infections is a result of the extremely hostile environment present in hospitals. Coming from other patients, healthcare professionals, contaminated equipment or airborne droplets, bacteria adhere to the implant surface and form biofilms, developing defense mechanisms against host responses [56]. This factor is estimated to account for about 30-35% of current TKA revisions, as it is one of the most prevalent complications in the current landscape [57]. The main symptoms include persistent pain, erythema, swelling and localized heat [56].

Most infections are reported in a fairly short postoperative period, typically in the first 5 years (figure 4) [57]. This statistic is alarming, considering that an implant failure in this time window can be regarded as a considerable failure. Diagnostic methods for this type of complication are varied, and include radiographs, bone scans, serological tests, and synovial fluid examinations [56]. Early diagnosis is crucial,

since a delay in detecting the infection may allow it to become established at the bone-implant interface, thus eliminating the possibility of using antimicrobial treatment and consequent prosthesis retention [58].

The eradication of this type of problem seems unlikely, so prevention and consequent attention to preoperative details is fundamental to avoid the development of infections: minimization of traffic in the operating room, appropriate use of masks and gloves, air ventilation and regulated use of antibiotics are among the most important factors [59].

3.3.2) Aseptic Loosening

Aseptic loosening is usually caused by wear of the prosthesis, as a result of the stresses imposed on the knee that slowly wear away the material. This wear leads to the slow release of small toxic particles, which eventually triggers an anti-inflammatory reaction on the part of the wearer. This autoimmune reaction leads to the resorption of bone tissue near the joint (osteolysis) and a consequent displacement of the implant [60]. This wear rate is thus influenced by the duration of implant use and the type of daily activity of the patient, so this factor is mainly of concern in young and active patients [10].

Due to increasing research and constant development of implant materials, particularly UHMWPE, this type of complication has been decreasing over the last decades. Still, it is estimated that aseptic enlargement accounts for about 20-25% of TKA revisions today [50-52].

In addition to osteolysis, this enlargement may also have other associated causes. Indeed, the appearance of this phenomenon at an early postoperative stage probably reflects the initial inability of the implant to fixate, while the displacement reported at a later stage may be related to insufficient secondary bone resorption or, as already mentioned, osteolysis [57,60]. However, this phenomenon tends to be more prevalent at a later postoperative stage, contrary to what happens in the case of infections (figure 7).

Additionally, the stress shielding phenomenon is also a relevant factor in this type of complication. Since the metallic materials present in the implemented prostheses have a Young's modulus much higher than that of bone, these components are much stiffer than natural bone, so they tend to absorb stresses that would typically be applied to it. Thus, and since bone tissue is shaped by the stresses under which it is placed (Wolff's Law), it becomes less dense and consequently more fragile, which can lead to bone resorption and consequent implant enlargement [61].

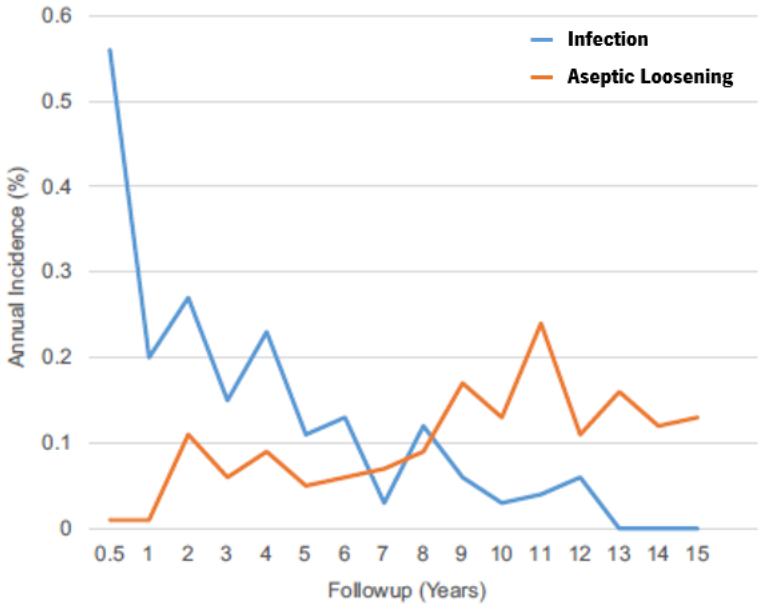

Figure 7 - Variation of the annual incidence of periprosthetic infection versus aseptic loosening. Adapted from [8].

3.3.3) Anterior Knee Pain

Anterior knee pain is one of the most common and persistent problems following the implantation of a total knee prosthesis, and can occur in patients with or without patella replacement [62]. The causes are diverse and even divided into two categories: functional problems inherent to the user, such as muscle imbalances, preoperative osteoarthritis, or dynamic knee valgus; or mechanical problems related to the implant, such as incorrect positioning of prosthetic components, fractures of the patellar component, or ineffective design [62]. Functional problems are the most common. Within this category it is important to highlight osteoarthritis, which, in more advanced stages, can weaken the muscles of the quadriceps femoris. This deterioration is often catalysed by implant implementation, which leads to maltracking of the patella, disturbing the dynamics between it and the trochlea [63], and a consequent alteration of the natural movement pattern of the knee and associated pain [64].

Regarding the mechanical factors, it is important to emphasize the importance of appropriate patellar implant selection: the prosthetic trochlea implemented should ensure adequate and effective patella tracking [64].

Despite the steady decrease in the frequency of these types of problems after TKA, due to constant improvements in implant design and surgical technique, it is estimated that rotator cuff complications still account for about 10-15% of all knee revision surgeries [65].

3.4) Cell-Biomaterial Interactions

A deep understanding of the interaction between biomaterials and cells is fundamental for the creation of effective biomaterial surfaces since the implants are intended to contact directly with living tissues and body fluids. Even though the desired bulk properties in terms of strength or elasticity can often be achieved, most of them do not meet the requirements for a specific clinical application. For instance, cp-Ti or its alloys do not possess adequate osteoinductive and osteoconductive properties, despite being biocompatible materials [66]. Therefore, tailoring the biomaterials surfaces for a solid interaction with the human body is a difficult and complex task.

Cell adhesion to a biomaterial surface is a critical step for the integration of implants since it precedes other events, such as cell spreading, cell migration, and often cell differentiation [67]. Most mammalian cells are anchorage-dependent, meaning that they must adhere to a surface in order to survive [68]. Therefore, improvements on these processes through the surface modification of the biomaterials will allow earlier functional solicitation and long-term stability of the prostheses.

3.4.1) Fundamental Interactions

The integration of a biomedical implant is characterized by different cellular events and mediators, as well as different processes that allow for cell-to-cell communication. The entire biological integration process can be summarized in figure 8.

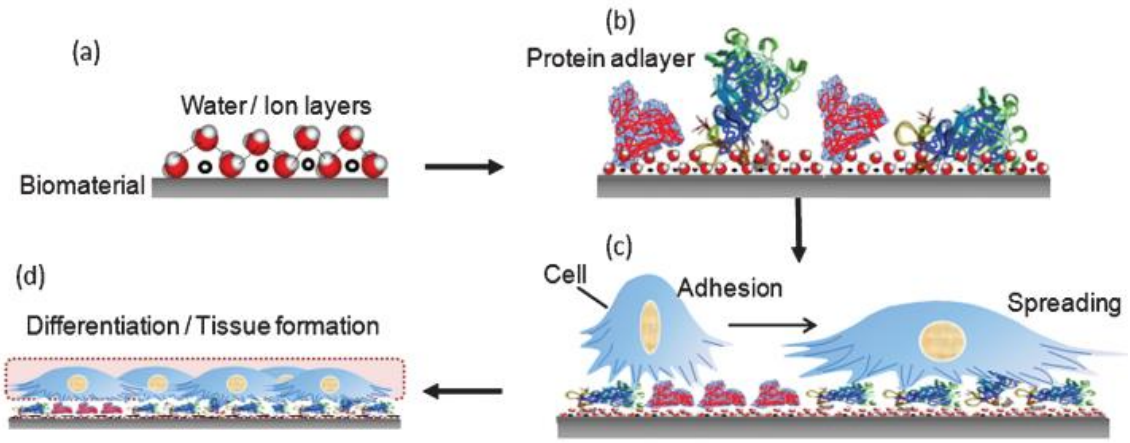

Figure 8 - Phases of the osseointegration process. Water molecules present in the surface of the biomaterial (a) lead to the adhesion of a protein adlayer to the interface (b). This protein layer serves as an anchor point for the deposition (c) and differentiation/proliferation of cells. Adapted from [70].

Proteins are the main meditators that define the entire mechanism of cell adhesion, growth and differentiation. In fact, after implantation in the body, it takes only a few minutes for proteins in the body

fluid to adsorb and cover the surface of the implant, forming the conditioning film [70]. This film is mainly composed of albumin (Ab), fibronectin, laminin and other extracellular matrix proteins, from which cells can recognize and establish contact with the biomaterial surface through specific receptors, called integrins. These transmembranar proteins act as a bridge between the adsorbed protein and the interacting cells, binding specifically to RGD (arginine–glycine–aspartic acid peptide) sequences, present in most ECM proteins (especially in fibronectins), and forming focal adhesion points (FA) [69,71,72]. Therefore, these adhesive structures establish a bridge between the cellular cytoskeleton and the ECM proteins (figure 9), inducing adhesion, spreading and mitigation.

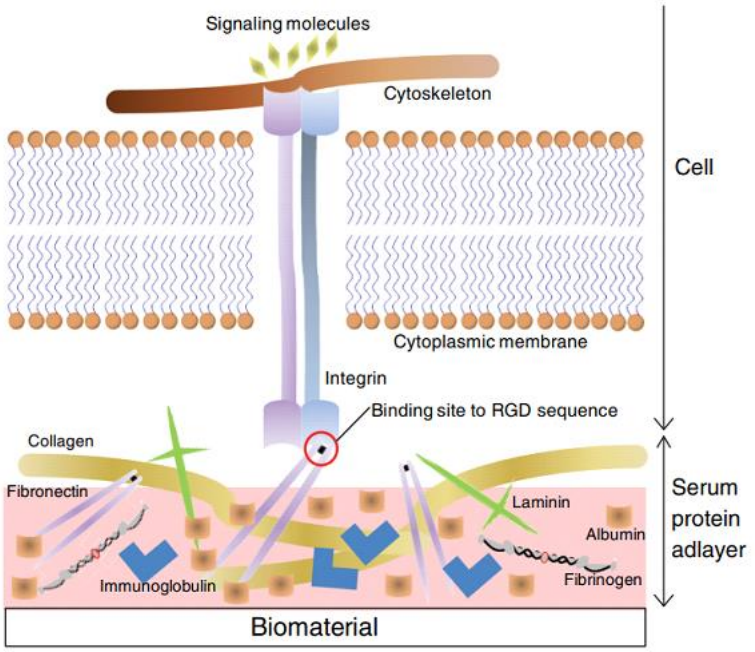

Figure 9 - Formation of the focal adhesion points in the surface of the biomaterial. Adapted from [69].

Many integrins are capable of binding to more than one protein, whereas many proteins can act as ligands for more than on integrin. Some of these connections are highly specific, controlling the cells functions and fate, while others do not necessarily affect cellular activity [73]. This variety of interactions is due to the presence of two non-covalently associated glycoprotein subunits in the integrin protein, namely α- and β- subunits. Different types of α- and β- subunits and different combinations between them exist, thus a huge variety of integrins with the ability to bind to different types of ligands are available [74].

The substratum surface properties play a big part in the adhesion of the initial protein adlayer. In fact, the formation of the conditioning film depends on the number of proteins present in the human body, on the physico-chemical properties of the biomaterial (such as roughness and surface energy) and on the

biological environment (temperature, pH, etc). The combination of these parameters regulates the properties of the protein adlayers, such as their conformation, orientation, distribution and elongation [69,71,72]. Consequently, and since cell functionality is determined by the characteristics of the protein adlayer, the substratum surface properties are also intimately related to cell fate. In fact, research has shown that, along with topography, the surface chemistry, porosity, microstructure, surface area, thermal, mechanical and electrical properties of the biomaterial play a significant role on cell behaviour [75-78]. For example, cells grown on micro-rough surfaces orientate, spread and differentiate themselves better than on smooth surfaces [79]; the tailoring of the pore size can be used to meet specific applications, optimizing the ingrowth of different cell/tissue types [80]; surface chemistry affects surface energy, which in turn mediates cell response through protein adsorption and interaction [81], etc.

3.4.2) Impact of Biomaterial Surface Properties on Cellular Behaviour

As already mentioned, it has been established that surface properties have a major influence on the process of tissue integration. Some of the most relevant indicators are chemical composition, surface energy, wettability, roughness, topography and surface morphology. Therefore, they will be explored in detail in the next sub-topics.

3.4.2.1) Surface Chemical Composition

Surface chemistry plays a fundamental part in the physiological interactions with biomaterials, as it is closely related to surface energy due to the functional groups and electrical charges. Therefore, surface chemistry has direct impact on protein adsorption, affecting factors such as the amount and conformation of the protein adlayer. Different functional groups interact with cells, proteins and tissues in different ways, as shown in research. In fact, nonpolar, hydrophobic groups such as methyl (CH3) typically create non-specific short-range interactions such as van der Waals interactions, which allow strong binding of fibrinogen and immunoglobin G (IgG) [82]. In contrast, polar and hydrophilic groups, such as hydroxyl (OH), induce conformational changes in fibronectins, which leads to the exposure of more adhesive points for cell adhesion. Carboxyl groups (COOH) (negatively charged in blood serum) typically interact with fibronectin and albumin [83].

Research shows that chemical surface modifications can alter cell activity and function. Indeed, Zreiqat et al [84] investigated the effect of surface chemistry modification of titanium alloy (Ti6Al4V) with magnesium, zinc and alkolide-derived hydroxy carbonate apatite (CHAP) on the function of human-bone derived cells (HBDC). Results showed that this surface modification resulted in modulation of key intracellular signalling proteins, which contribute to a better integration between integrins and the

mapkinase pathway, and consequently enhanced osteoblast differentiation. Additionally, a study developed by Keselowsky et al [85] reported that surfaces coated with self-assembled monolayers (SAMs) with different terminal functional groups (CH3, OH, COOH and NH2) altered the functional presentation of the integrin-binding domain of fibronectin, therefore modulating integrin binding, localization and specifity. This control of adsorbed protein activity represents a versatile approach to obtain specific cellular responses in biomaterial applications.

3.4.2.2) Surface Energy and Wettability

Surface energy is dictated by the quantity and type (physical or chemical) of unsatisfied bonds present at the surface of a given material, as it is directly dependent on the surface chemistry [86]. Research has shown that a higher surface energy is associated with a higher adsorption of proteins, such as fibronectin and albumin [87], and higher bone cell response. In another study, conducted by Hallab et all [88], surface energy was considered the most influential surface characteristic on cellular adhesion strength and proliferation.

Surface wettability is characterized by the water contact angle (WCA), which refers to the surface ability to be wetted by a drop of liquid water. The size and shape of the drop, as well as the contact angle, can be determined by the balance between the cohesive force, that attracts the molecules of the liquid to each other, and the adhesive force, that attracts the liquid molecules to the surface. Surfaces with high WCA exhibit a water-repellent behaviour, while surfaces with low WCA have high affinity with water. Therefore, materials that exhibit a WCA > 90° are considered hydrophobic, while materials that exhibit a WCA < 90° are considered hydrophilic [89].

High surface energies are typically related to high surface wettability. However, since wettability is also dependent on the surface topography, the roughness of the material can also influence this parameter, as shown by Hallab et all [88]. In their study, and after the introduction (increase) of surface roughness, materials with lower surface energy, such as polymers, showed an improvement in cellular adhesion strength, while materials with higher surface energy, such as metals, showed little change in this parameter. In fact, when roughness is introduced in a high energy surface, the resulting wettability might even be reduced, behaving as a hydrophobic surface. This happens since air bubbles are trapped on the asperities of hydrophobic surfaces, preventing protein adsorption and subsequent interaction with cell receptors in certain areas, as shown in figure 10 [90]. Therefore, and as discussed by Majhy and all [90], moderate surface energy ($E \approx 70mJ\ m^{-2}$) leads to the formation of the strongest cell-ligand

bonds, while an intermediate roughness ratio ($r \approx 2$) stimulates the optimal formation of focal adhesion points.

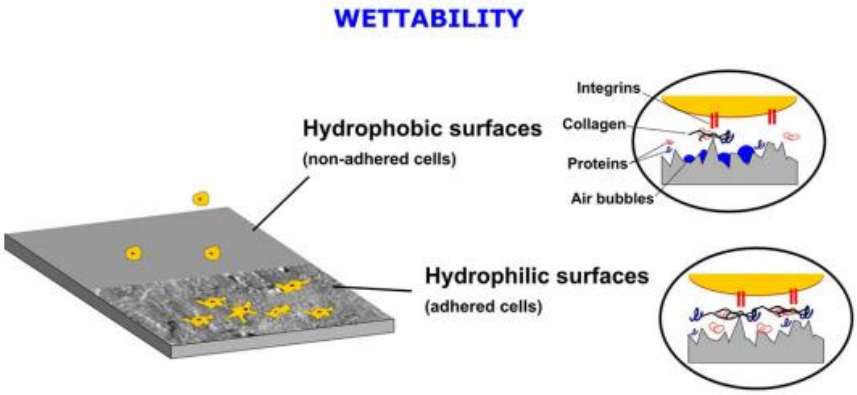

Figure 10 - The increase in roughness produces two types of models: hydrophobic, if the air bubbles accumulate in the grooves of the sample; hydrophilic, if proteins can achieve full deposition on the substrate surface and interact with cell receptors. Adapted from [90].

The degree of the contact angle affects protein adsorption, blood coagulation [91], platelet adhesion/activation [92] and cell and bacterial adhesion. As expected, research shows that surfaces with hydrophilic characteristics tend to promote higher protein adsorption and cell adhesion than hydrophobic surfaces. In fact, several studies have concluded that moderate hydrophilicity ($\sim 40° < \theta < \sim 70°$) promote a much more balanced protein adsorption, as well as better cell proliferation and differentiation [93-96]. Furthermore, a study conducted by Lim et all [95] proved that surface energy impacts not only short-term cell behaviour, but also has later stage effects on the osteoblastic cell growth and mineralization. In their work, human fetal osteoblastic (hFOB) cells were cultured on plasma-treated quartz ($\theta = 0°$, hydrophilic) and octadecyltrichlorosilane (OTS)-treated quartz ($\theta = 113°$, hydrophilic). It was concluded that hydrophilic surfaces produce homogeneous osteoblastic cell growth and mineral deposition, all while enhancing the quality (mineral-to-matrix ratio) and quantity of mineralization, when compared to hydrophobic surfaces, that tend to form randomly distributed structures filled with cells and decreased mineralized area.

Even though, as discussed, moderate hydrophilicity is the ideal surface wettability for biomaterials, the majority of the current implant surfaces exhibit hydrophobic behaviour [97]. Therefore, different strategies and procedures have been developed to modify the implant surface energy and other related properties, usually by modifying the surface composition or nature (oxygen content increase, radical formation, bioactive material incorporation) [97]. Some of these treatments include the use of SAMs [98,99], polymer brushes [100] or photolithography [101].

3.4.2.3) Surface Topography

3.4.2.3.1) Roughness

Several studies have shown that cell adhesion and proliferation occur more rapidly in surfaces with relatively higher roughness, in comparison to smoother surfaces [90,102,103]. This behaviour is related to protein adsorption, more specifically fibrin, which in turn dictate the preferential sites for the attachment of cells [101]. Additionally, higher roughness is indicative of an additional contact surface area, contributing to a higher mechanical interlocking in the interface, and a higher degree of pits and craters to act as the anchoring points [104]. Different cell behaviour can be observed, depending on the type of cells and the roughness of the material. In the case of osteoblastic cells, surfaces with moderate roughness ($Sa \sim 1 - 2\ \mu m$) are considered ideal [102-105].

3.4.2.3.2) Morphology and the Scale Effect

Surface structures can be defined as macrostructures (100 μm – millimetres), microstructures (100 nm – 100 μm) or nanostructures (1 – 100 nm) according to their size. Research shows that each length scale has a specific influence in tissue integration, therefore being of high importance in the cell-biomaterial interaction [106]. Figure 11 illustrates the different interactions between cells and biomaterials, according to the scale length.

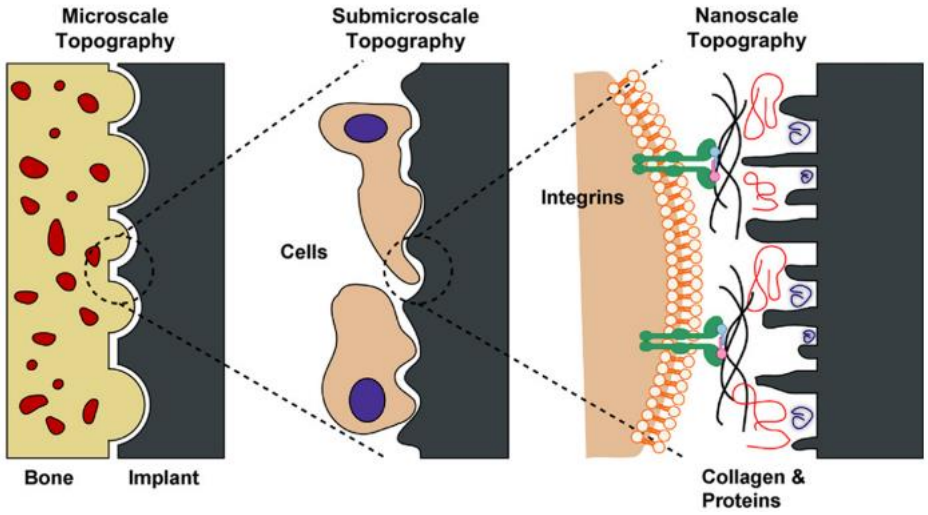

Figure 11 - Interactions between cells and biomaterials according to scale. Adapted from [6].

Surface topography at micro/nanoscale is well-documented to have a direct impact on the morphology, activity, orientation and phenotypic expression of cells. At the nanoscale, cells have potential interaction with ECM proteins, modulating various cellular activities. At the microscale, topography

governs the mimicking of the tissue structure, modulating the spatial organisation within ECM proteins. Macroscale affects the 3D structure, determining size and shape [106].

Surface morphology is described as the study of form involving shape, size and structure. It is especially important for nanomaterials since form tends to dictate their physical and chemical properties [108]. The rapid evolution of nanotechnology has facilitated the development of nanoscale surface modification. In fact, structures like nanogrooves [109], nanopits [110], nanoneedles, nanoleaves and nanotubes [111] have all been successfully imposed in the surface of different biomaterials and shown to directly influence cellular behaviour. Nanoscale structures tend to disrupt the formation of adhesion sites, acting as initial promoters of cellular adhesion, also having impact in cell differentiation and function [112]. Lin et al [112] investigated the effect of different TiO_2 nano/microstructures in osteoblast adhesion and proliferation, such as nanotubes, sponge-like structures and nest-like structures, as represented in figure 12. It was concluded that the nest-like structures displayed higher roughness and larger specific surface area, therefore proving to be the best approach for applications regarding bone-implant integration.

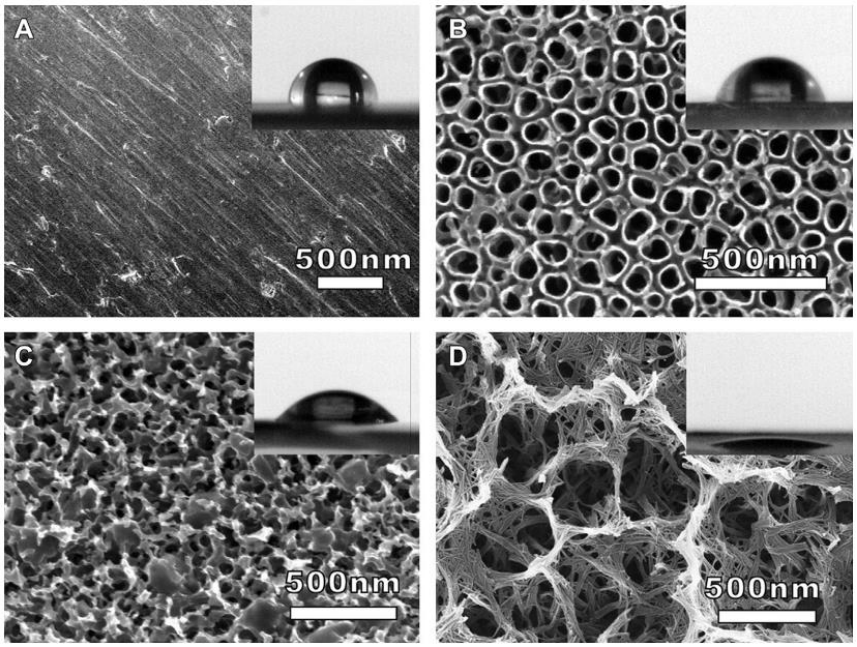

Figure 12 - Surface wettability of different nano/microstructures: nanotubes (a); sponge-like structures (b) and nest-like structures (c;d). Adapted from [112].

However, these structures can also be used to inhibit bone resorption and prevent cell adhesion, as showed by Biggs et al [111]. In their study, the authors claim that osteoblast adhesion and tissue mineralization can complicate the removal process of some plating systems, increasing torque, inducing latent pain and predisposing screw and bone damage. Therefore, nonadhesive surface modification could greatly benefit the design of some orthopaedic implants. The introduction of nanopits disrupted the

adhesion of primary human osteoblasts (HOBs), preventing sufficient contact formation at the cell-substrate interface and disrupting early focal contact formation, therefore denying cell adhesion in these structures.

3.4.2.3.3) Topographical Organization

In the last few years, the influence of surface topography on the response and behaviour of cells has been heavily researched. In fact, different structures with different shapes and dimensions have been developed and studied, such as grooves, pits, tubes, needles, pores, and many others. Each of these topographies has a distinct effect on cell fate and have been used to modulate their function and response to different biomaterial surfaces [110-113,114]. The most widely studied structures, however, are pits and grooves, due to their simplicity and effectiveness.

In the presence of topographical patterns, cells tend to orient and migrate bidirectionally in response to these specific cues, a phenomenon known as contact guidance, since filopodia and lamellipodia sense topographical signals. Bettinger et al [114] explored this fact and developed a method for fabricating biodegradable substrates with micron-scale features for cell-guidance applications, having studied the morphology of bovine aortic endothelial cells (bAECs) grown in these surfaces. The researchers varied the period and curvature of the rounded features, keeping the height constant. It was concluded that cells cultured on the substrate with smaller periods exhibited stronger alignment and reduced circularity relative to substrates with larger features. These results support the theory that filopodia play an important role in the detection of rounded microstructures, since cells showed preferential attachment to the apex of the microstructures, most likely due to the filopodia inherent ability to detect local gradients. In fact, substrates with smaller periodicity have a higher mean curvature, which presents a stronger topographic cue leading to an increase in cell alignment. In another study, Ramirez et al [115] studied the influence of inter-line spacing in cell bridging and alignment. In this study, parallel lines of fibronectin with constant width (2 μm) where micropatterned onto polyacrylamide gels, with inter-line spacing ranging from 0 (uniform) to 10 μm, and with line width large enough for typical focal adhesion formation. It was observed that cell elongation increased linearly with line spacing, while cell spread area decreased rapidly. Additionally, orientation increased sharply from 0 to 2 μm spacing, increasing smoothly afterwards until it reached almost complete alignment with the ECM in 10 μm spacing. Instantaneous migration speed was unaffected over the range of line spacing, but cell trajectories also became increasingly more parallel to the ECM. Furthermore, migration direction became increasingly parallel to the ECM as a function of line spacing, which is consistent with the changes observed in cell migration and shape. It was therefore

concluded that micrometer-scale variations in fibril-like spacing (2-3 μm) can tune cell shape and guide the direction of cell migration parallel to the ECM.

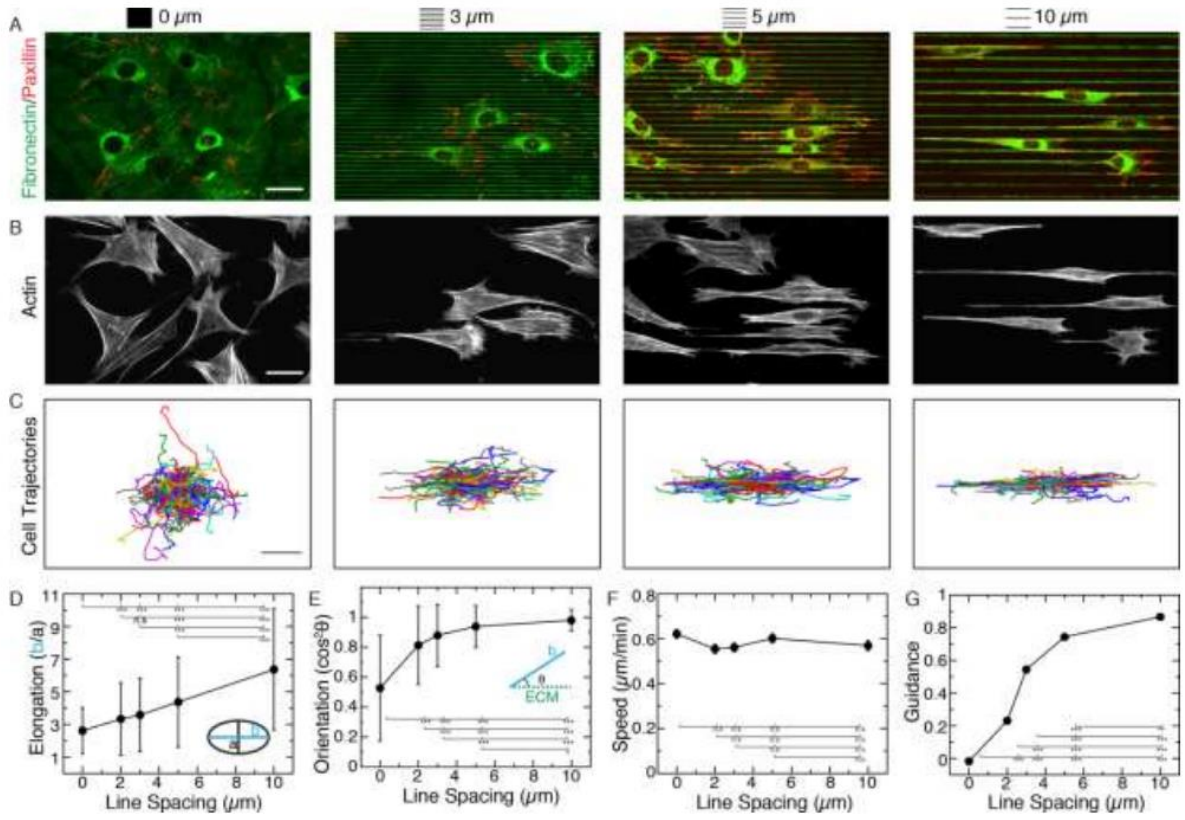

Figure 13 - Results obtained by Ramirez et al. An increase in inter-line spacing led to an increase in cell elongation and a decrease in cell spread area. Adapted from [115].

In fact, research shows that surface topography can even induce cell differentiation. For example, Giulio Abagnale et al [116] analysed the in vitro differentiation of MSC cells on micro-grooved surfaces, comparing cell activity in 25 different structures and varying the width of ridges and grooves from 2-15 μm. Contact guidance was observed, has cell spread and alignment was dictated by the structures present in the surface of the biomaterial. Additionally, it was observed that MSC cells differentiated into specific lineages according to the pattern of said structures: patterns with 2 μm induced osteogenic differentiation, while 15 μm patterns enhanced adipogenic differentiation. The authors concluded that the physical size of the ridges had a direct impact on cellular morphology: round morphology might drive the cells towards adipogenic lineage, whereas elongated morphology enhances osteogenisis.

3.5) Current Surface Modification Techniques

Successful surface treatment requires the development of an adequate bone-implant interface. Thus, not only are the properties of the base material and prosthesis design important, but the implant surface properties are also critical in regulating the interaction with bone tissue [118,119]. Thus, numerous techniques for surface modification of the materials that compose implants have recently been studied to make them more functional. These modifications can be subtractive (when portions of material are removed from the surface) or additive (when coatings are added over the surface), and both consist of changing the topography of the material, creating complex structures on it. Table 2 shows some of the techniques currently applied, according to their mechanism of action [121,121].

Table 2 - Currently used surface modification techniques.

Subtractive Methods	Additive Methods
Acid etching	Sol-Gel Coating
Laser Treatment	Electrophoretic Deposition
Grit-Blasting	Plasma Spraying
	Ion Deposition

Despite their relatively low expense when it comes to investment and industrial appeal, additive methods present a main limitation: the fragility of the coating created. If it disappears from the implant surface, then the base material is exposed, which can lead to undesirable reactions with the surrounding tissues and rejection of the prosthesis [120]. In fact, techniques like sol-gel or plasma spraying have been associated with biofilm formation, implant loosening and inflammation of soft tissue [122,123].

On the other hand, and despite presenting some interesting advantages, such as simplicity, low cost, and longevity, subtractive techniques also present important limitations. Excluding anodization laser treatment (no contact with the material) the most relevant setback is the possibility of surface contamination, which can damage the surface properties of the modified material [123].

It is thus important to find new surface modification methods, which overcome the mentioned weaknesses and allow for optimal surface functionalization. In fact, recent attention has been directed to the development of modified surfaces incorporated with biologically active coatings, acting as osteoactive

and antibacterial materials [34,24,124,125]. Additionally, the micro and nano texturing of surfaces, creating hydrophilic and cell-responsive materials, has also been the subject of study has of late [126-128]. Due to its fairly recent development, no long term clinical results have been obtained yet.

3.6) Proposed Hybrid Laser Surface Modification

As already mentioned, the processing technique proposed in this work is considered hybrid, that is, it is both additive and subtractive. It is a subtractive technique since portions of the material are removed from the surface by laser texturing, creating different structures on the surface of the samples by varying laser patterns and parameters. On the other hand, it is considered additive since different bioactive compounds are subsequently introduced on the surface of the material, initially deposited through the spin-coating and cold-pressing methods and then sintered and compacted by different techniques, explored in the next chapter.

3.6.1) Laser Technology

A laser is defined as a consistent and uniform monochromatic light beam with high energy and intensity (figure 14) [130]. To produce this energy beam, an energy source releases electrons into the active medium (liquid, gaseous or solid) which, when excited, release energy in the form of photons [130]. These photons are then reflected back and forth between two mirrors at both ends of the active medium, one that is fully reflector and another that is partially reflective, from where the photons leave the system and the laser beam is generated [130,131].

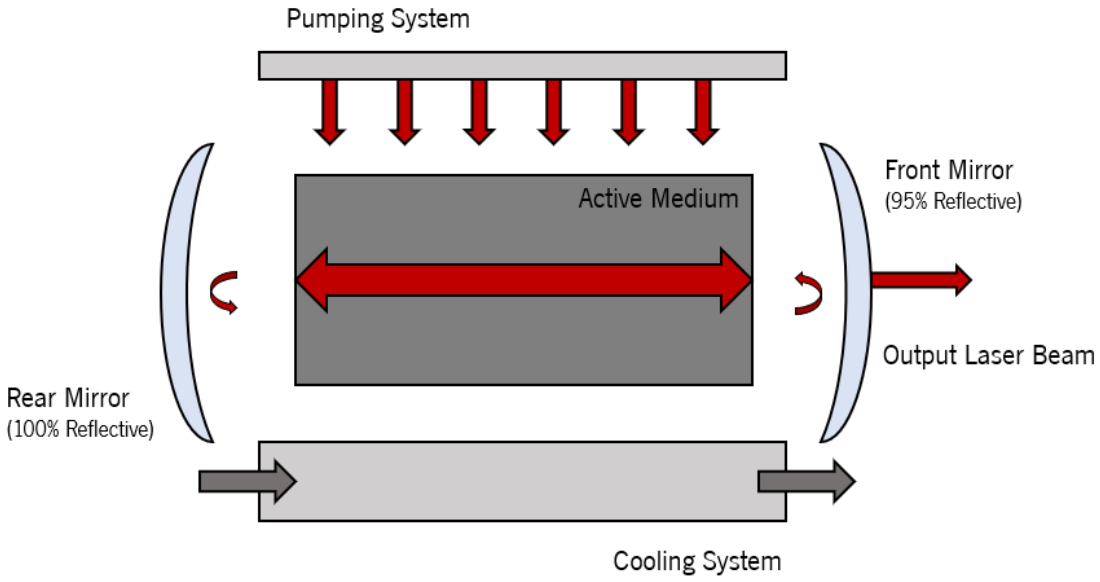

Figure 14 - Schematic illustration of radiation emission in a basic laser system.

Depending on the type of active medium used, lasers can be classified as solid-state (Nd:Yag, Nd:YvO4), gas lasers (CO2) or semiconductor lasers [131]. Most lasers can be used in a continuous or pulsed mode. Pulsed lasers (such as Nd:Yag lasers) are the most popular, since they possess a greater ability to control parameters, and the use of pulses allows heating and consequent ablation of a small volume of material quickly in a short period of time, that can range from micro-seconds to femto-seconds [128]. All energy is delivered in a single pulse and controlled by the Q-switch module, that defines the amount of energy present inside the active medium [131]. On the other hand, continuous lasers (such as CO2 lasers) adopt a gradual energy delivery with a constant output of power, a nonstop laser beam [128]. Figure 15 shows the comparison in practical effects between pulsed and continuous lasers.

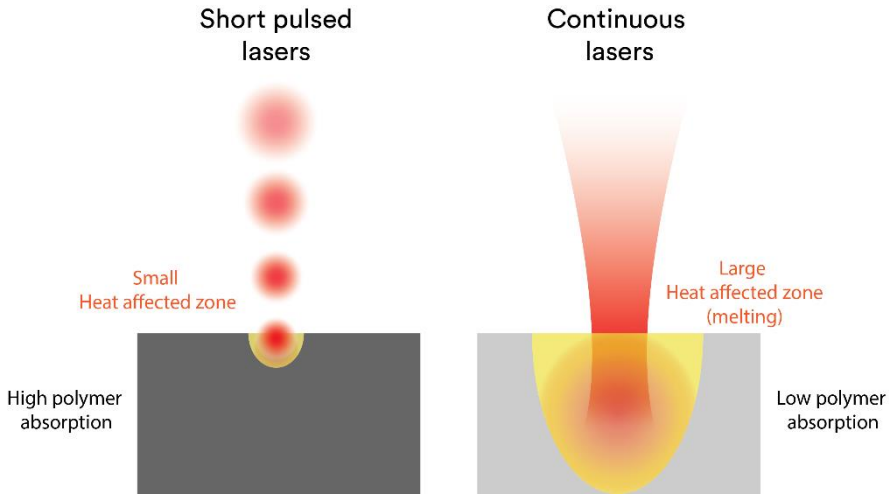

Figure 15 - Schematic representation of the practical effects between the operation mode of a pulsed laser and a continuous wave laser. Adapted from [132].

3.6.1.1) Laser Surface Texturing (LST) and Material Interaction

Laser surface texturing (LST) has emerged as a promising subtractive technique in the field of surface modification, due to its high versatility. The laser texturing process is based on ablation, which is the removal of material from a substrate by direct absorption of laser energy [126,133]. Usually discussed in the context of pulsed lasers, this mechanism allows the controlled vaporization of small portions of surface material, due to its reduced spot size. Depending on the laser beam parameters (pulse length, fluence and wavelength), the mechanisms for material removal may differ: at low fluence they include material evaporation and sublimation, while at high fluence heterogeneous nucleation of vapor bubbles leads to normal or explosive boiling. In all cases, material removal is accompanied by direct ejection of plume from the irradiated zone, that can contain liquid and material clusters of the substrate. At high

energies this plume may even be ionized, producing plasma [133]. A combination of ablation, surface melting and other thermal processes lead to changes in the material, such as surface texture, morphology and chemistry [133].

Material processing via laser is dependent on different process variables that directly affect the laser-material interaction and, consequently, the texturing quality and efficiency. Thus, the processing parameters (scan speed, power, number of passages, focal position, etc.) should be chosen in accordance with the material properties (density, absorptivity, thermal conductivity, etc.) and the laser beam conditions (wavelength, maximum power, spot size, etc.), so that the topography and chemistry of the textured materials can be optimized to the application in question [133,134].

As already discussed, subtractive methods currently applied to biomaterials do not allow precise control of the depth and detail of generated structures and patterns, only providing random textures, and can sometimes contaminate the surface of the biomaterial [135]. On the other hand, laser texturing allows the control and modification of sample roughness, thus creating different micro-textures and patterns with different morphologies by varying specific parameters such as power or speed [126]. It enables the removal of material quickly and very precisely, with low waste and no surface contamination since there is no contact between the material to be texturized and the laser (energy irradiation) [136]. Additionally, it is reagent free, has high temporal and spatial resolution and is a cost-effective technique [135].

In literature, fiber and yttrium-aluminum-garnet (YAG) based lasers are the most commonly used in the texturing of biomaterials. Figure 16 shows some examples of patterns produced via LST. In the context of biomedical applications, these lasers have been applied with success to improve wettability, friction, and even provide antibacterial properties [128,137,138]. Additionally, laser induced textures facilitate and guide cell orientation and growth [106,117,124], as well as facilitate the incorporation of bioactive materials on the surface of the samples [139]. Recent in vivo studies also show that textured implants promote a higher bone-to-implant contact, enhancing bone regeneration and improving the longevity of orthopedic implants [140,141]. Therefore, LST is considered a viable approach to improve the osteointegration rate, longevity, stability and performance of newly produced implants and prosthesis.

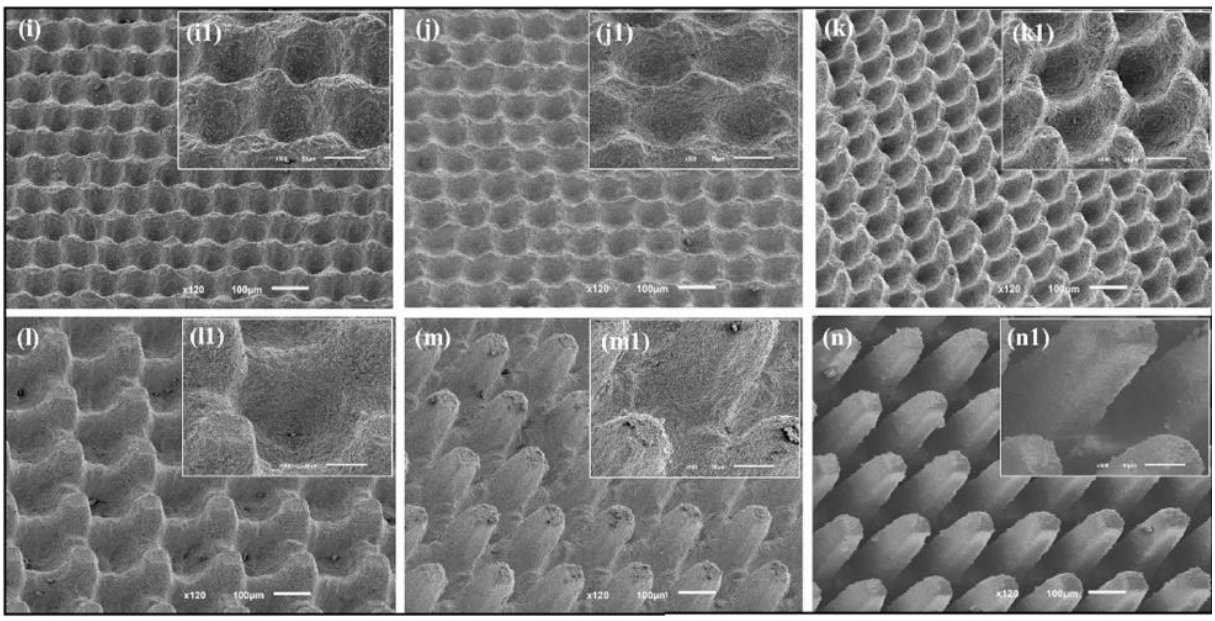

Figure 16 - Different structures produced by LST. The pattern used in the creation of all textures was the same, but the variation of laser processing parameters influences the final topography of the textured surface. Adapted from [128].

3.6.2) Incorporation of Bioactive Materials (Hap & MTA)

Bioactive materials are defined as compounds that are intended to interface with biological systems to evaluate, treat, augment or replace any tissue, organ or function of the body [142,143]. These materials have the capacity to stimulate cell differentiation and proliferation, as well as release bioactive molecules that stimulate tissue regeneration, typically bone tissue [144]. The mechanism of bone bonding is due to the formation of a hydroxyapatite layer (Hap) on the surface of the material after immersion in body fluid. Since this layer is similar to the apatite layer present in the human bone, a strong bond is formed [144]. Therefore, it is important for a bioactive material to have some biological characteristics, although not essential, as reported by Sheperd et al: osteoconduction, by supporting the attachment of new osteoblasts and providing a stable structure for cell migration and blood vessel orientation; osteogenesis, by allowing the production of minerals that calcify the collagen matrix, forming the substrate for new bone; osteoinduction, by inducing the differentiation of stem cells into bone-forming osteoblasts; osteointegration, where a chemical bond between the surface of the material and the bone is formed, without an intervening fibrous tissue layer [142,144,145].

A vast number of bioactive materials have been tested and described in literature. Among them, synthetic Hap presents itself as one of the most popular compounds. This material has enormous potential for bone tissue engineering, due to its chemical similarity with the mineral component of the human bone [146]. Typically distributed in ceramic form, Hap bioactivity lies in the formation of an

additional calcium phosphate layer on its surface, keeping the bulk material intact [147]. Calcium phosphate then increases bone integration, while also preventing the formation of a fibrous layer [148,149]. The chemistry of Hap relies on its Ca/P ratio, which can influence thermal stability, solubility and consequent biological response [145]. The optimal Ca/P ratio for Hap is 1.67 and derivations of these value are associated with the presence of impurities, such as tricalcium phosphate (TCP) or calcium oxide (CaO). In fact, Guimarães et al [106] evaluated cell adhesion of laser sintered Hap in zirconia surfaces, comparing cell viability in samples with different Ca/P ratios. They confirmed that ratios around 1.67 performed better than their counterparts, both in terms of quantitative and qualitive analysis, while past this number the higher the ratio, the poorer the results. The creation of Hap coatings typically involves the application of high temperatures, sintering the material into a compact film. However, this process can decompose the bioactive material if the temperature used is too high, transforming the hydroxyapatite into other calcium phosphates, such as α/β-TCP or tetracalcium phosphate ($Ca_4(PO_4)_2O$). The products of this decomposition are based on the Ca/P ratio [150].

Another material that has gained popularity in recent years, although still less explored in the literature compared to more conventional materials, is mineral trioxide aggregate (MTA). MTA is a powder consisting of fine hydrophilic particles of tricalcium silicate, tricalcium aluminate, tricalcium oxide, silicate oxide and other minerals, that harden when in contact with water. This hydration of the powder, more specifically the transformation of calcium oxide into calcium hydroxide, results in the formation of a colloidal gel, which forms hard structures upon solidification (approximately 4 hours) [151]. It was originally created from traditional Portland cement (PC) and is widely used in dentistry. A vast number of studies have proven the excellent biocompatibility and minimal cytotoxicity properties of MTA, its antibacterial nature and favourable osteoblast response [152-154]. For example, de Deus et al produced a study in which they studied the *in vitro* cytotoxic effects of two different brands of MTA (Pro-Root MTA and MTA Angelus), as well as PC, on endothelial cells [154]. It was concluded that, after a brief initially elevated cytotoxic effect, a positive reaction from the material was achieved, resulting in high biocompatibility and cell culture proliferation after 72h (figure 17).

However, all these bioactive materials have a clear disadvantage: they are brittle composites with low fatigue strength, so they are unable to withstand the mechanical loads imposed on the knee, and they cannot be directly used as a base material in the prostheses that are to be implemented [155]. In fact, the compressive strength of MTA tends to increase with time as it sets, evolving from 40MPa to about 70MPa [156], while the ceramic nature of apatite cements, such as Hap, confers them a brittle nature

(about 20 to 50MPa) [157]. Since the compressive strength of bone can be as high as 150MPA, many efforts have been made to incorporate these bioactive materials into more resilient base materials.

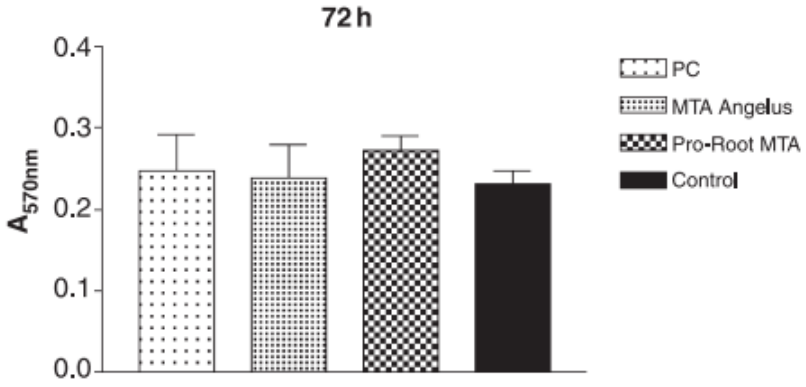

Figure 17 - Cell viability tests comparing different types of MTA powder. All bioactive samples obtained absorbance values higher than the control group, which is a testament to the biocompatibility capacity of these materials. Adapted from [154].

3.6.2.1) Functionalization Techniques

As previously mentioned, it is important to find solutions that allow the incorporation of the bioactive materials with poor mechanical properties into bulk materials that can sustain the weight of the body during movement. It is crucial that the method used gives rise to high adhesion between the created coating and the substrate. Otherwise, shear stresses created during implant insertion may lead to implant separation, compromising the whole process [158]. The use of coatings is one of the strategies used to enhance biocompatibility and osteointegration without changing the base material, as it is thoroughly present in literature. It consists in the coverage of a surface with a bioactive material and can be done through different strategies, such as plasma spraying, deep-coating, sol-gel, electrodeposition, etc [159-162]. Post-treatments after coating are also widely applied to optimize coating properties. Sintering of the material tends to form flake-like morphologies, and is predominantly used to confer integrity and density to the bioactive coating [159-162].

In this work, the hydroxyapatite coatings are established through spin-coating, while the sintering process is performed by two different methods: conventional sintering and laser sintering. Alternatively, the MTA coatings are created through cold-pressing, and since the material hardens when hydrated sintering was not required.

3.6.2.1.1) Spin-Coating & Cold-Pressing

Spin coating is one of the simpler methods for fabricating a film on a substrate. This technique uses centrifugal force to rapidly apply a thin and uniform film out of a solution and onto a solid surface, spinning out the precursor solution over the edge of the support [163,164]. The spin-coating process starts with the dilution of the material that is to be deposited in a solvent. The solution is loaded in the centre of the substrate surface, which is then spun at high speed [164]. The resulting centrifugal force drives the solution to spread in a film where the solvent evaporates to produce a uniform coating layer on the substrate, as shown in figure 18 [164]. The thickness of the membrane can range from nanometers to several micrometers and is defined by the evaporation rate, the spin rate and the nature of the solution (viscosity) [164]. The advantages of this procedure are the low operation cost, uniformity, rapidness and the ability to control film thickness [165].

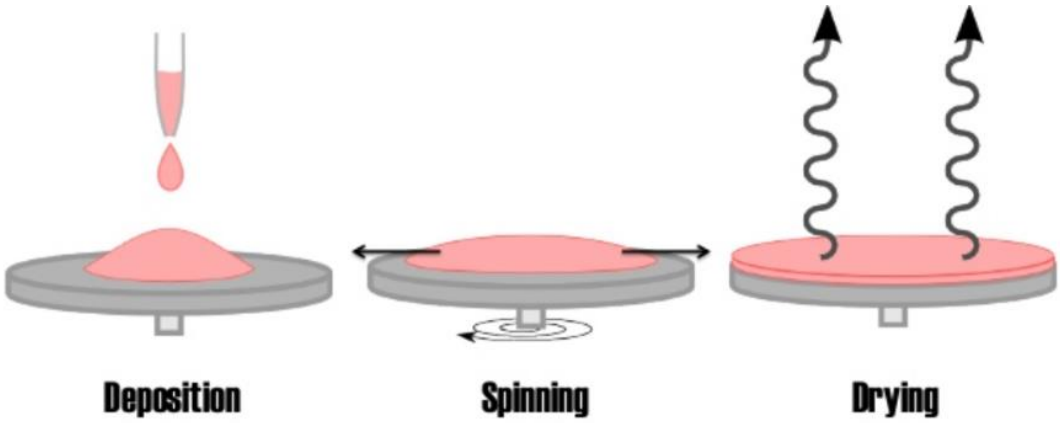

Figure 18 - Different stages of the spin-coating procedure. Adapted from [166].

Cold pressing is the method of applying pressure upon a column of loose powders in order to form a solid green compact. The powder is placed in a closed die, where upper and lower punches (axial) compact it by using enough pressure to bind the particles together. Since solid particles tend to flow mainly in the direction of the applied pressure, a solid material is formed and then ejected from the die [167]. The time and pressure used are dependent on the physical properties of the powder, such as particle size, shape, composition and size distribution, as excessive pressure can present some complex problems, such as punch and die fractures [167]. Figure 19 summarizes the cold-pressing technique.

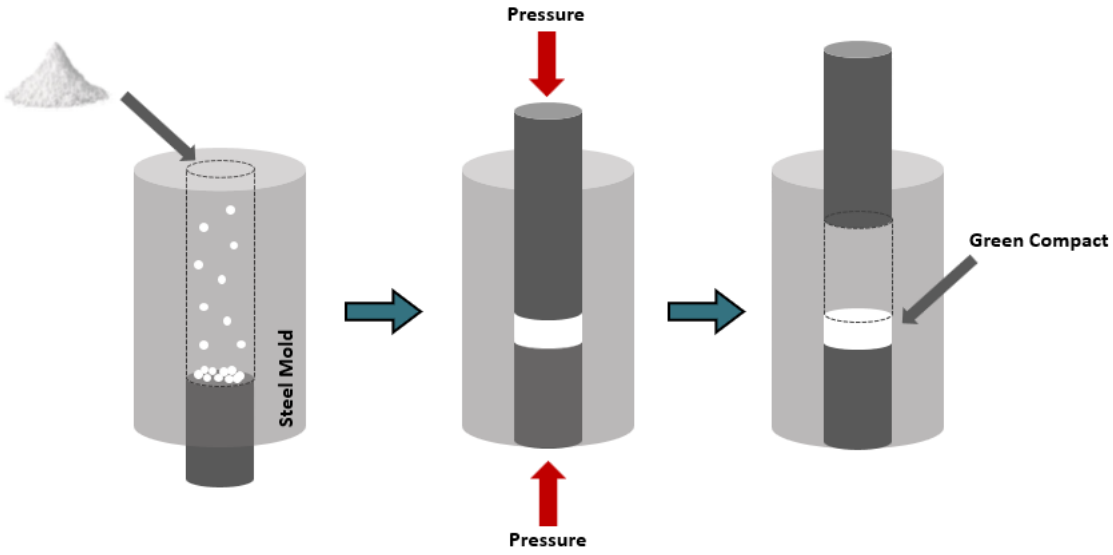

Figure 19 - Different stages of the cold-pressing technique.

3.6.2.2.1) Conventional and Laser Sintering

Sintering is a thermal process that consists in the conversion of loose fine particles of a given material into a solid, coherent mass by mechanisms of heat and/or pressure, without fully melting the particles [168]. This process eliminates most pores and improves binding among grains, which in turn have an effect in physical, chemical and biological performance, creating coatings with increased density, strength, ductility, corrosion resistance and other important properties [169]. Figure 20 shows a scheme representation of the sintering process effect on ceramics. Sintering time, pressure, atmosphere, temperature and heating/cooling rate are fundamental variables that affect the physical and mechanical properties of the coating. For example, at higher temperatures fast and irregular grain growth occurs, while lower sintering temperatures lead to smaller sintering times and consequent limited grain growth [170]. Different atmospheres can be deployed during sintering, such as hydrogen, argon, vacuum (for reactive materials) and other inert gases, while the application of pressure accelerates the densification process [170]. Two distinct types of sintering are studied in this work: laser sintering and conventional sintering.

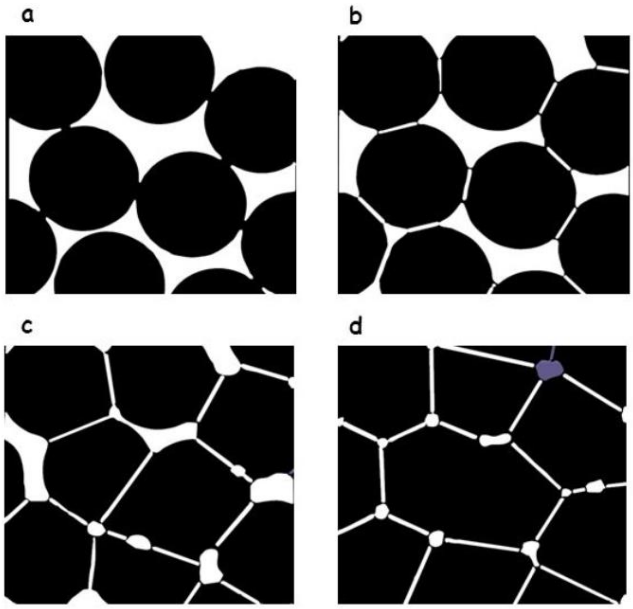

Figure 20 - Sintering process effect on ceramics. The high temperatures/pressure compact the grains, reducing the space between them and creating a hardened material with improved mechanical properties. Adapted from [171].

Selective laser sintering is an addictive technique that uses a high-power CO2 laser as the heat source for the sintering of powdered material. This is a promising technique since it allows the sintering of selected areas of granules (previously modelled in CAD-computer assisted design software) in a fast, layer-by-layer process, creating hardened and very precise structures [172]. The CO2 laser is a continuous-wave laser that produces the sintering beam in a sealed glass tube filled with carbon dioxide and other gases, through the reaction of high voltage with the gas particles. These particles are excited and release energy, creating an infra-red beam that is then continuously reflected inside the active medium until it has enough power to be vertically directed towards the surface of the material [173].

On the other hand, conventional sintering is the simplest technique, which simply involves the heating of any powder compact, previously prepared at ambient temperature, without the application of any external pressure. It is typically conducted in box or tube furnaces under different atmospheres (oxidizing, inert, vacuum) [174], and is considered a uniform, cheap and high yielding process. However, it can be time and energy consuming [170].

CHAPTER III

MATERIALS AND METHODS

This chapter explores the different stages of the experimental procedure of the present work. The materials used are presented and the modification processes are described, explaining the different strategies used and the various parameters, using different schemes. Additionally, morphological and mechanical tests are presented and elaborated.

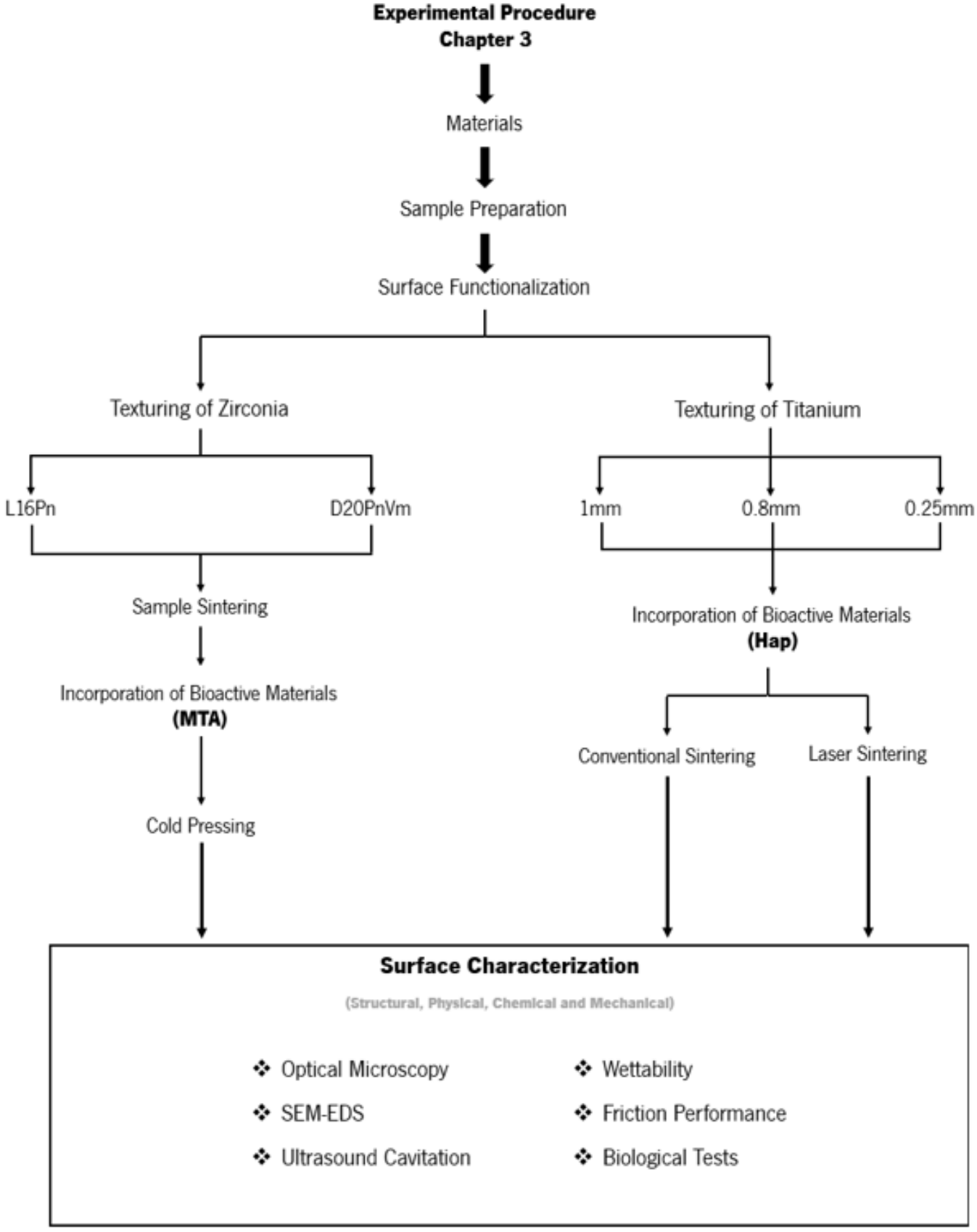

Figure 21 - Experimental Procedure of the present work.

1) Experimental Procedure

1.1) Zirconia

1.1.1) Green Zirconia Samples Preparation

The initial zirconia samples were produced using the cold-pressing technique. The substrate used was partially Yttria-stabilised zirconia powder (Y-PSZ) (Yttrium oxide [3 mol%]) (TZ-3YB-E Tosoh, Tokyo, Japan). Additionally, the quantitative chemical composition according to the supplier is represented in Table 3, while the SEM images of the Y-PSZ powder are presented in Figure 22.

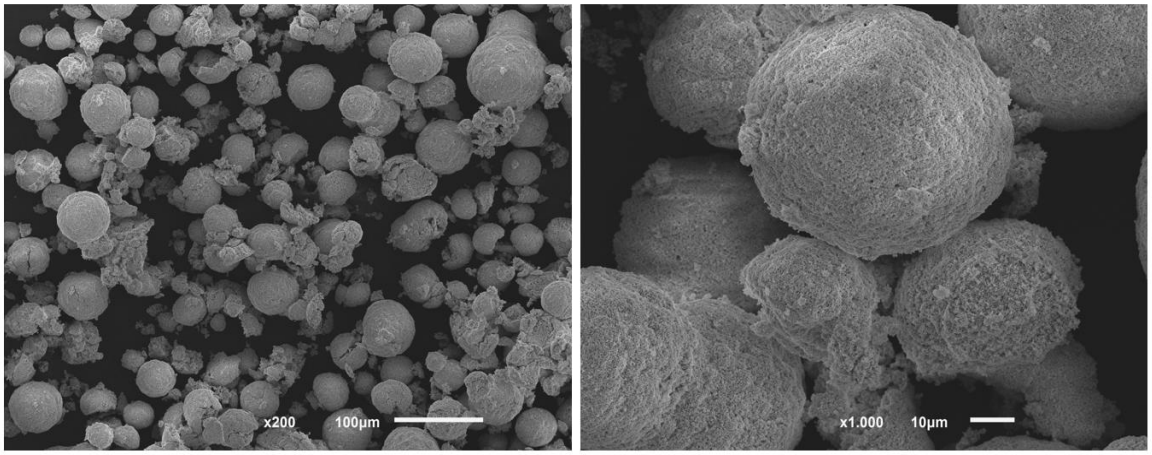

Figure 22 - SEM images (x200, x1000) of the zirconia powder.

Table 3 - Chemical composition of the zirconia powder used, according to supplier.

CHEMICAL COMPOSITION (%)	
$ZrO_2 + HfO_2 + Y_2O_3$	> 99.90
Y_2O_3	5.15 ± 0.20
Al_2O_3	0.25 ± 0.10
SiO_2	≤ 0.02
Fe_2O_3	≤ 0.01
Na_2O	≤ 0.04

In this procedure, described in the previous chapter, 1 gram of zirconia powder was weighed and inserted into a cylindrical steel mould, 10 mm in diameter, and lubricated with a small amount of zinc stearate. A pressure of 200 MPa was applied to it for about 30s. The pressure was then uniformly removed, and green zirconia specimens with a diameter of about 10 mm and a height of about 4 mm

were obtained. Additionally, the surface of each sample was lightly polished with sandpaper (grit 2000) to remove any marks or scratches that might invalidate the textured pattern. Figure 23 presents the initial samples obtained.

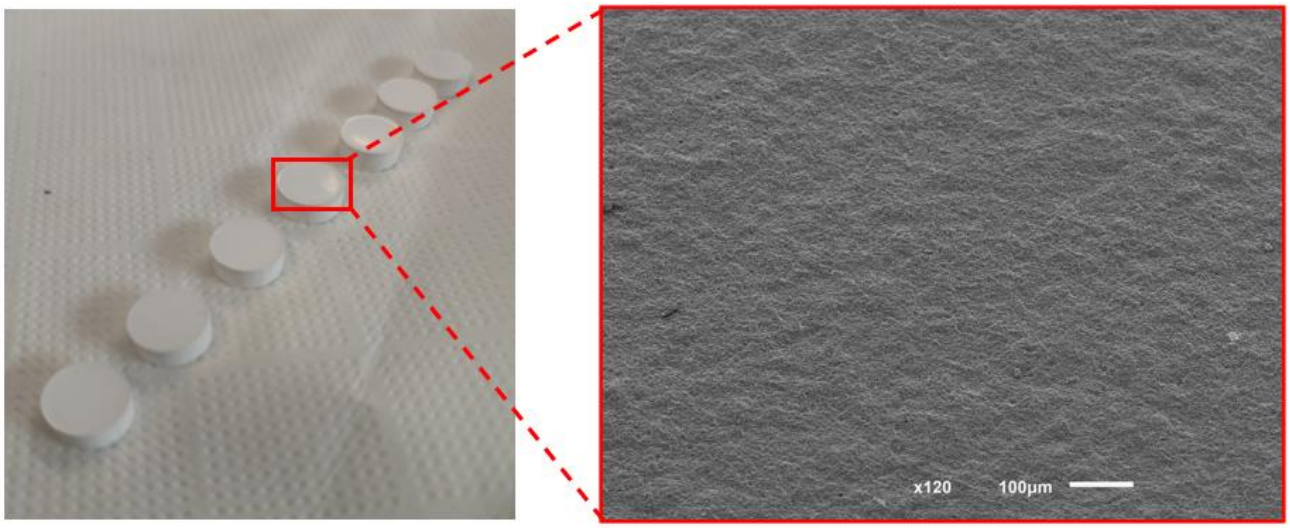

Figure 23 - Initial zirconia samples, produced by cold-pressing, as well as the respective surface SEM image (x120).

1.1.2) Laser texturing of the green zirconia samples

After the production of the green samples, the laser surface texturing was performed. For that, the Nd:YAG laser (OEM Plus 6W, SISMA, Italy), represented in figure 24, was used. A wavelength of 1064 nm and a laser pulse duration of 35 ns was used for all the surface texturing present in this work. A galvanometer scanning head (2-axis subsystem Focusshifter, model MS-10 [Y] D1 V2, from RAYLASE) was used to focus the beam on the surface of the specimens, and the height used was 32.8 cm. Furthermore, it should be noted that the entire process was carried out at normal atmospheric pressure and with constant air renewal, using a fan and a compressed air jet, in order to remove any debris that might accumulate on the surface of the sample. No inert gases were employed in this work. Detailed laser specifications can be consulted in table 4.

As seen in figure 24, the laser setup integrates a computer-control station that regulates the texturing process by a software designated Sisma Laser Controller (SLC). This software allows the user to define the processing parameters, as well as to import the files containing the patterns and designs chosen for the intended work.

Table 4 - Nd:YAG laser specifications.

LASER SPECIFICATIONS:	VALUES
Average Output Power [W]	6
Wavelength [nm]	1064
Laser Technology	Nd
Repetition Rate Range [kHz]	20
Pulse Width [ns]	35
Max Pulse Energy [mJ]	0.3
Cooling System	Forced Air-Cooling
Power Supply	230V, 50/60 Hz

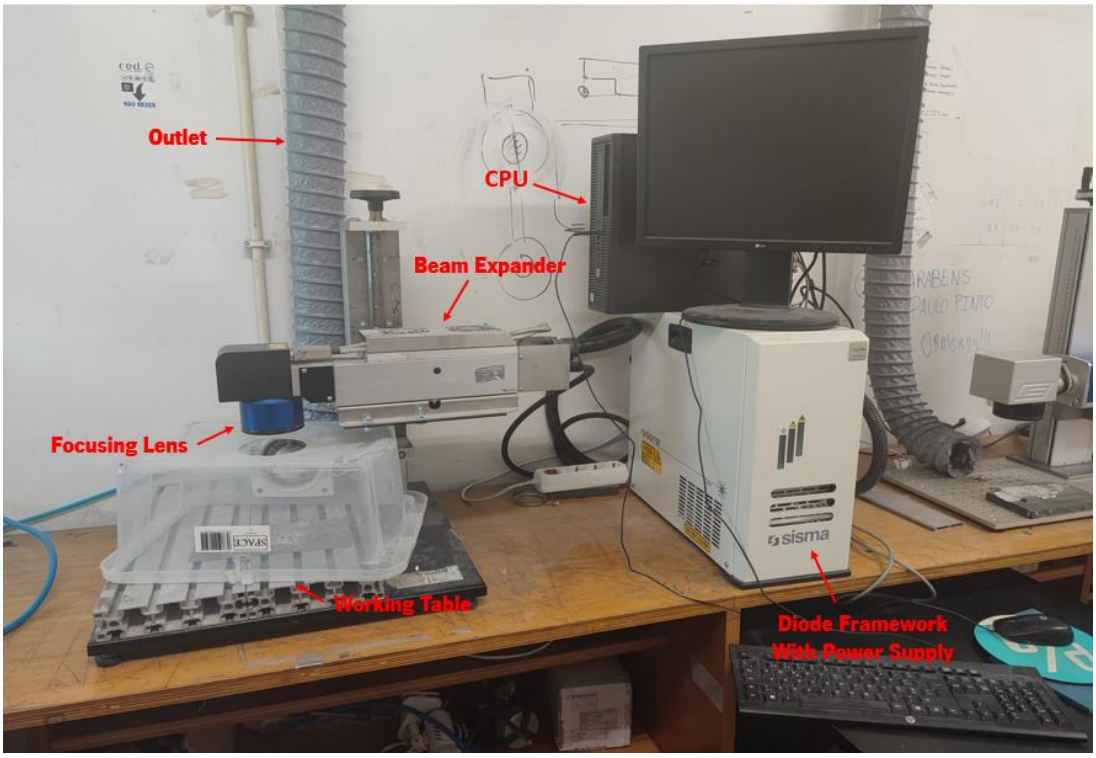

Figure 24 - Nd:YAG Laser system setup used in the experimental work (CMEMS Laboratory of the Mechanical Engineering Department of University of Minho).

1.1.2.1) Texturing: Design, Strategies and Parameter Optimization

Considering previous studies conducted in this research field [28,34,41,42], cross-hatch patterns were designed in order to increase bone-implant contact. Research has shown that this type of pattern

increases surface adhesion between bone and implant, improving mechanical stability and interlocking [76]. Figure 25 represents the general scheme of the patterns used and the resulting topography of the sample after texturing.

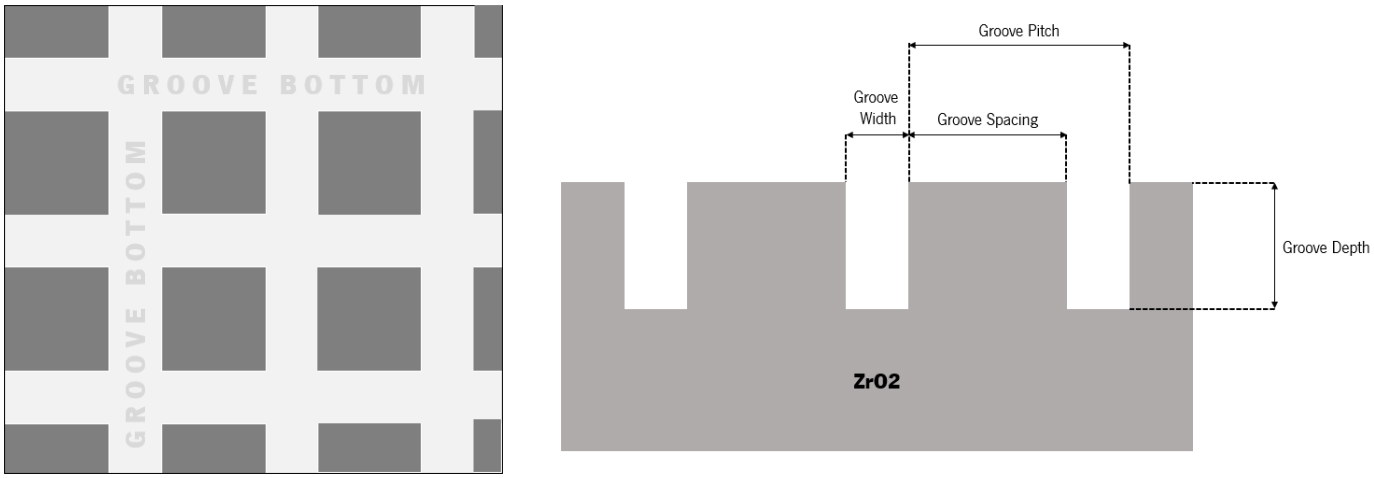

Figure 25 - Schematic representation of the top-view and side-profile of the zirconia samples after texturing.

The patterns used were created through a computer design system, and each file was later transferred to the laser computer control-station. In this way, it was possible to replicate the patterns generated on the surface of the samples, varying only some parameters of the laser, as described below.

In this work two different strategies were used to produce the textured samples:

- **Strategy 1:** laser texturing of the zirconia samples using the **L16Pn pattern**, in which the parameters of laser power(**n**) and number of laser passages were varied.

- **Strategy 2:** laser texturing of the zirconia samples using the **D20PnSm pattern**, in which the parameters of laser power(**n**), scan speed(**m**) and number of laser passages were varied.

The main difference between the two proposed textures is the spacing between the lines: the L16Pn design textures 16 lines for about 120 µm of material, resulting in a line spacing of around 7.5 µm, while D20PnSm design has 20 µm of line spacing. This variation in the patterns will have effects on the dimensions and number of grooves textured into the sample, and, consequently, alter parameters like groove spacing and groove width. Additionally, while one single major line of the L16Pn design contains 16 other sub lines, the YAG laser passes only on time for each major line of the D20PnSm texture, which

will impact the topography and depth of the created microstructures. Figure 26 represent the scheme of the two different textures.

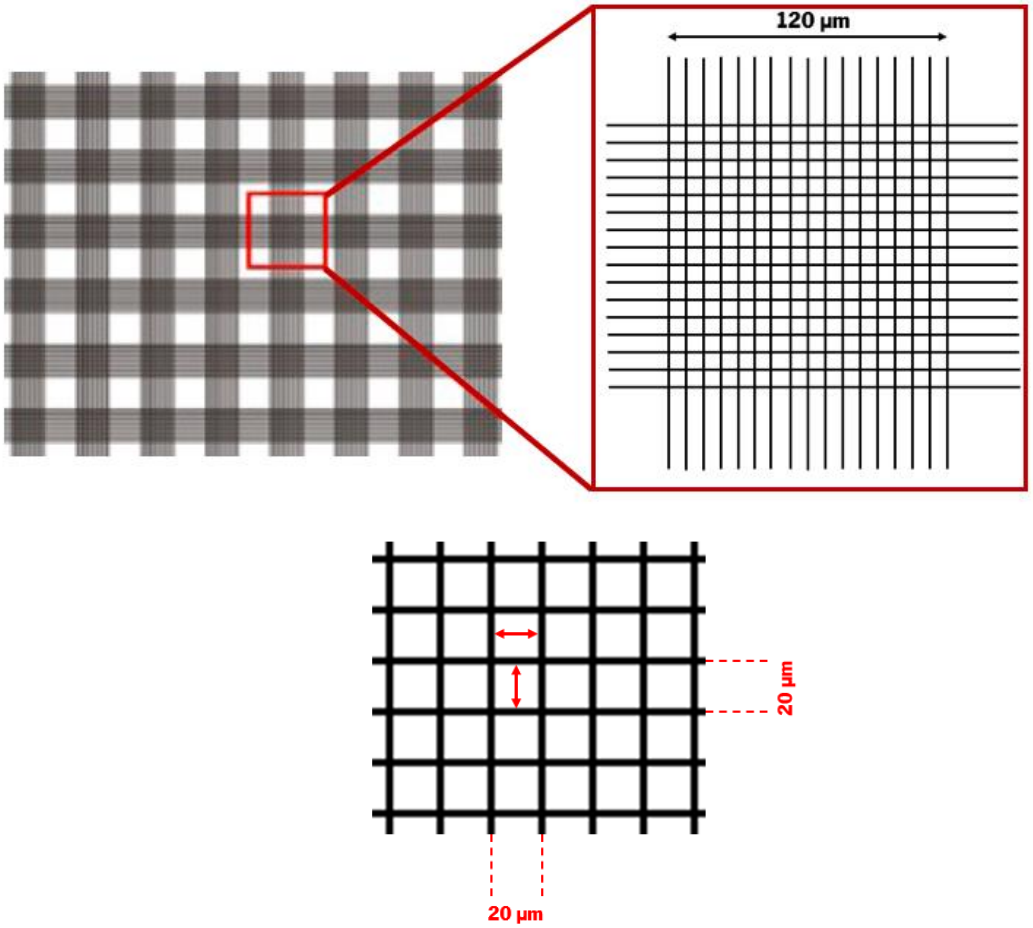

Figure 26 - Designs used in the texturing of the zirconia samples: L16Pn (top) and D20PnSm (bottom).

A few preliminary studies were conducted in order to understand how the laser system operated and evaluate the influence of the laser parameters in the microtexturing process. This optimization process was focused on three major parameters: laser power, scan speed and number of passes. As indicated in each texture, strategy 1 involves only the variation of laser power (Pn) and number of passes, while in the second strategy laser power (Pn), scan speed (Sm) and number of passes were studied. The remaining parameters like fill spacing, wobble amplitude and wobble frequency were kept constant. For the reader to understand the meaning of each adjusted variables, a brief description is presented below:

- **Laser Power**: represents the laser beam energy delivered per pulse, expressed in the percentage (%) of maximum laser power.

- **Scan Speed**: represents the marking speed at the leading edge of the beam front (in mm/s);
- **Passes**: corresponds to the number of scans carried out by the laser during processing.

Therefore, tables 5 and 6 represent the different combinations that were tested for both mentioned patterns.

Table 5 - Laser parameter combinations tested for the D20PnSm pattern.

Pattern	Power (%)	Number of Passes	Scanning Speed [mm/s]	Fill Spacing [mm]	Wobble Amplitude [mm]	Wobble Frequency [Hz]
$D20P_{10}S_{128}n=1$	10	1	128	0.03	0	75
$D20P_{20}S_{128}$ n=1	20					
$D20P_{20}S_{128}$ n=2		2				
$D20P_{20}S_{128}$ n=3		3				
$D20P_{20}S_{128}$ n=5		5				
$D20P_{20}S_{128}$ n=6		6				
$D20P_{20}S_{128}$ n=7		7				
$D20P_{25}S_{128}$ n=1	25	1				
$D20P_{30}S_{128}$ n=1	30					
$D20P_{35}S_{128}$ n=1	35					
$D20P_{40}S_{128}$ n=1	40					
$D20P_{45}S_{128}$ n=1	45					
$D20P_{10}S_{32}$ n=1	10		32			
$D20P_{10}S_{32}$ n=2		2				
$D20P_{10}S_{32}$ n=3		3				
$D20P_{10}S_{32}$ n=5		5				
$D20P_{10}S_{32}$ n=7		7				
$D20P_{20}S_{32}$ n=3	20	3				
$D20P_{20}S_{32}$ n=5		5				
$D20P_{20}S_{32}$ n=7		7				
$D20P_{10}S_{48}$ n=1	10	1	48			
$D20P_{10}S_{64}$ n=1			64			

Table 6 - Laser parameter combinations tested for the L16Pn pattern.

Pattern	Power (%)	Number of Passes	Scanning Speed [mm/s]	Fill Spacing [mm]	Wobble Amplitude [mm]	Wobble Frequency [Hz]
$L16P_{25}$ n=1	25	1	200	0.008	0.008	550
$L16P_{30}$ n=1	30					
$L16P_{35}$ n=1	35					
$L16P_{35}$ n=2		2				
$L16P_{35}$ n=3		3				
$L16P_{40}$ n=1	40	1				
$L16P_{40}$ n=2		2				
$L16P_{40}$ n=3		3				
$L16P_{45}$ n=1	45	1				
$L16P_{45}$ n=2		2				
$L16P_{45}$ n=3		3				
$L16P_{50}$ n=1	50	1				

1.1.3) Sintering of Textured Zirconia Samples

After laser texturing, the samples were sintered using a high temperature furnace (Zirkonofen 700, Zirkonzahn, Italy), as represented in figure 27. The sintering temperature used in this work was 1500°C, as indicated by the supplier, with a heating/cooling rate of 8°C/min and a holding time of approximately 2 hours. The thermal cycle, represented in figure 27, was chosen according to the supplier requirements.

The sintering of the samples was carried out after the texturing process in order to preserve the physical properties of the material, decreasing the probability of the formation of micro-cracks due to excessive power or number of passes, as stated in literature [177]. Since sintering promotes zirconia compaction, the samples obtained at the end of this process had reduced dimensions – 8 mm in diameter and 3.25 mm in height, due to a 45% volume retraction and a 20% linear retraction.

After sintering, all the samples were cleaned in isopropyl alcohol using ultrasound technology, in order to remove possible debris or surface contamination. This process consists in the use of high-frequency, high-intensity sound waves in a liquid to facilitate/enhance the loosening and rinsing of

residual matter [175]. Throughout this work, the ultrasound cleaning of various samples is always performed using the same conditions: 100 W of power and 2 minutes of cleaning duration.

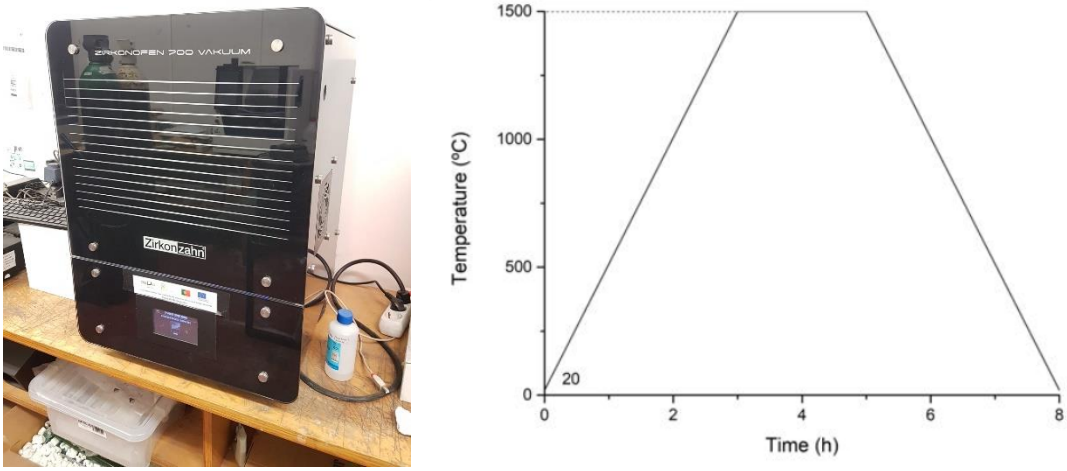

Figure 27 - Zirkonzahn furnace used in the sintering of the green zirconia samples (left) and the respective thermal cycle (right).

1.1.4) Coating of Bioactive Materials

1.1.4.1) MTA

After the sintering of the textured samples, the bioactive MTA (MTA Angelus ®) coating was produced and applied to the samples, by means of cold pressing. Figure 28 presents the SEM images (x1000, x5000) of the MTA powder, with a grain size of 12 μm, while table 7 indicates the chemical composition of said material, according to supplier.

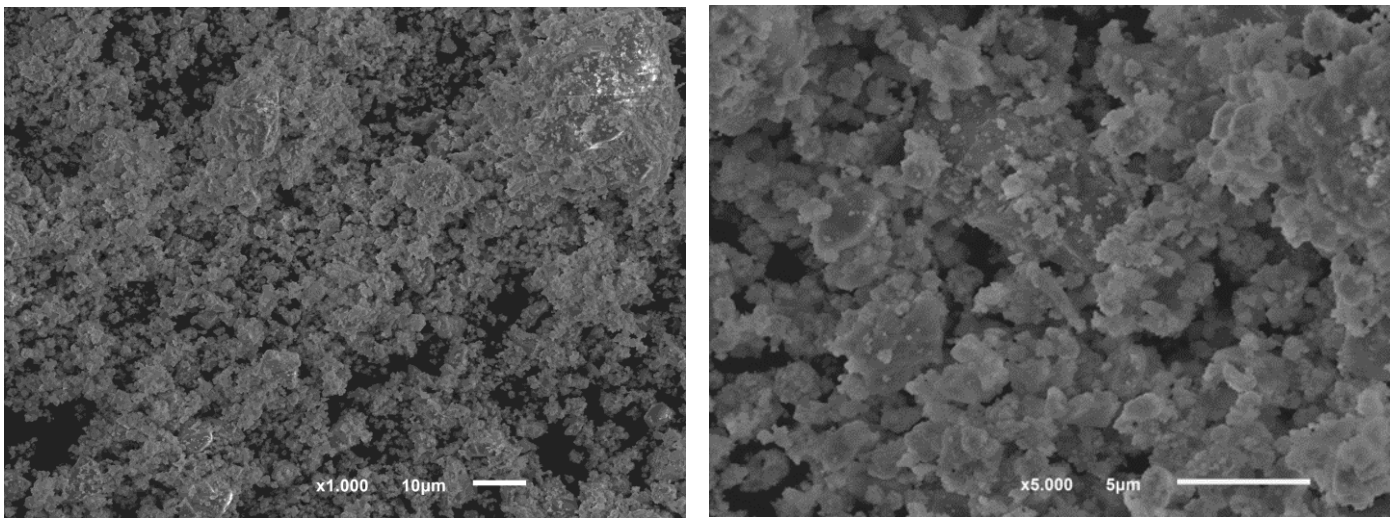

Figure 28 - SEM images (x1000, x5000) of the MTA powder.

Table 7 - Chemical composition of the MTA powder, according to supplier.

Elements	CaO	SiO_2	Bi_2O_3	Al_2O_3	MgO	SO_3	Na_2O	Cl	$H_2O + CO_2$
Wt %	49.20	18.58	8.26	4.48	0.64	0.19	1.32	0.51	16.82

In this sense, a device (represented in figure 29) was created, in order to facilitate the coating of the samples and improve its stability and adherence to the substrate. This consists in the use of parallel bars attached to a metallic support through springs, that allow the adjustment of the pressure on the samples. Therefore, the functionalization process can be divided into two main steps: the coating of the samples, and the pressing and compaction of said coating.

MTA Angelus powder was prepared in accordance with the instructions and quantities provided by the supplier. Therefore, 1 spoon (0.2 g) of the powder was mixed with 0.14 mL of distilled water and mixed for about 30 seconds until the mixture became homogeneous and similar to wet sand. Afterwards, the mixture was applied to the textured surface of the sintered samples, using a spatula, and placed inside small blue tube strips. These strips were then placed under the intermediate screws of the created device, where the pressure will act and compact the material. Finally, the springs are tightened, creating pressure on the screws, applied for about 3-4h. After this, the samples are removed and kept inside the tubes for another 24h, until they are fully compact, and extracted.

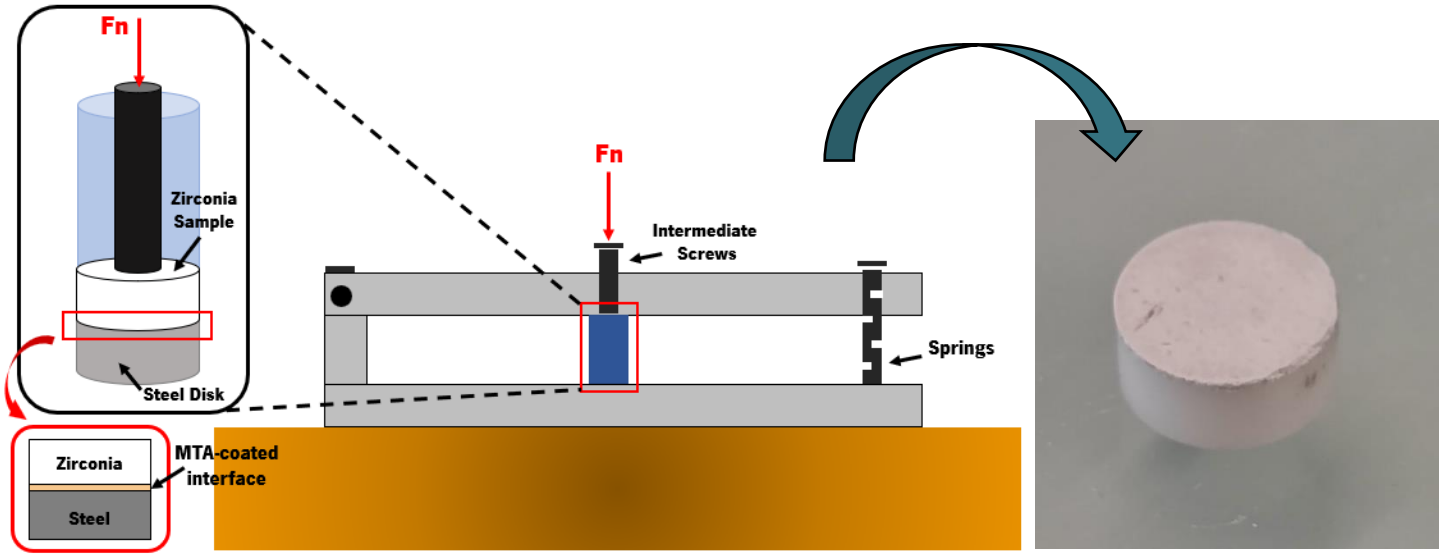

Figure 29 - Schematic representation of the device created to produce the MTA coatings in the zirconia samples, as well as the resulting MTA-coated sample.

1.2) Titanium Alloy: Ti-6Al-4V

1.2.1) Initial Titanium Samples

The titanium samples were obtained by cutting an 8 mm diameter Ti-6Al-4V bar into several discs, each about 2.5 mm high. The discs were subsequently polished with a sandpaper of mesh 280 and grit size 46 µm in order to remove any marks, scratches or surface contamination that could interfere with the final results. Figure 30 represents the obtained titanium samples, while Table 8 presents the chemical composition of said samples, obtained from EDS technology.

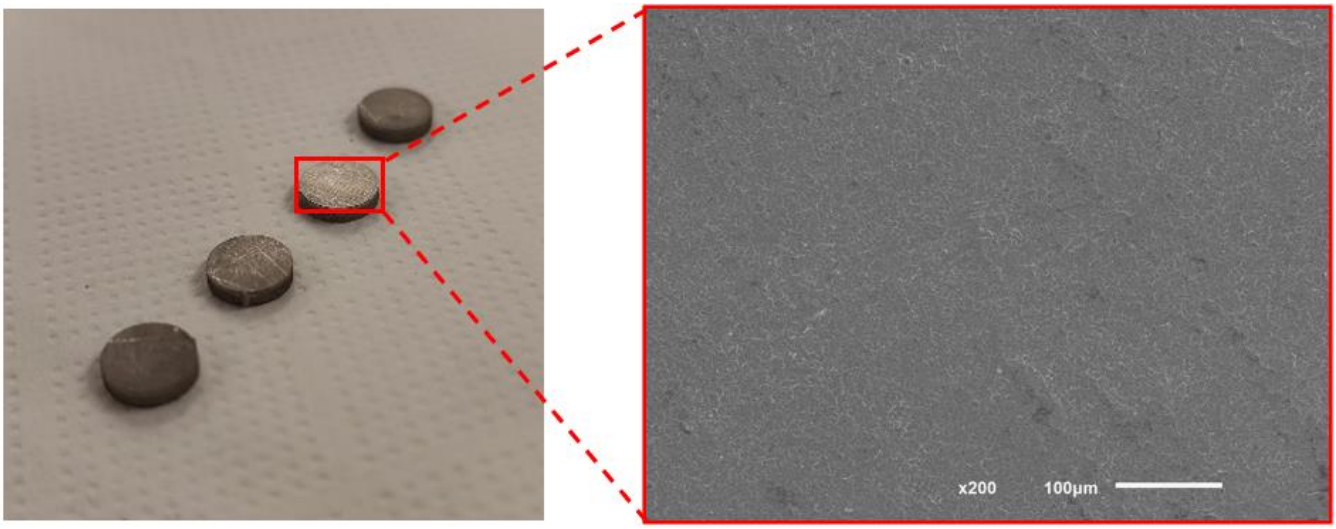

Figure 30 - Initial Ti6Al4V samples obtained, as well as the respective surface SEM image (x200).

Table 8 - Chemical composition of the initial titanium samples, obtained through EDS.

ELEMENTAL COMPOSITION	Ti	O	Al	V
Wt (%)	78.2	12.7	5.6	3.6

1.2.2) Laser Texturing of the Titanium Samples

After obtaining and polishing the samples, their surface texturization was performed. For that, a Nd:YV04 laser with a working wavelength of 1064 nm and a laser pulse duration of 10 ns was used for all titanium samples textured in the present work. The laser is represented in figure 31 and the respective specifications are represented in table 9. The laser was focused on the surface of the sample through a focusing unit, with an initial focusing height of 11.1 cm. It is important to point out that, due to the loss

of material by the texturing, the laser becomes slightly blurred at the end of each pass, so the focusing height was adjusted to 11 cm at the beginning of the eighth pass for the samples textured with two of the three patterns that will be mentioned next.

Furthermore, and similarly to the procedure used for zirconia, laser texturing was performed at normal atmospheric pressure and with constant air renewal using a fan and a compressed air jet in order to remove any debris that may have accumulated on the surface of the sample. As seen in figure 30, the laser setup also integrates a computer-control station that regulates the texturing process.

Table 9 - Nd:YV04 Laser specifications.

LASER SPECIFICATIONS:	VALUES
Maximum Output Power [W]	30
Wavelength [nm]	1064
Laser Technology	Nd
Repetition Rate Range [kHz]	20
Pulse Width [ns]	10
Spot Size (mm)	0.01
Cooling System	Forced Air-Cooling

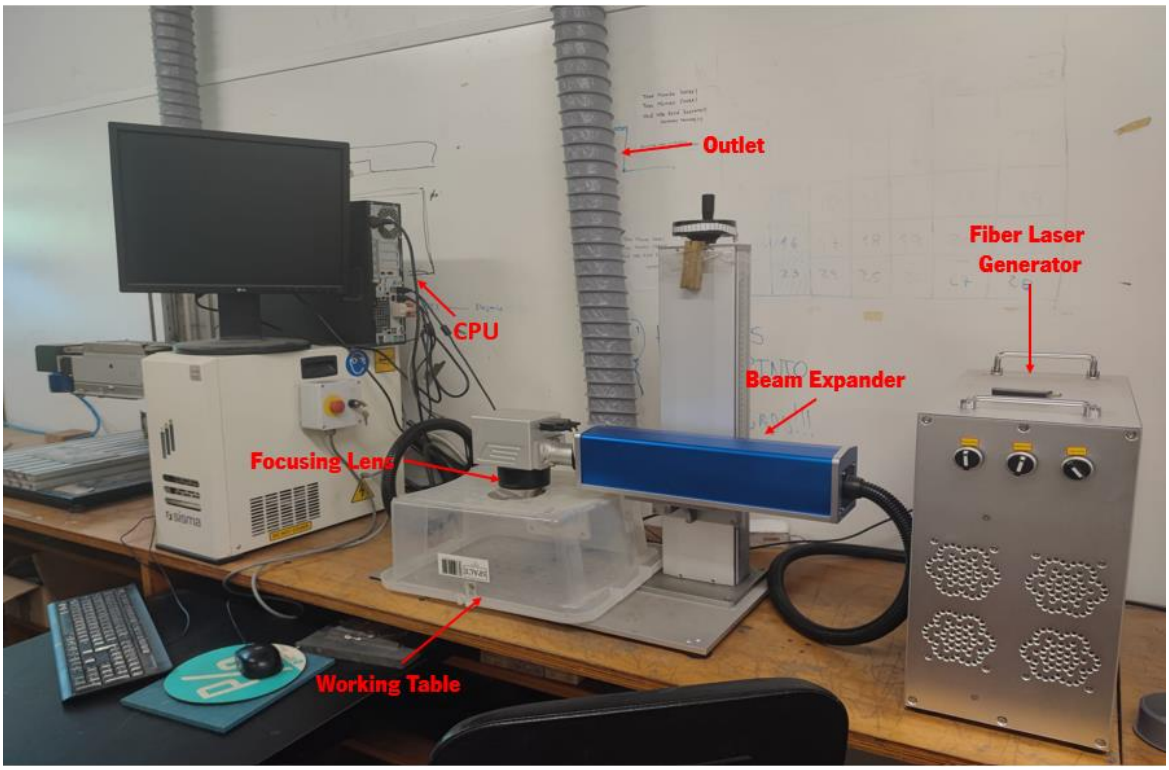

Figure 31 - Nd:YV04 Laser system setup used in the experimental work (CMEMS Laboratory of the Mechanical Engineering Department of University of Minho).

1.2.2.1) Texturing: Design and Strategies

Alike the procedure used for zirconia, the patterns used in the texturing of Ti-6Al-4V samples are based in cross-hatch patterns, such as those schematically represented in figure 32. These patterns were created through a computer design system, and each file then transferred to the laser computer-control station. However, for titanium, 3 different strategies were used:

- **Strategy 1**: laser texturing of the titanium samples using the **1 mm pattern**;
- **Strategy 2**: laser texturing of the titanium samples using the **0.8 mm pattern**;
- **Strategy 3**: laser texturing of the titanium samples using the **0.25 mm pattern**;

Identically to the strategies used in the zirconia samples, the main difference between the three texturing patterns is the distance between the lines. In fact, and since the marking textures were produced using the laser texturing software EZCAD, the design line spacing used varied in accordance with each strategies name, and this value expresses the length of one ridge and the groove between the next, as simplified in figure 32. Therefore, this length is of 1 mm in strategy 1, 0.8 mm in strategy 2 and 0.25 mm in strategy 3. This variation in design will not affect the distance between each ridge, which stays the same, but rather the surface area of the non-textured material and, consequently, the size and number of pillars present in each sample. Since other parameters such as power and scanning speed remained constant, the depth and morphology of the samples should be identical. Parameters such as laser power and scanning speed are kept constant throughout the texturing process. In fact, the only parameter that differs between textures is the number of passes: 16 in the 1 mm and 0.8 mm strategies, and only 2 in the 0.25 mm texture. Table 10 represents all the conditions used in each one of the referred textures. After texturization, all samples are cleaned with isopropyl alcohol for 1 minute, using ultrasound technology, to remove possible debris or surface contamination.

Table 10 - Texturing conditions used in the texturing of the Ti6Al4V samples.

Pattern	Power (%)	Number of Passes	Scanning Speed [mm/s]	Frequency [Hz]
1mm	30	16	1500	50
0.8mm				
0.25mm		2		

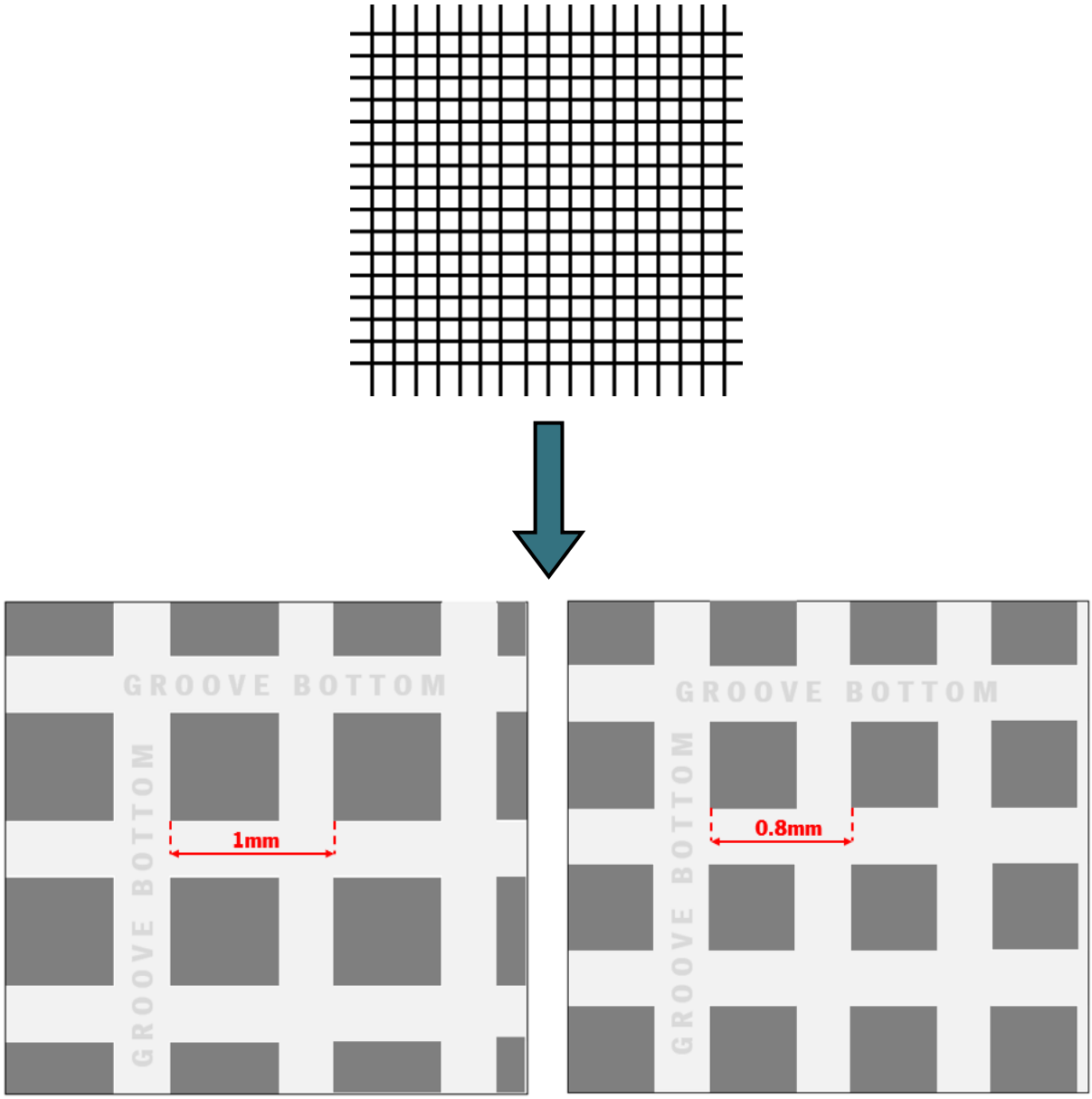

Figure 32 - Pattern used in the texturing of the Ti6Al4V samples. The number in the patterns represents the length of a ridge and the respective groove, as represented on the bottom schematic.

1.2.3) Coating of Bioactive Materials

1.2.3.1) Hydroxyapatite

The selected titanium samples were afterwards functionalized with hydroxyapatite (nanoXIM Hap400, from Fluidinova) by the spin-coating method, as represented in figure 18 of the previous chapter. Figure 33 depicts the SEM images (x1000, x5000) of the used Hap powder, while table 11 presents the chemical composition of said powder, according to supplier.

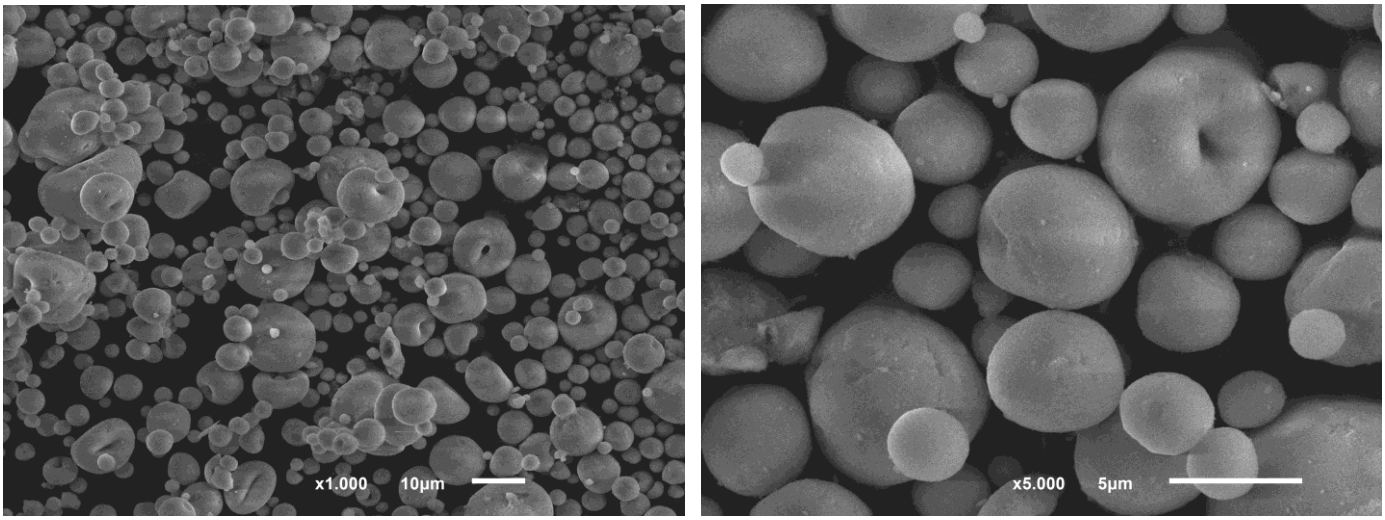

Figure 33 - SEM images (x1000, x5000) of the Hap powder.

Table 11 - Chemical composition of the Hap powder, according to supplier.

ELEMENTAL COMPOSITION	Ca	P	Co	Cu	Ni	Cr
Wt (%)	38.77	23.66	7.88	6.09	12.97	11.75

In an initial stage, the deposition of the Hap coating was processed through means of dip-coating. However, after analysis of the SEM images, it was concluded that the finalized coating was not homogeneous enough, as the deeper grooves of the textured samples would not often be correctly filled with the coating. In this sense, the spin-coating technique was adopted, and thus the samples were placed and properly fixed on a spin plate (MECAPOL P251). Afterwards, a bioactive suspension, composed of water and Hap, was slowly deposited, with the help of a pipette, on the textured face of the rotating samples (about 2 drops). Therefore, the centrifugal force applied on the sample allows the creation of a uniform hydroxyapatite film. Table 12 presents the spin-coating conditions used in the creation of the Hap layers.

Table 12 - Spin-Coating conditions used in the creation of the Hap bioactive layer

SPIN-COATING SPECIFICATIONS:	VALUES
Diameter of the Sample	8mm
Solvent	Water
Concentration of the Bioactive Suspension	0.133 g/mL
Volume Deposited	2 drops
Rotation Speed	300 rpm
Duration	1 minute

1.2.3.2) Sintering of the Hydroxyapatite Coating

After the coating is concluded, the functionalized samples were sintered using two different methods: laser sintering and conventional (furnace) sintering.

The laser sintering of the samples was performed using a CO2 laser (BD-50C, Bende, China), with a maximum power of 50 W and a wavelength of 10640 nm, represented in figure 34. The CO2 laser technical characteristics are presented in Table 13. This equipment is classified as a gas laser and, much like the previous equipment's used, the laser is connected to a computer by means of which it is possible to design the 2D draw needed on the laser processing, as well as control the sintering parameters through the software EZ-CAD. In this sense, a drawing composed of a succession of lines, distanced from each other by 0.01mm, was designed in Inkscape (v0.91) and applied in the sintering of all the samples. The respective drawing is presented in figure 35. The conditions used in the first sintering process, based on the literature, were considered inadequate (P30 W, S750 mm/s), since the Ca/P ratio in each sample turned out to be significantly lower than that found in the literature (1.67). Therefore, an optimization process was conducted, in which different parameters, such as power and scanning speed, were varied in order to evaluate the laser sintering performance under different conditions, and its consequences on.the Ca/P ratio and Hap properties. Table 14 represents the conditions tested.

Table 13 - CO2 laser specifications

LASER SPECIFICATIONS:	VALUES
Maximum Output Power [W]	50
Wavelength [nm]	10640
Laser Technology	CO_2
Spot Size (mm)	0.02
Cooling System	None

Table 14 - Parameters tested in the laser sintering of the Hap-coated samples.

Scanning Speed / Power	10 %	20 %	30 %
750 mm/s	P10S750	P20S750	P30S750
1000 mm/s	P10S1000	P20S1000	P30S1000

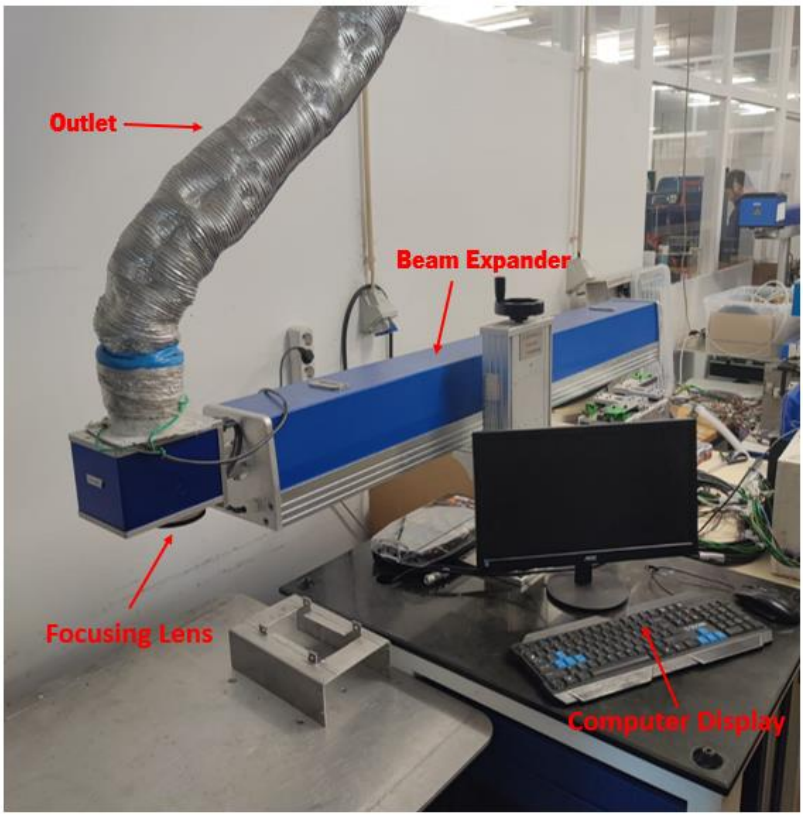

Figure 34 - CO2 Laser system setup used in the experimental work (CMEMS Laboratory of the Mechanical Engineering Department of University of Minho).

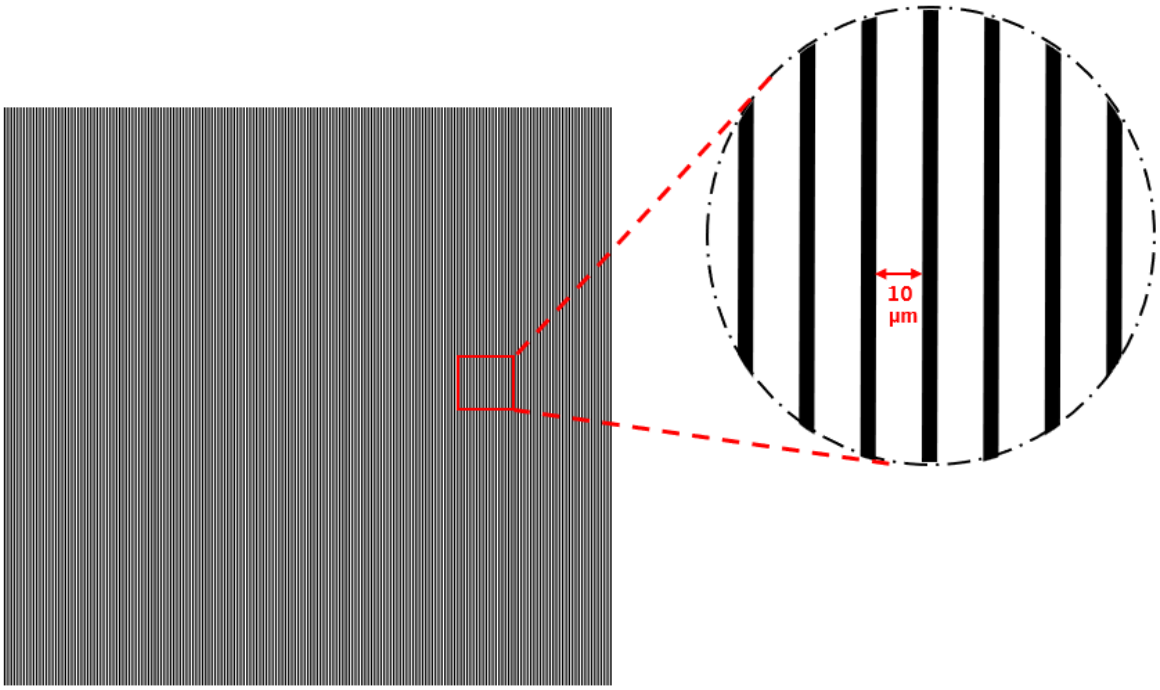

Figure 35 - Pattern used in the laser-sintering of the Hap-coated samples.

Conventional sintering was based on a more uniform and simple method, and initially tested using two types of furnaces: a vacuum furnace and a muffle furnace. Table 15 represents the three different strategies tested for the sintering of the titanium samples.

The vacuum furnace used was a tubular furnace (Termolab, Águeda, Portugal), represented in figure 36. These types of furnaces function in the absence of air, which prevents oxidation, heat loss from convection processes and removes possible contamination. Firstly, a turbomolecular pump removes the air inside the furnace, reaching levels of pressure close to $5 * 10^{-4}$ Pa. The thermal cycle is then established through an electronic system embedded in the furnace, and the temperature measured and controlled during the sintering process through various sensors present in the heating chamber.

On the other hand, the muffle furnace used (Termolab, Águeda, Portugal) is represented in figure 36. These furnaces function in the absence of vacuum, which causes oxidation, and higher temperatures are necessary to achieve full sintering. The thermal cycle is similar to that of the vacuum furnace: an electronic system sets the values, and the sensors analyse and regulate the temperature.

Table 15 - Conditions tested in the furnace sintering of the Hap-coated samples.

	Condition 1	Condition 2	Condition 3
Furnace	Vacuum	Vacuum	Muffle
Heating Rate	8°C / minute	8°C / minute	20°C / minute
Holding time	1 hour	1 hour	1 hour
Maximum Temperature	1175°C	950°C	950°C
Pressure	Vacuum ($5x10^{-4}$)	Vacuum ($5x10^{-4}$)	Atmospheric

Figure 36 - Furnaces used in the conventional sintering of the Hap-coated samples: vacuum furnace (left) and muffle furnace (right).

2) Materials Characterization

The produced samples are afterwards characterized through different techniques, presented in this subchapter, in order to evaluate the different conditions used and guarantee the success of the pre-established objectives of the present work. Therefore, these techniques comprise morphological, physical, chemical and mechanical material characterization.

2.1) Surface Characterization Techniques

2.1.1) Optical Microscopy

Optical Microscopy (OM) are pratical, versatile and inexpensive laboratory equipment that allow the fast visualization of small surface features that are not discerned by the human eye, using visible light and adequate magnification to expose the microscopic features of a surface. However, optical microscopes have several limitations, such as low resolution, poor depth of focus and short magnification range, and are, therefore, not suitable for more detailed studies.

As a first approach for samples imaging an optical microscope (OM), a Lampert SM03 Welding Microscope (Germany) was used (figure 37).

Figure 37 - Lampert SM03 Welding Microscope (Germany). (CMEMS Laboratory of the Mechanical Engineering Department of University of Minho).

2.1.2) SEM-EDS

In contrast to OM, scanning electron microscopy (SEM) uses an electron beam, instead of visible light, which allows higher magnification imaging and the ability to caption micrographs with extreme detail, resolution and depth of focus. In a SEM observation, a highly energetic electron beam is focused on the target surface. From the interaction of the electron beam with the target material different types of photons and electrons are released: characteristic X-rays, secondary electrons, backscattered electrons, and others. Each species is then detected through various sensors and analysed, revealing important information. In fact, characteristic X-rays are used for elemental analysis, while secondary electrons provide image rendering of the surface [176].

Therefore, an ultra-high-resolution field-emission Scanning Electron Microscope (FEG/SEM) with a built-in microanalysis X-ray system (EDS) (SEM – Nova NanoSEM 200, FEI, Netherlands) was used to analyse the morphology of the zirconia powder and different microstructures produced by texturing, as well as to evaluate the degree of sintering of the bioactive compounds on the surface of the produced samples. The elemental surface analysis was performed by Energy Dispersive X-ray Spectroscopy (EDS).

2.2) Wettability

The texturization process and the incorporation of bioactive materials on the surface of the samples have clear effects on the topography, chemical composition and consequent wettability of the material [107]. In fact, and as already mentioned in this work, surface energy is intimately related to wettability, since a higher surface energy means that the surface has a higher affinity to the molecules that compose the liquid than them among themselves [89].

Water contact angle (WCA) measurements are most popularly used to evaluate surface wettability and consequent surface energy. The contact angle (θ) is the angle formed between the liquid-vapor, solid-liquid interfaces and the surface of the sample (vertex), as depicted in figure 38 [178]. Young`s equation relates these three variables and provides the respective contact angle on a solid (smooth) surface (eq.X), as shown below:

$$\gamma_{sv} = \gamma_{sl} + \gamma_{lv}.\cos\theta_{YG}$$

Where γ_{sv} stands for the surface tension of the solid-vapor interface, γ_{sl} stands for the surface tension of the solid-liquid interface, γ_{lv} stands for the surface tension of the liquid-vapor interface and θ_{YG} the Young`s contact angle.

Depending on the WCA value obtained, the surface is considered:

i. Hydrophobic, if $90^{\circ} < \theta < 150^{\circ}$;
ii. Superhydrophobic, if $\theta \geq 150^{\circ}$;
iii. Hydrophilic, if $10^{\circ} < \theta < 90^{\circ}$;
iv. Superhydrophilic, if $\theta \leq 10^{\circ}$.

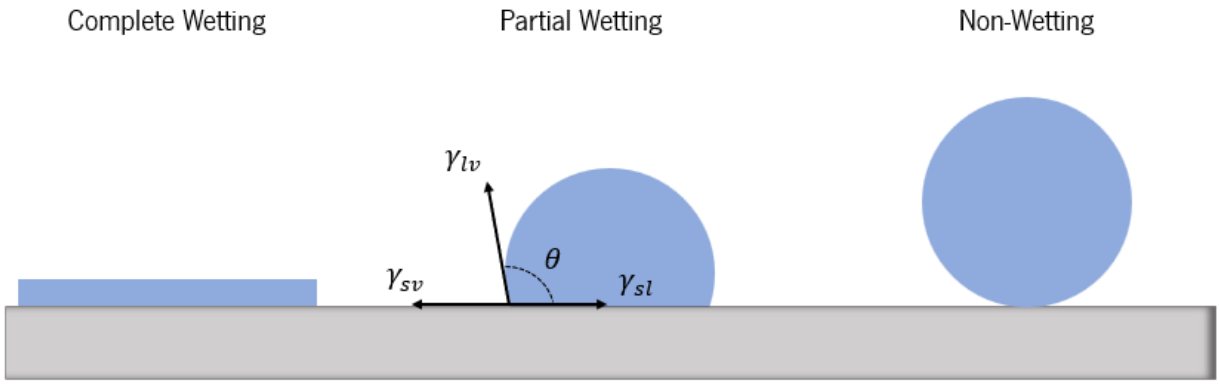

Figure 38 - Schematic illustrations of the different wetting states of a droplet deposited onto a smooth surface. (a) super-hydrophilic surface; (b) partial wetting of a hydrophilic surface; (c) super-hydrophobic surface.

There are different methods that can be used to analyse the water contact angles. However, in the present work, only the sessile drop method technique was used, due to its simplicity and ease of use. Therefore, these measurements are performed in an optical goniometer, where a single droplet of ionized water is placed on the testing surface by a micrometer syringe. A camera registers the contact and the consequent evolution of the contact angle of the liquid, and a software program later analysis the footage and obtains the correct angle.

2.2.1) Wettability on rough surfaces

As mentioned in the previous chapter, surface topography as a huge impact on the wettability of a surface. Therefore, and since Young´s model is only applied to smooth surfaces, the resulting contact angles on rougher surfaces are called apparent contact angles (ACA). In fact, different models were created to describe liquid behaviour in these types of surfaces, such as the Wenzel and Cassie-Baxter models (fig.39).

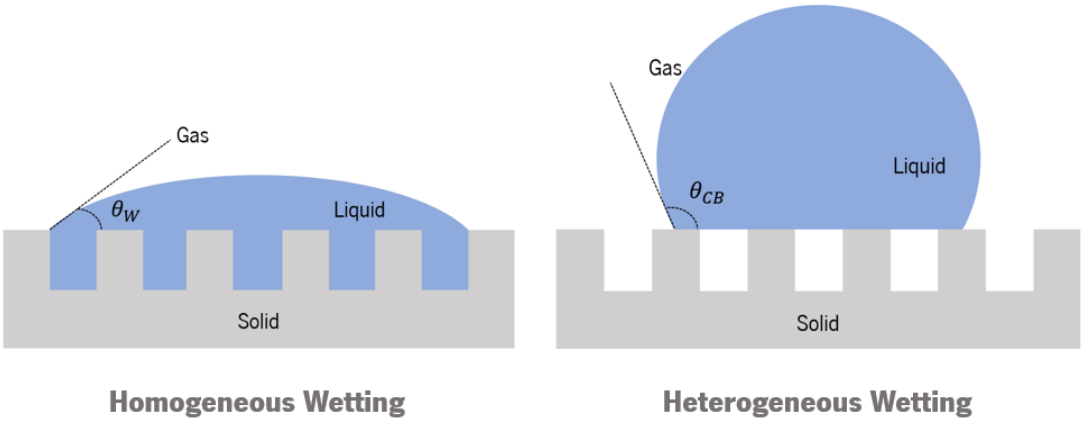

Figure 39 - Wenzel and Cassie-Baxter models for surface wettability of solid surfaces.

The Wenzel model recounts for a homogeneous wetting, in which roughness increases wettability. This model relates the real contact angle and the Young contact angle (θ_{YG}) through a roughness factor, named r. Therefore, the Wenzel equation is as follows:

$$\cos\theta_W = r\cos\theta_{YG}$$

Where θ_W represents the Wenzel´s contact angle. Consequently, this model states that, as the roughness of a certain surface increases, the hydrophobic surfaces become even more hydrophobic ($\theta_A > \theta_{YG}$) and hydrophilic surfaces become even more hydrophilic ($\theta_A < \theta_{YG}$) [179].

On the other hand, the Cassie-Baxter model recounts for a heterogeneous wetting, in which roughness decreases wettability. In this case, the contact angle is dependent on the area fraction of each phase (fi), and the relation between them is the Cassie-Baxter equation:

$$\cos\theta_{CB} = f_1\cos\theta_{YG^1} + f_2\cos\theta_{YG^2}$$

Where θ_{CB} describes the Cassie-Baxter´s contact angle, f_1 and f_2 the area fractions of each phase and θ_{YG^1} and θ_{YG^2} the Young´s contact angle of their respective phase. Therefore, this model describes a perfect equilibrium of the droplet on top of the asperities, which only tends to happen in superhydrophobic surfaces ($\theta \geq 150°$). Consequently, the two models tend to co-exist in most scenarios [179,181].

2.2.2) Contact Angle Measurements

Surface wettability of the created samples was evaluated and measured through the sessile drop method, using as testing media ultrapure ionized water (at 18.2 Ohm). Prior to any measurements, the selected samples were ultrasonically cleaned and dried. The apparent contact angles were calculated using a OCA 15 plus (Dataphysics, Germany) optical goniometer, depicted in figure 40. Droplets of 5 µL were deposited in the surface of the samples, and then analysed by means of video microscope and the software SCA 20 (Dataphysics, Germany). For the need of reproducibility of results, the WCA measurements were carried out at least 4 times for each condition tested, and at different locations.

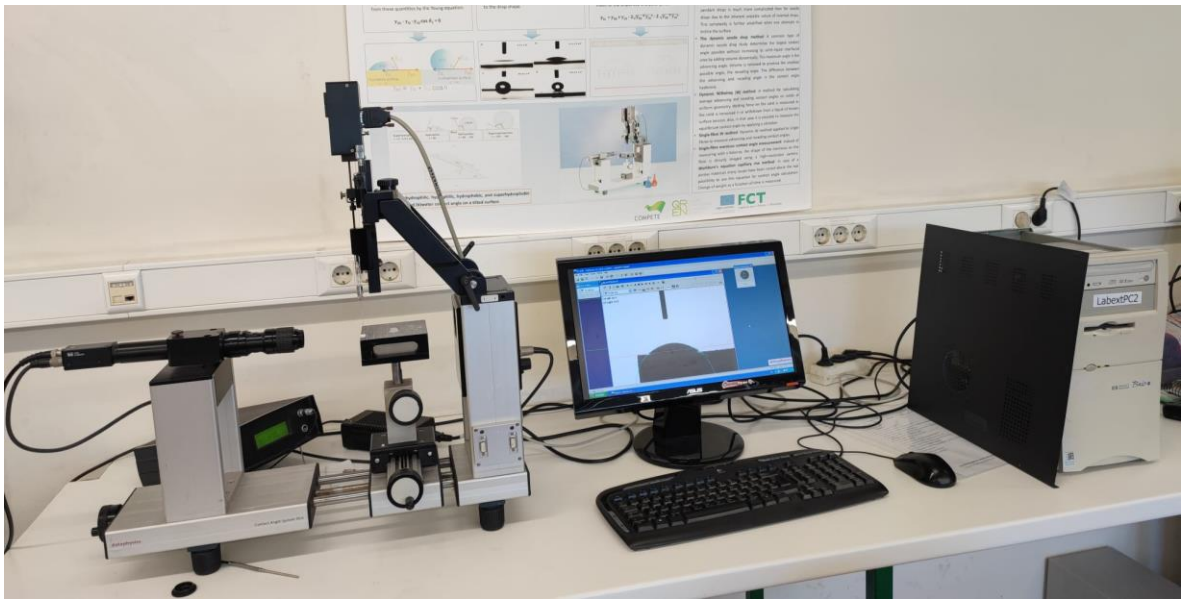

Figure 40 - Optical goniometer OCA 15 plus, Dataphysics, Germany. Available in the Textile Laboratory of the Textile Department of University of Minho.

2.3) Ultrasonic Adhesion Tests

Ultrasound cavitation is a phenomenon that involves the repetitive formation, growth and implosive collapse of bubbles in a liquid medium. This collapse produces a rush of the fluid to fill the void, forming a jet against the surface of the tested samples that causes a disruption of the interfacial boundary layers, possibly removing the coating. Therefore, this technique is typically used to test the adhesion efficiency between different materials and to evaluate the mechanical interlocking of different coatings. In this work, all samples were subjected to an ultrasonic cavitation test using an ultrasonic processor (UP200St, Hielscher, Germany), shown in figure 41. The samples were submitted to a power of 100W and a frequency of 40 Hz for 1 minute in a vessel containing isopropanol.

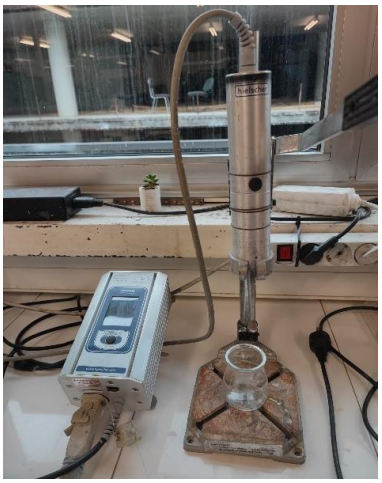

Figure 41 - Ultrasonic processor, UP200St, Hielscher, Germany (CMEMS Laboratory of the Mechanical Engineering Department of University of Minho).

2.4) Reciprocating Friction Test

Friction tests were employed in order to evaluate the friction and structural integrity of the produced samples when in an environment that mimics that of the natural human bone. Therefore, real bone (extracted from the femur of a young bovine), combined with a phosphate buffered saline (PBS) solution, was used as the base material during these tests. The bone was cut into circular pieces of about 25mm of diameter using a drill, polished until a flat surface was obtained and afterwards ultrasonically cleaned in isopropanol. The equipment used was a reciprocating pin-on-plate tribometer (Bruker-UMT-2, USA), as represented in figure 42. The performed friction tests assessed both the static and the dynamic coefficient of friction (COF).

Figure 42 - Tribometer Bruker-UMT-2, USA. Available on the Tribology Laboratory of the Mechanical Engineering Department of the University of Minho.

2.4.1) Experiment Conditions and Details

In the present work, the circular pieces of bone were mounted in an acrylic electrochemical cell, serving as the plate, while the produced samples were fixed to the pins. A PBS solution (detailed in table 16) was used as a lubricant fluid, since it is a simulated body fluid commonly used in biomedical research. The friction tests are depicted in detail in figure 43.

Table 16 - PBS composition according to the supplier.

Composition	NaCl	KCl	Na_2HPO_4	KH_2PO_4
Concentration (Mm)	137	2.7	10	1.8

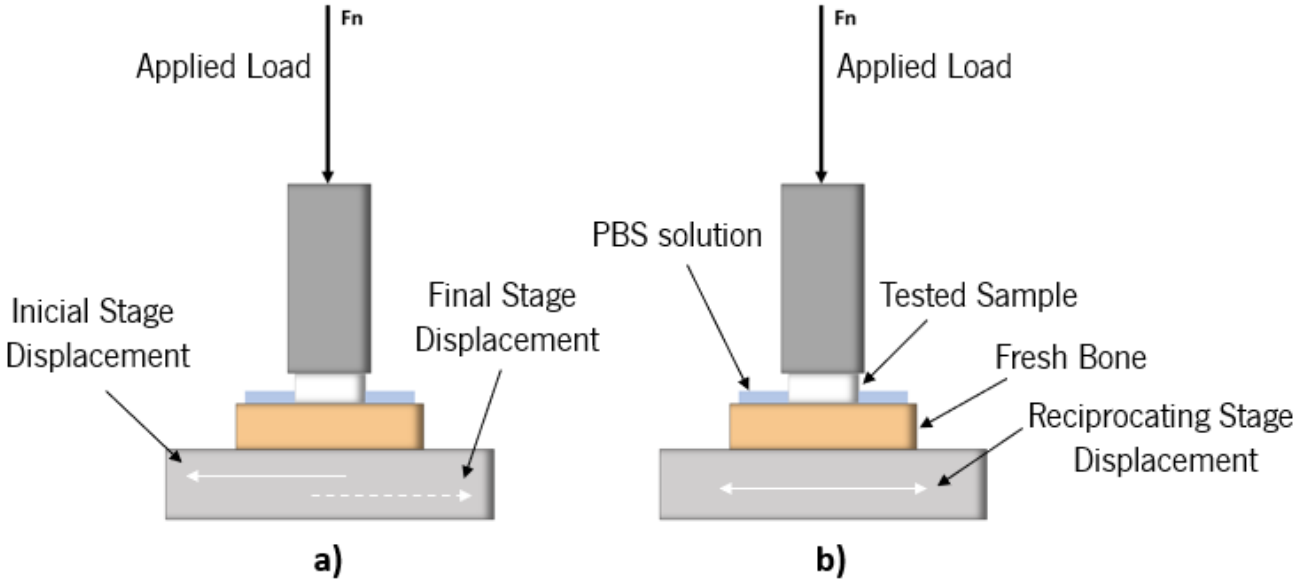

Figure 43 - Schematic representation of the friction test: a) initial static friction test; b) dynamic friction test.

As already mentioned, friction is an essential parameter when evaluating the primary fixation capacity of the implant and the structural integrity of the created coatings. In fact, the higher the coefficient of friction (COF) of a given material, the higher the force required to create sliding between it and the bone [57], as the mechanically interlock between both materials creates a stable interface. There are three coefficients of friction: the initial static COF, which should be as high as possible to guarantee the fixation of the implant to the bone; the dynamic COF, which represents the friction that occurs between bone and material during movement; and the final static COF, relative to the end of the movement, which should be lower than the initial COF, indicating possible adhesion of bone to the material [180]. The friction tests consisted of two stages as follows: i) determination of the initial static coefficient of friction by a single displacement in one direction; ii) measurement of the dynamic coefficient of friction during 10 seconds of reciprocating sliding.

All the tests were performed under the same conditions, and the respective parameters are represented in table 17. For the need of the reproducibility of the results, at least three samples of each condition were tested, and every bone plate used was enough for the testing of two samples.

Table 17 - Conditions used in the reciprocating friction tests.

Lubricant	Applied Load	Stroke Length	Oscillation Frequency	Duration
PBS	50N	5mm	1Hz	17 sec

2.5) Biological Tests (Cell Viability)

Biological tests were employed in order to evaluate the biological properties of the created surfaces regarding cell adhesion and proliferation. In fact, and as previously discussed, the creation of different types of microstructures and the addition of different types of coatings to bulk materials can enhance the biocompatibility of the surfaces, creating more favourable conditions for prosthesis osteointegration and improving the efficiency of said devices [106,152-154].

Therefore, in this work, cell viability tests were performed in some of the created conditions using Human HGF hTERT gingivae fibroblasts, obtained from the Applied Biological Materials Inc. (abm)® (T0026; Richmond, Canada) repository. After defrosting the cells, cell culture was initiated in a 75 cm2 flask (VWRTM, Radnor,Pennsylvania, USA) with culture medium composed of Dulbecco's Modified Eagle's Medium-DMEM (BiowhittakerTM, LonzaTM, Basel, Switzerland) supplemented with 1% penincillin-streptomycin (LonzaTM, Basel, Switzerland) and 10% fetal bovine serum (Biowest, Nuaillé, France). The cells were incubated in an adapted incubator (Memmert®, Schwabach, Germany) under controlled environmental conditions: 5% CO2, 98% humidity and a temperature of 37 °C. Since these were cell cultures, all manipulation was performed using aseptic manipulation technique in a laminar flow chamber (Biobase®, Jinan, China). The culture medium was changed after 1 day of initial culture and during the multiplication and growth phase in each culture flask every 2 days. When the cells reached an approximate confluence of 100%, enzymatic detachment of these cells from the growth surface was performed using Trypsin-EDTA (LonzaTM, Basel, Switzerland). The number of viable cells was counted in a Neubauer chamber (Laboroptik Ltd., Lancing, UK) using Trypan-Blue staining (AMRESCO®, Solon, Ohio, USA). The sample discs were distributed in 48-well culture plates (Corning Inc®, Corning, New York, USA) and were incubated for 1 hour with appropriate culture medium. Subsequently, the cells were

seeded onto the discs at a density of 1x104 cells/well with 500µl of culture medium. All experiments were conducted using a third pass, thus ensuring homogeneity of behavior between different experiments.

Cell viability of fibroblasts on each surface was assessed using a viability assay based on rezasurin reduction - Cell-TiterBlue® reagent (Promega®, Madison, USA), according to the manufacturer's protocol. The conversion rate of the non-fluorescent blue dye (possible only in mitochondria of viable cells) was determined as fluorescence intensity in arbitrary fluorescence units (AU) after 1, 3 and 7 days of culture. Fluorescence intensity was detected at excitation wavelengths 530/30nm and emission wavelengths 595/10nm using a multimode microplate reader (VICTOR NivoTM HH3500, PerkinElmer®, Pontyclun, UK).

These tests were performed in cooperation with the Faculty of Dental Medicine of the University of Lisbon, whose research team performed the previously mentioned assays. At the time of submission of this work, not all the created surfaces had yet been tested, and the results achieved comprised of only 7 days of cell culture. Therefore, the biological aspect of this work is mainly focused on the zirconia surfaces, as well as the produced MTA coatings.

CHAPTER IV

RESULTS AND DISCUSSION

This chapter presents the results obtained in this dissertation, and it can be divided into five different subchapters for each material tested. The first subchapter regards characterization of the created micropatterns: the microstructures are analysed and the influence of the laser parameters are discussed. Finally, the optimal conditions are chosen and advance to the coating stage, discussed in the second subchapter. In this chapter, the coatings created are morphologically and chemically described, the different sintering conditions and technologies are analysed and the optimal settings are identified. The third, fourth and fifth subchapters involve the testing of the selected samples: the third measures the wettability of the samples through contact angle measurements; the fourth describes the tribological performance of the created structures through friction tests; and the fifth subchapter analyses the biological performance of the obtained surfaces, regarding cell culture and antibacterial properties.

.

1) Zirconia

1.1) Textures Characterization and Parameter Influence

Two different strategies were implemented for the texturing of the zirconia samples (L16Pn (1) and D20PnSm (2)) and three specific laser parameters (power, speed and number of passes) were varied. In order to study the influence of this variation in the textures obtained, SEM images (120x and 500x) of the textures obtained according to tables 5 and 6 are represented in images 44 and 45. Since a great variety of parameter combinations were created and tested, especially for the D20PnSm strategy, not all the images obtained were placed in this work. Only some of the combinations created were selected, so that the differences produced by parameter variation were notable.

Firstly, it is important to highlight the high resolution and quality of the textures obtained, which were reproduced for the surface of the samples without any distortion and with adequate spacing. Additionally, through the analysis of the images with the magnification used, no micro-cracks were verified on the surface of the samples after texturization. This proves the importance of this process being performed on green, pre-sintered samples to preserve their mechanical properties, as previously mentioned [66].

1.1.1) Strategy 1 (L16Pn)

Regarding Strategy 1, figure 44 represents some of the textures produced, as well as the respective power (P) and number of passes (N) used. Each pattern contains two images (x50, x120). Additionally, table 18 presents the average groove depth of the textured samples, obtained through ImageJ software. Appendix A a) presents detailed micrographs of the samples.

Firstly, it is important to note the formation of two quite distinct types of structures: cavities (figure 44vii) and pillars (figure 44ix). Three levels of depth can be observed in the samples: ridges, the highest and practically non-textured area; ridge walls, an intermediate level area where the laser passed only once per pass; and grooves, the deepest area resulting from the intersection between the two laser orientations during a pass.

Regarding the influence of the texturization parameters in the produced samples, it can be observed that an increase in power (P35 to P45) for the same number of passes results in a greater depth of the machined sample (figure 44iv to 44vi, for example, registers an increase in depth from 54.506 ± 1.938 µm to 105.306 ± 0.508 µm). This happens since a larger amount of irradiated energy is implemented for the same area of material, so a larger volume of zirconia is removed (considering constant fluency). Additionally, and for all the number of passages tested (N=1,2,3) the variation from P35 to P40 led to a

more pronounced increase in groove depth than from P40 to P45. It is also observed that an increase in the number of passes (N=1 to N=3) for the same amount of power used results in greater sample depth (figure 44iii, 44vi and 44ix, for example, register a groove depth of 76.121 ± 2.066 µm, 105.306 ± 0.508 µm and 130.526 ± 1.330 µm, respectively). The explanation to this increment is similar to that of the power used: the power remains constant, but the amount of energy supplied grows for each pass. Finally, and as expected, a combination of both high power and high number of passes during the texturization process leads to the highest sample depth. In fact, and regarding the values presented in table 16, it is observed that the deepest texture is obtained when both parameters are maxed out (P45N=3).

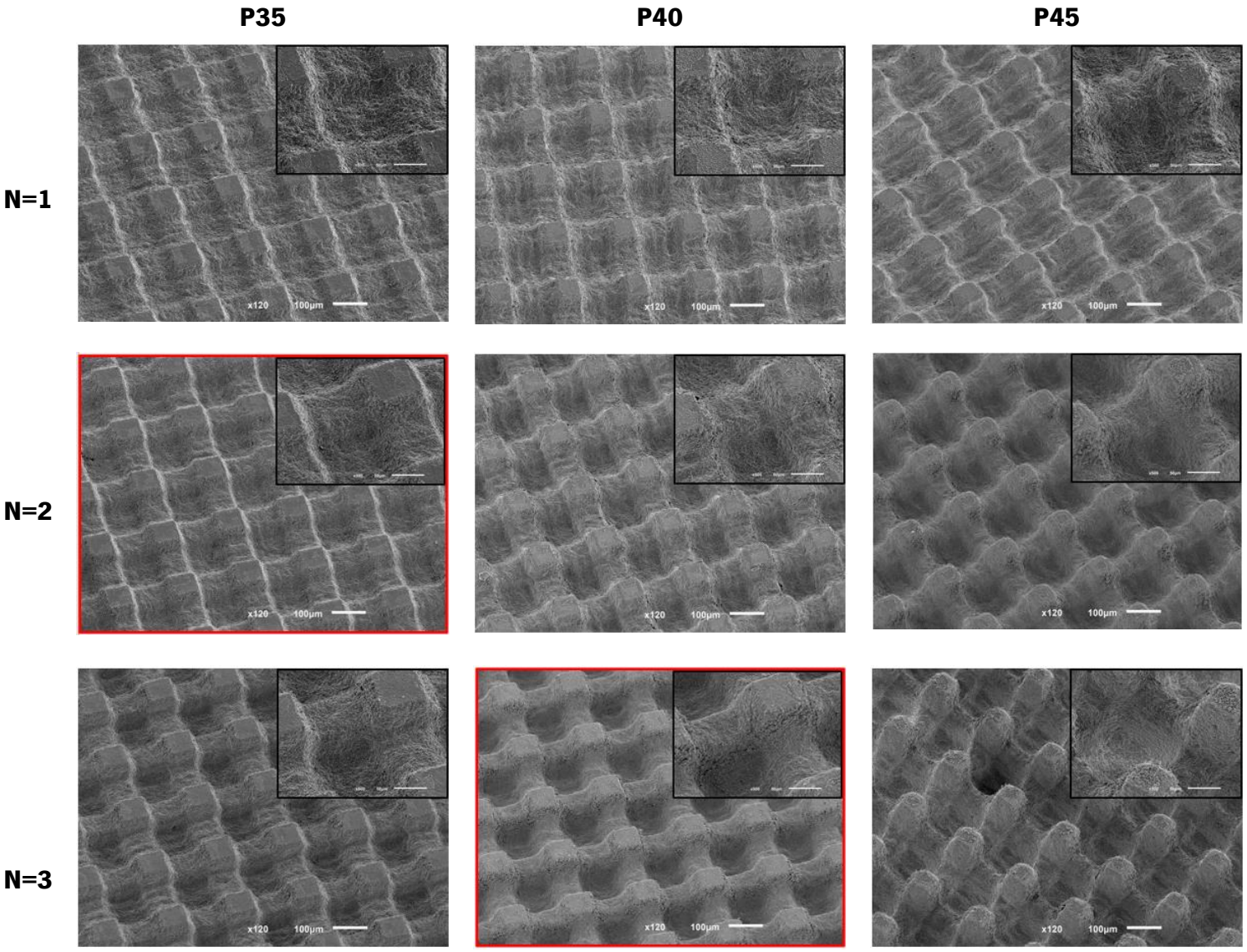

Figure 44 - SEM images (120x, 500x) of the obtained zirconia textured samples using the L16Pn texture.

i) L16P35 n=1; **ii)** L16P40 n=1; **iii)** L16P45 n=1; **iv)** L16P35 n=2; **v)** L16P40 n=2; **vi)** L16P45 n=2; **vii)** L16P35 n=3; **viii)** L16P40 n=3; **ix)** L16P45 n=3

Table 18 – Measured groove depth [µm] of all tested conditions.

Number of Passes / Power [W]	P35	P40	P45
N=1	34.799 ± 1.156	58.390 ± 1.674	76.121 ± 2.066
N=2	54.506 ± 1.938	91.011 ± 1.970	105.306 ± 0.508
N=3	77,892 ± 1.778	116.021 ± 0.987	130.526 ± 1.330

Thus, and as already mentioned, the creation of textures and certain geometric elements, such as cavities, pillars and grooves, seem to considerably improve cell adhesion, increasing the contact between them and inducing their proliferation in a controlled and homogeneous way, decreasing the probability of poor attachment or creation of scar tissue [106,124]. Additionally, it has also been shown that this type of structure considerably facilitates the incorporation of bioactive materials [139]. However, it is important that the depth of the textures created is adequate, as pillars that are too deep may prevent contact between the cells present in the ridges and grooves, while a depth of cavities that is too shallow may lead to reduced roughness of the sample and cause cells to behave similarly to what happens in flat, non-textured samples. Furthermore, the mechanical interlocking of the coating must be assured, and groove depth plays an important part in this process. Thus, the textures chosen for subsequent deposition of bioactive materials were **L16P35 (n=2)** and **L16P40 (n=3)**, marked in red. These textures present an appropriate level of depth according to the literature [128], and the choice of samples with distinct geometric structures (cavities and pillars) allows the study and comparison between the effectiveness of both, mainly regarding the capacity to control cell adhesion and proliferation.

1.1.2) Strategy 2 (D20PnVm)

Regarding Strategy 2, figure 45 represents some of the textures produced, as well as the respective power (P), scanning speed (S) and number of passes (N) used. Each pattern contains two images (x120, x500). Additionally, table 19 presents the average groove depth of the textured samples. Appendix A b) presents detailed micrographs of the samples.

Comparing the D20PnSm pattern to the previous strategy, the differences are obvious: while in the L16Pn texture well defined structures are created, these samples present only a slight increase in surface roughness. In fact, surface morphology is defined randomly.

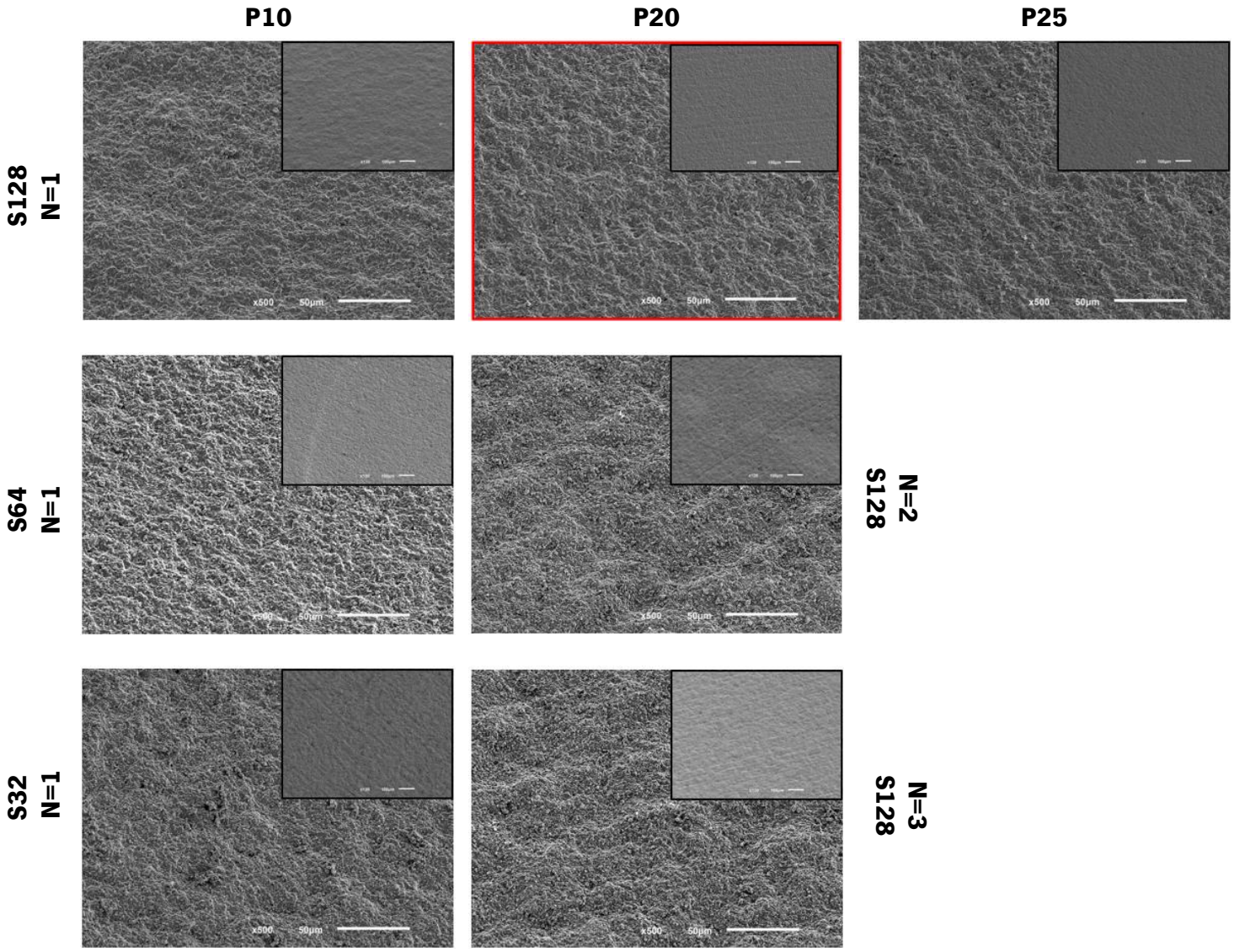

Figure 45 - SEM images (120x, 500x) of the obtained zirconia textured samples using the D20PnSm texture.

i) D20P10S128 n=1; **ii)** D20P20S128 n=1; **iii)** D20P25S128 n=1; **iv)** D20P10S64 n=1; **v)** D20P20S128 n=2; **vi)** D20P10S32 n=1; **vii)** D20P20S128 n=3

An analysis of image 45 shows that the obtained textures are very similar in all tested conditions, and that the obtained roughness is reduced when compared to the previous texture.

Regarding the influence of the varied parameters, it is verified that increasing laser power (P10 to P25), while keeping constant scanning speed and the number of passes (images 45i) to 45iii)), does not have any kind of influence on the texture obtained, since the roughness presented by the samples is practically identical and very reduced. On the other hand, an increase in the number of passes (N=1 to N=3), with constant power and speed (figure 45ii), 45v) and 45vii)), leads to the occurrence of more visible small waves (ripple effect), which are the result of the wobble present during laser texturing. These structures, however, do not seem to bring great advantages from a mechanical point of view. Finally, the decrease of the texturization speed (S=128 to S=32), with constant power and number of passes (figure 45i), 45iv) and 45vi)), has also no influence on the texture obtained, and the roughness is similar in all samples.

Thus, this strategy serves mainly to increase the roughness of the material randomly and without much control and depth, which leads to the creation of a microtexture (unlike the previous strategy, that created a macrotexture). Thus, the parameter chosen for subsequent deposition of the MTA coating was the **D20P20S128 (n=1)**, marked in red. The reason behind said decision fell mainly on the fact that this combination of parameters signifies a relatively short texturization time, all while still presenting a desirable level of roughness, which contributes to the effectiveness and speed of the entire process.

1.2) MTA Coating Characterization

Three different textures, two “macros” and one “micro”, identified in the previous chapter, were tested to evaluate the most adequate pattern to retain an MTA coating. These three textures are presented below, in image 46. After obtaining said textures, the coating was created and applied to the samples by means of cold pressing, as discussed in Chapter 3. Afterwards, each coated sample was put through ultrasonic cavitation, in order to evaluate the adherence of the coating created. Therefore, they were tested one by one, using isopropanol, using 100W of power for 2 minutes.

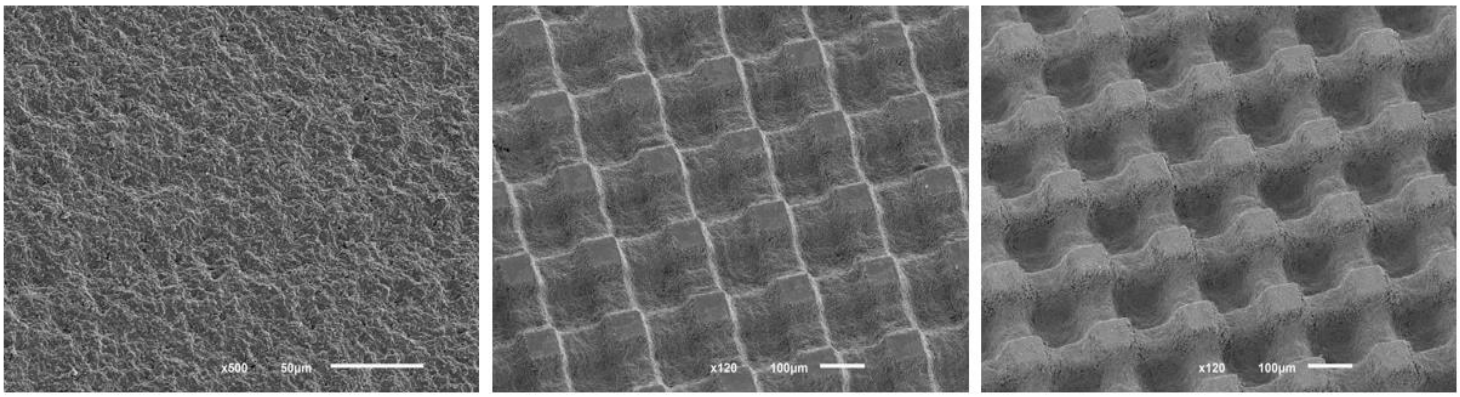

Figure 46 - Ideal textures selected: D20P20S128N=1 (left); L16P35N=2 (middle); L16P40N=3 (right).

In an initial phase, the MTA coating was deposited using only a spatula, without the application of any sort of pressure. However, and even though the coating appeared to adhere to the surface, most of the samples produced failed the ultrasound cavitation tests, as the entirety or a big portion of the MTA powder was removed. Therefore, the method of production was altered and optimized, as the device depicted in figure 29 was developed, and cold pressing was applied in order to improve coating adherence. The top view and cross-sectional SEM images of the resulting samples are presented in figure 47, and the thickness of the coatings were obtained through ImageJ software.

Firstly, it is important to note that the microtexture previously selected (D20P20S128N=1) was not tested in these conditions and is therefore excluded from any posterior analysis. This is due to the poor mechanical stability provided by this texture in an initial phase of MTA deposition (spatula method), in which the coating consistently disintegrated during surface polishing. Therefore, only the two macrotextures were considered.

In general, the SEM images show that MTA was successfully impregnated in the zirconia samples without compromising the substrate. In fact, no cracks are visible on the bulk material, which seems to indicate that the pressure applied to the samples did not affect the mechanical stability of the texture. However, the coating itself presents some cracks that extend from the base to the surface, as observed in figure 47iii. Since MTA is a form of cement these fractures are considered a normal occurrence, caused by the shrinkage of this material when hardening and drying. Additionally, the MTA layer in both textures presents some material porosity, especially visible in the L16P35N=2 texture (figure 48i to 48iv). This is due to either an excess of water in the coating mixture, which increases the water/cement ratio and decreases compaction, or due to the excessive duration of the moist curing [182]. Lastly, the layer of MTA is exceptionally thick in both samples (with a length of almost five and two times the depth of the pattern, respectively), which may be beneficial for the retention of bioactive material during insertion.

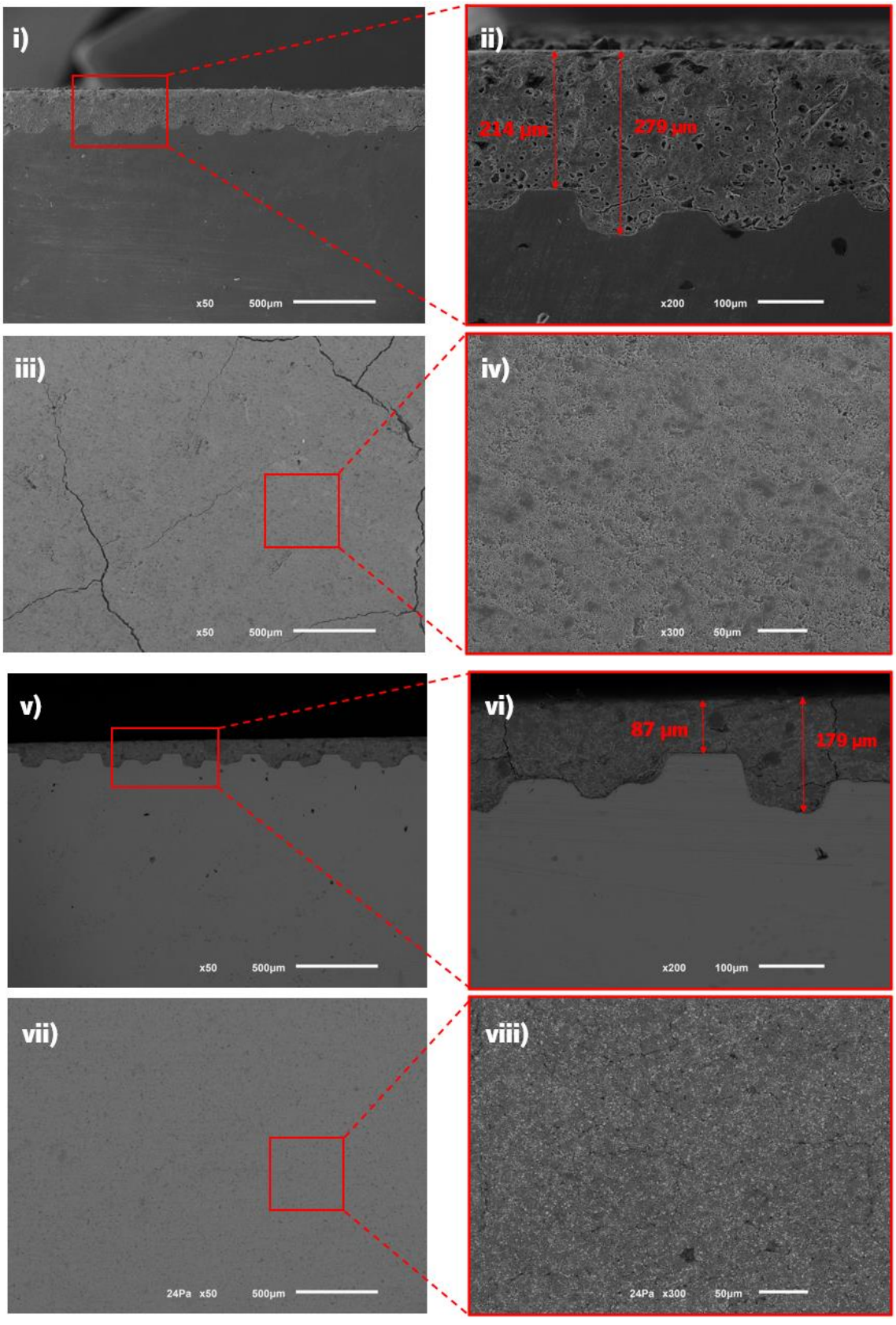

Figure 47 - Top-view and side profile SEM images (50x, 200x, 300x) of the MTA coated samples: L16P35N=2 (i to iv); L16P40N=3 (v to viii).

Therefore, it can be concluded that both tested conditions are adequate, providing mechanical interlocking and allowing the creation of a stable and compact MTA coating. In fact, the difference in surface depth does not seem to affect the mechanical standpoint of the coating, and the thickness of the bioactive layer, although relatively bigger in the L16P35N=2 texture, seems to be related not to the depth or morphology of the produced texture, but to the amount of MTA cement used when creating said layer. Therefore, and since both conditions can be used, the optimal condition chosen was **L16P40N=3**, since literature suggests that a higher surface roughness leads to a better mechanical interlocking, providing stabler anchoring points and efficiently compacting the bioactive material [104].

1.3) Wettability

In order to investigate the influence of the different combinations of micropatterns produced by LST and the incorporation of an MTA coating on the zirconia surface wettability, contact angle measurements were performed. Ultrapure water (at 18,2 Ohm), with a volume of 5 µL and a dosing rate of 2,5 µL/s, was used as testing media. This solution was dispensed from a micrometric syringe, brought in contact with the sample surface and allowed to stabilize before the reading was taken. Figure 48 shows the contact angles obtained for each tested condition, as well as the profile image of one of the measurements performed for each condition.

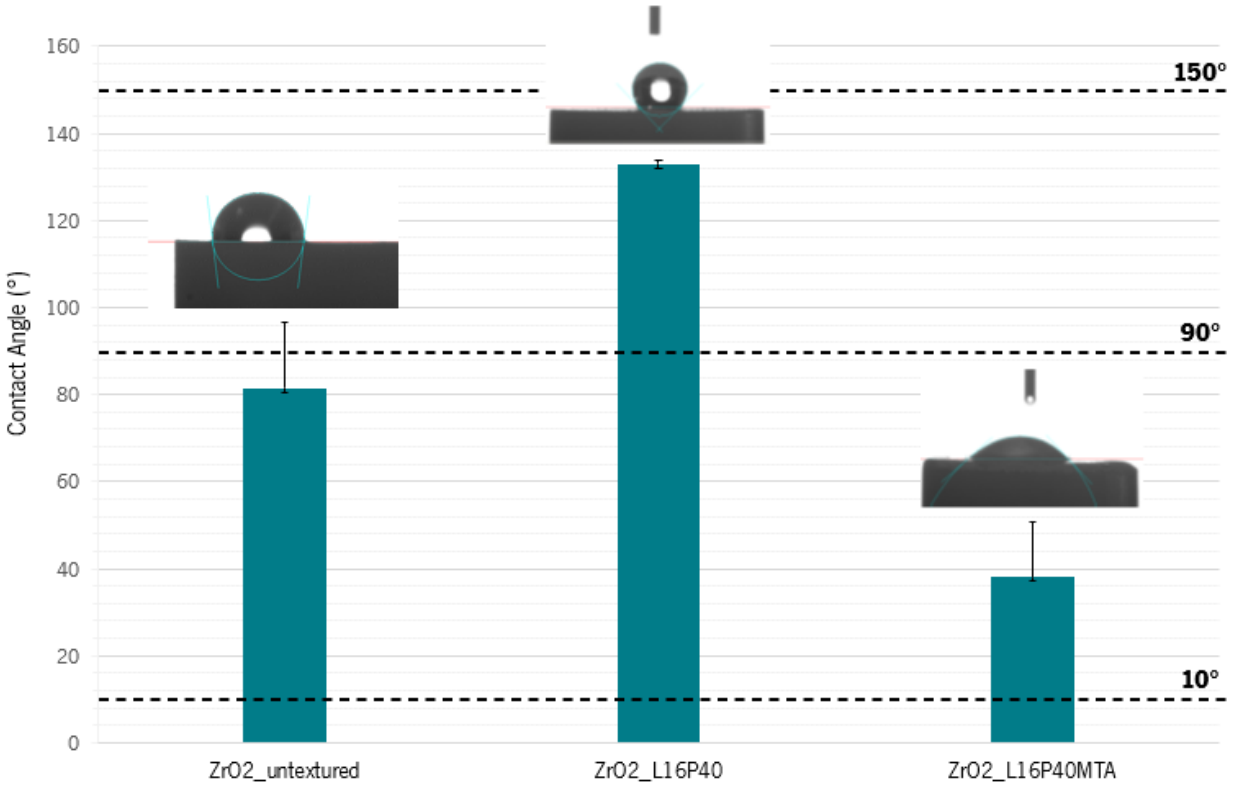

Figure 48 - Apparent contact angles obtained by sessile drop measurements from all the tested conditions.

By analysing the results, it seems clear that surface texturization led to an increase in the WCA of the samples, and therefore induced hydrophobicity. In fact, the polished non-textured surfaces presented an average contact angle of 81°, while the textured L16P40N=3 samples averaged 133°, which surpasses the 90° margin of hydrophilic behaviour, represented in the previous figure. This discrepancy might be explained by the achievement of different equilibrium states, such as the Wenzel and Cassie-Baxter models. In fact, it is hypothesized that the created features, such as well-defined pillars, play an important role in the interaction between the surface and the liquid, and lead to air entrapment beneath the drop and the occurrence of pinning effects, as expressed in the Cassie-Baxter model. Therefore, the water never fully reaches the bottom of the grooves, remaining in an intermediate state that results in the increase of the contact angle.

The incorporation of an active MTA coating led to a decrease of the surface contact angle and to a hydrophilic behaviour. In fact, the average angle obtained (38°) was lower than that of the polished untextured samples. This is due not only to the smooth surface obtained after the creation of the coating, but also due to the composition of the surface material. In fact, MTA Angelus is mainly composed of various silicate and calcium particles, which hydrate in the presence of water, creating a hardened paste. However, after setting, the created cement exhibits a certain porosity, that is heavily dependent on the curing time and water/cement (W/C) ratio. In fact, and according to Pakravan and co-workers [183], for most cements, the longer the curing time and the higher the W/C ratio, the lower the pore size distribution and the surface free energy which, consequently, decreases the wettability of said surface. On the other hand, the sintering of the zirconia samples creates a compact and hardened material, eliminating the open spaces between particles and greatly reducing porosity and surface energy. Therefore, it can be concluded that the MTA Angelus coatings were created using an appropriate setting time and W/C ratio, which conferred them very hydrophilic properties.

1.4) Reciprocating Friction Tests

In order to evaluate the tribological performance of the created samples, as well as the structural integrity of the produced micropatterns in an environment mimicking the insertion of a knee prosthesis, reciprocating friction tests were employed. The tests were performed according to the conditions reported in Chapter 3, and the COF results for each tested condition are present in figure 49.

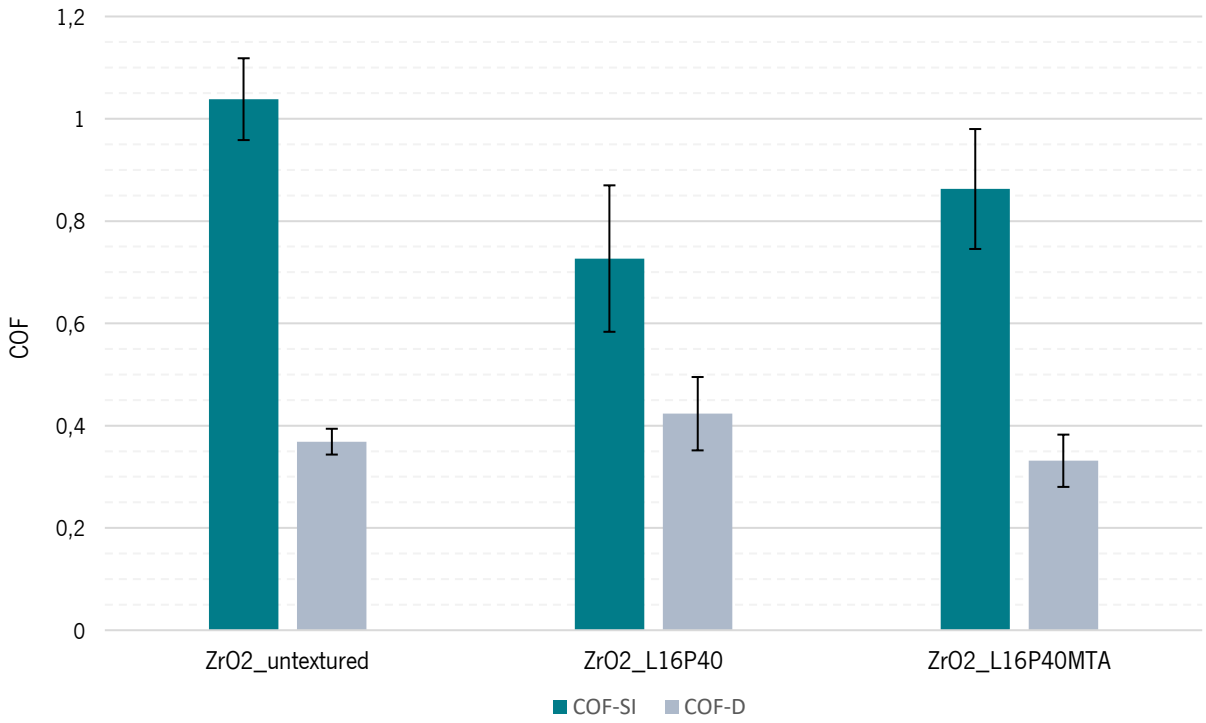

Figure 49 - Average coefficient of friction (COF) obtained for all tested conditions. COF-SI and COF-D denotes the static and dynamic coefficient of friction, respectively.

Firstly, it is important to point out, as observed in figure 49, that the static COF was higher than the dynamic COF for all tested conditions. These results were expected, as it seems to indicate that the bone enters a mechanism of adhesion and compaction: the normal load exerted by the sample during sliding causes bone debris to amass between the small asperities of the sample surface, which leads to the compaction of said material (figure 50). Therefore, the contact interface slowly transitions from bone-sample to bone-bone, which causes a decrease in the COF, as the required friction force to maintain the relative motion is lower compared to the one that is required to initiate relative motion. However, this conclusion must be validated by analysis of the SEM images of the sample surfaces, to evaluate the degree of bone adhesion.

The obtained results also show that the untextured samples present a higher static COF than the textured and MTA-coated samples. This was not expected, since various articles in literature state that an increase in roughness of a given surface leads to a higher surface friction and respective tribological performance [125,128]. One possible explanation for the decrease in static COF after laser texturing may be related to the normal load that was used, which may be too small to, in the initial movement, cause the samples to deform the bone surface, which in turn does not cause bone debris. It is important to

point out that the static COF is dependant not only on the loading force but also on the apparent contact area, as demonstrated by Katano et al. [184]. Therefore, and since the smooth zirconia surfaces have a much bigger apparent contact area than the L16P40N=3 textured surfaces, the static COF of said samples will also be higher. However, the sliding movement during the rest of the friction tests eventually deforms the bone and causes its entrapment in the asperities of the textured samples, which is indicated by the higher dynamic COF of these samples, when compared to the untextured surfaces. This theory must be supported by the analysis of the SEM images of the zirconia samples surfaces, mainly regarding the retention of bone material.

Lastly, the static COF increases after the coating of the samples with MTA. This is due to the higher chemical affinity of the bioactive material since the chemical structure of the coating is similar to that of the bone. Thus, bone material is more likely to adhere to the surface of the coated sample, which leads to an increase in required friction force and, consequently, a higher static COF [124,128]. Thus, it can be concluded that the MTA coating has a huge role in defining the tribological performance of the zirconia samples.

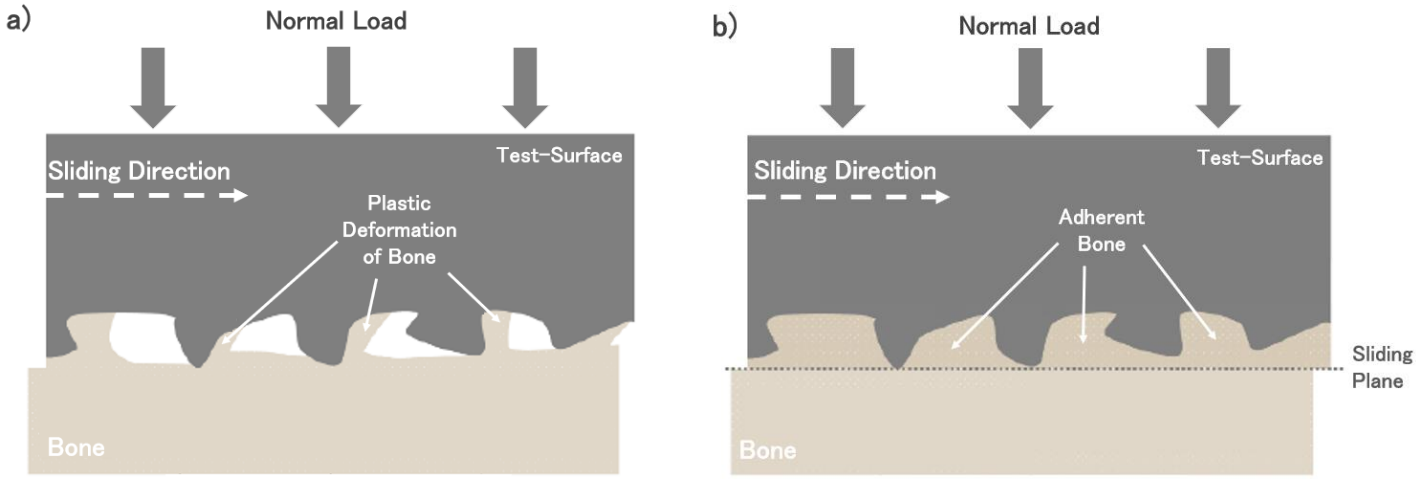

Figure 50 - Illustration of the mechanism of adhesion and compaction of bone against a test-surface. a) bone debris accumulates between asperities during sliding. b) gliding of the sample along the sliding plane and compaction of the adhered bone underneath.

In order to verify the above-mentioned assumptions, the morphology of both the zirconia and the bone worn samples was observed by SEM. Figure 51 shows the SEM micrographs (x150; x40) of the bone and zirconia surfaces after the friction tests. EDS analysis was also performed in said samples, as the different zones analysed are also identified in figure 51 (z1, z2 and z3). Appendix A c) presents detailed micrographs of the samples.

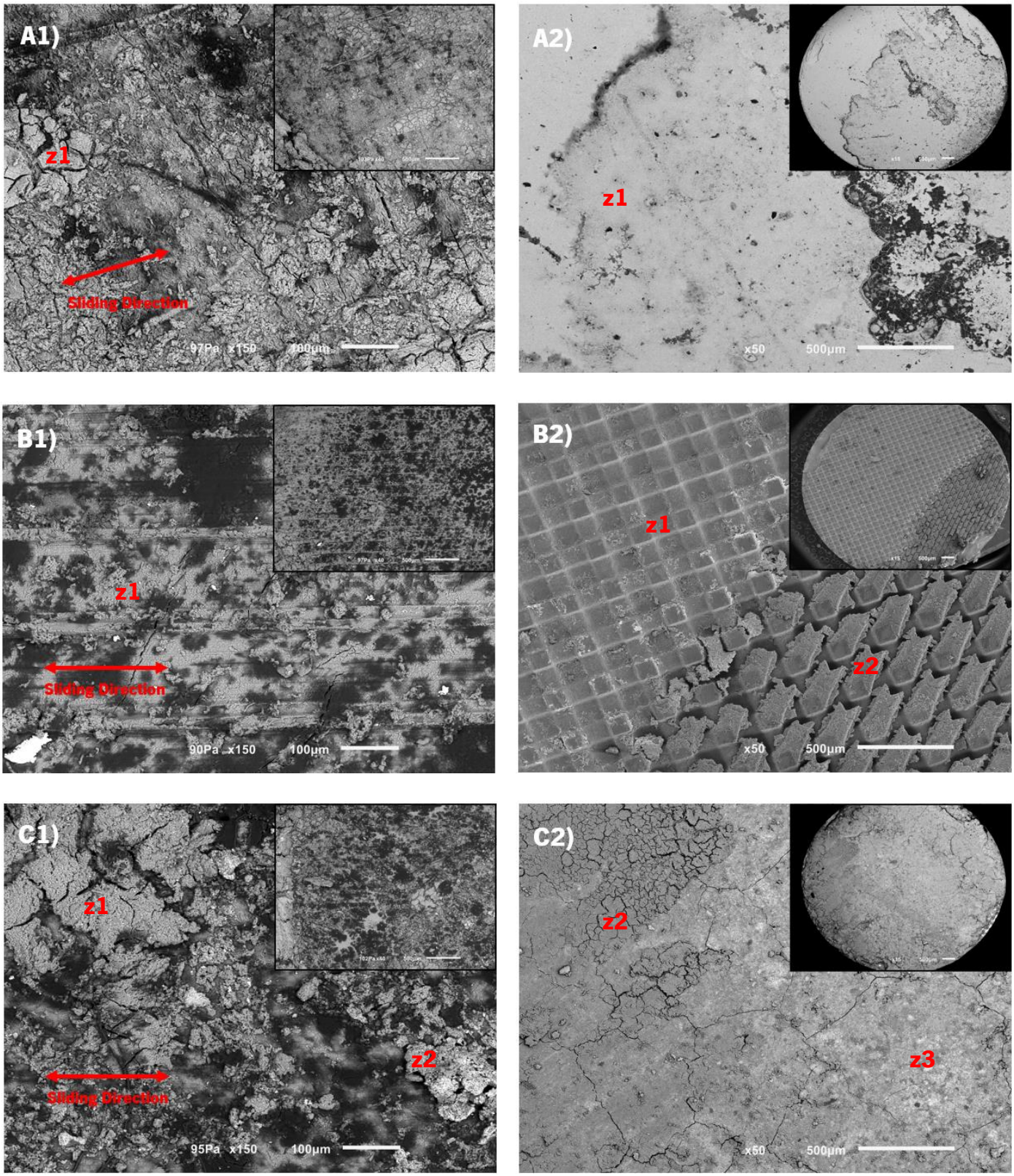

Figure 51 - Top-view SEM micrographs (x40, x50, x100, x150) of the bone (left) and zirconia (right) samples used during friction tests. A1&2) Untextured sample; B1&2) L16P40N=3 textured sample; C1&2) MTA-coated sample.

Bone samples: z1 – Bone; z2 – MTA. **ZrO2 samples:** z1 – ZrO2; z2 – Bone; z3 – MTA.

Analysing the images obtained by SEM technology, it seems clear the presence of adhesive mechanism on the zirconia samples (bone material adhered to the samples surface) and abrasion mechanisms on the bone surfaces (grooves aligned with the sliding direction). The adhesion of bone can clearly be seen in the micrographs of the samples, as well as in the EDS analysis performed in all studied samples.

The main elements found in the EDS studies of the zirconia samples were Zr (Zirconium), Y (Yttrium), Ca (Calcium) and P (Phosphorus). The Zr and Y elements found belong to the bulk zirconia material, while the Ca and P come from the bone. Bone transfer (z2) can be observed in every condition, except for the untextured zirconia surfaces, and the textured samples contain the highest transfer rate. Regarding these surfaces, the abrased particles seem to be located in the lower regions of the patterns, such as grooves, pits and the intermediate-level intersections, and do not cover the entirety of the texture. Therefore, the presence of specific microstructures, such as ridges and grooves, establishes a mechanical connection between the bone substrate and the zirconia surface. Additionally, it can be observed that the mechanical integrity of said structures is not compromised by the friction process.

Regarding the bone surfaces, figure 51 shows the difference between the various conditions tested. It can clearly be concluded that, out of all the tested conditions, the textured samples are the only ones that produced pronounced grooves on the substrate. These grooves are well-defined and aligned with the sliding direction of the zirconia samples, with a diameter of 16,3±1,778 μm. In contrast, the untextured samples do not produce any major marks, which means that bone deformation does not occur in these conditions. Therefore, the theory previously formulated is valid: the low normal load applied to the textured samples is not enough to penetrate and remove bone matter, which explains the low static COF. However, as the friction test progresses, the textured samples eventually deform the substrate, producing bone debris and entrapping it in surface asperities. Finally, and regarding the MTA-coated disks, the EDS analysis of the bone surface reveals that, apart from the elements previously mentioned, residues of silicon and aluminium were found, which are some of the main constituents of mineral trioxide aggregate powder (z2). However, there are no signs of grooves produced during testing, which was expected, since the surface of the coating was relatively smooth. Therefore, it can be concluded that the main agent that dictates the adhesion of bone to the sample and regulates the friction performance is the chemistry of the MTA coating and its affinity with bone.

1.5) Biological Tests

Cell viability tests were performed in order to evaluate the biological properties of the created surfaces regarding cell adhesion and proliferation. Regarding the zirconia bulk material, all created conditions were tested, as well as the titanium smooth samples, for comparison purposes. The tests were performed in accordance with the conditions described in chapter 3, and the obtained results are presented in figure 52.

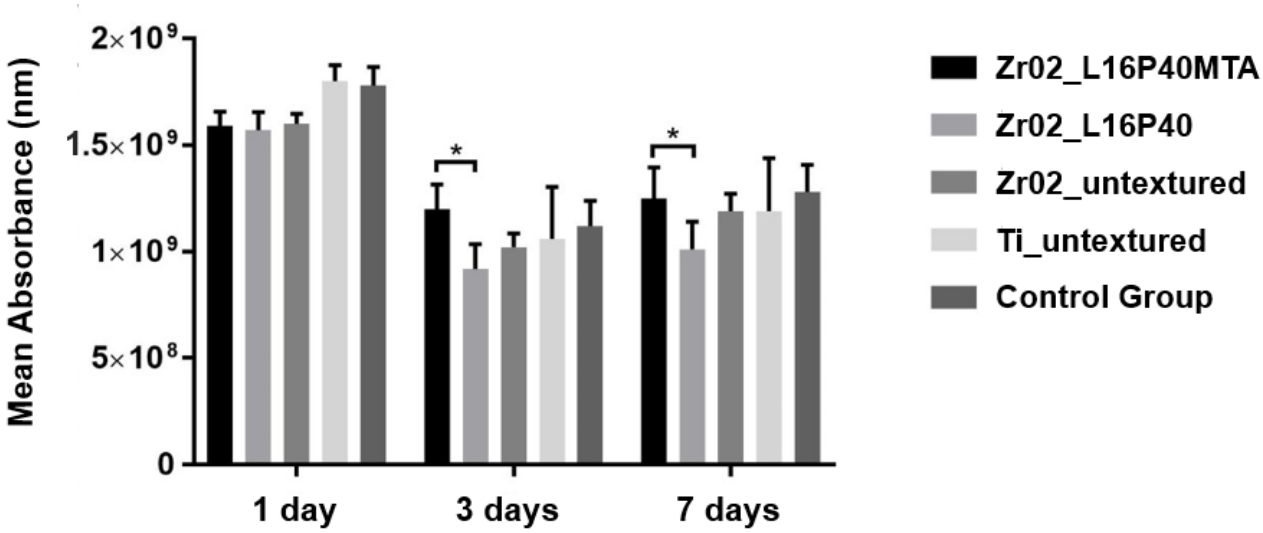

Figure 52 - Cell viability test results for all tested conditions.

Firstly, it is important to point out that after the first day of cell culture, all the zirconia-based surfaces (smooth, textured and MTA-coated) presented no significant differences in cell viability, and the smooth titanium samples registered the highest number of cells in the culture medium. However, by the third day of testing, an abrupt unexpected decrease in the number of cells can be observed in every condition, which is possibly the result of sample contamination. At this point, the MTA-coated samples presented the highest values of cell viability, while the L16P40N=3 surfaces can be considered the least biocompatible. Finally, by analysing the last day of cell culture, it can be concluded that this trend was maintained: the MTA samples present slightly higher numbers of fibroblasts when compared to the two smooth surfaces, and almost identical numbers to the control group. However, the textured zirconia samples obtained the lowest percentage of alive cells out of all conditions (20% lower than the MTA samples culture and 15% lower than the untextured samples culture). There is no significant difference between the two used materials in terms of biocompatibility after 7 days (zirconia and titanium).

2) Titanium

2.1) Micro-Textures Characterization

Three different strategies were implemented for the texturing of the titanium samples (1 mm, 0.8 mm and 0.25 mm) and only one specific laser parameter was varied (number of passes). In order to study the practical effects of the different patterns in the creation of micro-textures, SEM images (500x and 100x) of the samples obtained according to table 9 are represented in figure 53. As mentioned in the previous chapter for the zirconia samples, the obtained textured samples present high resolution and quality, without any distortion and adequate spacing.

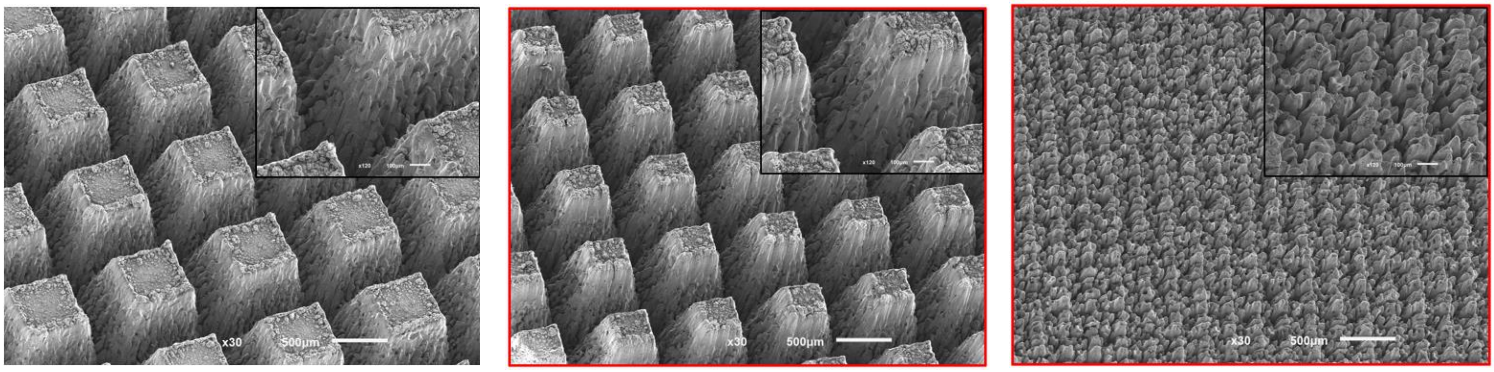

Figure 53 - Top-view SEM images (100x, 500x) of the textured titanium samples: 1mm (left); 0.8mm (middle); 0.25mm (right).

As observed, cross-hatched patterns were successfully produced through laser texturing. Much like what was obtained in the zirconia samples, the used parameters led to the development of two types of textures: macrotextures, with topographical elements visible and well defined (1 mm and 0.8 mm), and a microtexture, with diminished surface roughness and randomly produced topographical elements (0.25mm).

Regarding the macrotextures, figure 54 and table 20 establish a comparison between the 1mm and 0.8mm designs, regarding surface morphology and topography. Since the same parameters are used in both strategies their influence cannot be studied in this case. These patterns exhibited hydrodynamic structures such as resolidified droplets of material and raised sidewalls on the borders of non-textured areas, especially in the 1 mm design. These details were expected, since the texturization is based on ablation processes. Therefore, material that is situated in the borders of the spot area melts by thermal build-up and is pushed to the borders, creating raised sidewalls (figure 54iv) [185]. Cauli-flower-like structures are also visible in both textures, which appear to be titanium oxides originated during the laser

texturing process (figure 54ii). As also expected, the distance between each pillar in the 1 mm and 0.8 mm is similar since the width of the design pattern lines is the same (Table 20). Additionally, the depth of the samples is also identical, since all texturing parameters (such as power, number of passes and scanning speed) were maintained constant. However, the non-textured area of each design is considerably different: the 1mm design presents larger flat squares than the 0.8mm pattern, and consequently, almost three times more non-textured volume of material.

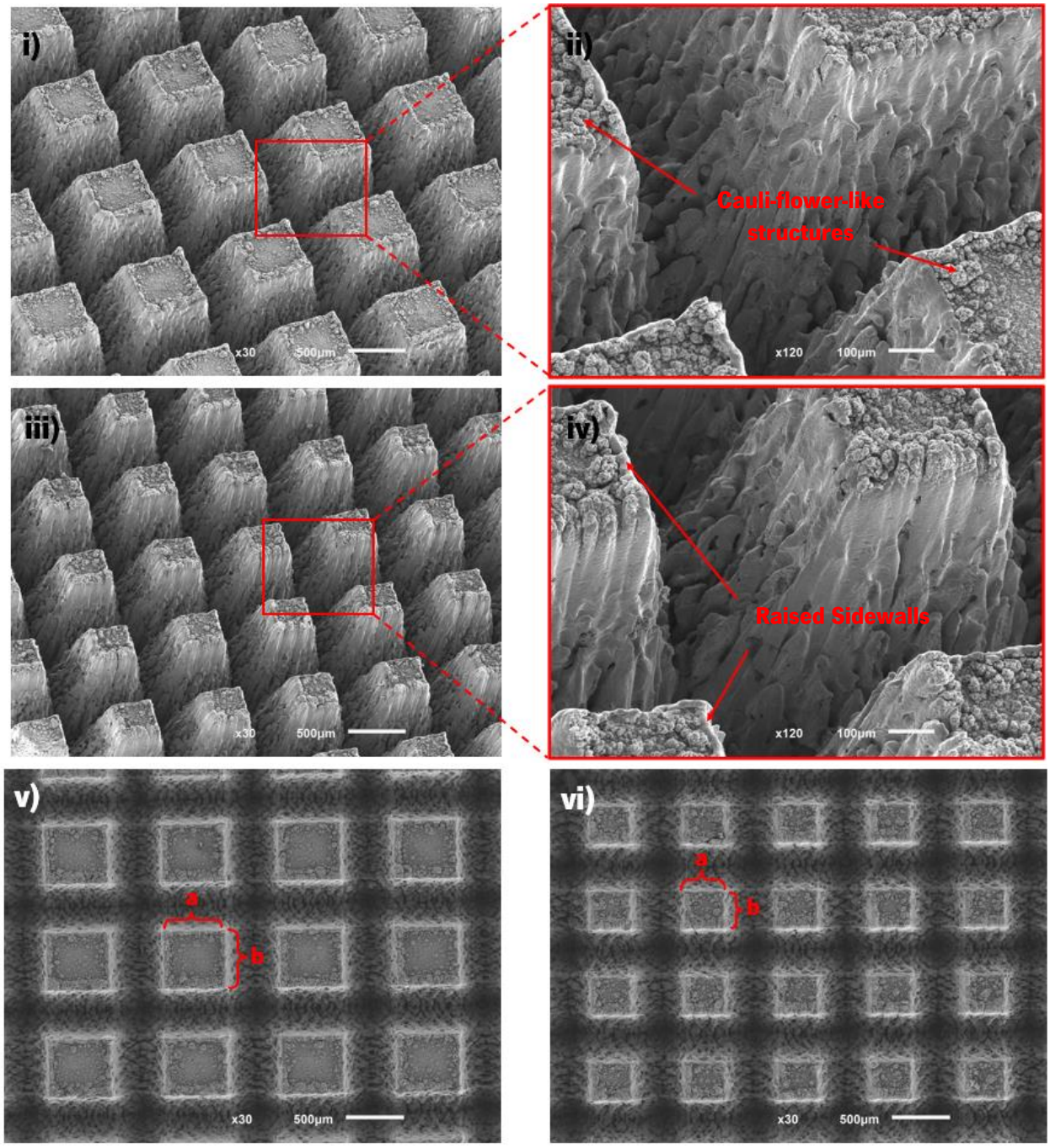

Figure 54 - SEM micrographs (x30, x120) of the textured Ti6Al4V samples: 1mm (i, ii and v); 0.8mm (iii, iv and vi).

Table 19 - Measurements of the structures created by laser texturing: 1mm and 0.8mm patterns.

Measurements / Patterns	1mm	0.8mm
Distance between pillars [µm] ± SD	492.091 ± 5.508	495.143 ± 3.392
Length of (a) [µm] ± SD	486.154 ± 4.098	291.837 ± 5.451
Length of (b) [µm] ± SD	446.222 ± 4.194	244.541 ± 6.285
Depth of Grooves [µm] ± SD	748.468 ± 5.559	751.644 ± 2.345

Regarding the 0.25 mm microtexture, figure 55 presents the results obtained after texturing, mainly regarding surface morphology and topography. Similarly to the macrotextures previously analysed, the parameters used are kept constant, so their influence cannot be studied in this case. This pattern exhibited a distinct surface when compared to the 1 mm and 0,8 mm patterns. The average roughness of these samples is much lower than that of the previous macrostructures, which can be explained by the fewer number of passes used in the texturing of this micropattern: a lower number of passes leads to lower energy provided for material removal, which leads to a smoother surface. Additionally, this texturing process led to the creation of smaller, granular-type structures, that are produced randomly and do not seem to follow a specific cross-hatch pattern. As mentioned previously, the analysis of table 20 confirmed that the distance between ridges is maintained (0,5 mm) regardless of the chosen size of the texture (length of the ridge + length of the groove). Therefore, and since the total size of the microtexture is smaller than the distance between ridges ($0.25\ mm < 0.5\ mm$), there is an overlap in the design, eliminating the untextured area (ridges) and texturing the entire surface of the titanium samples. This leads to the random "excavation" of the material and the production of said structures.

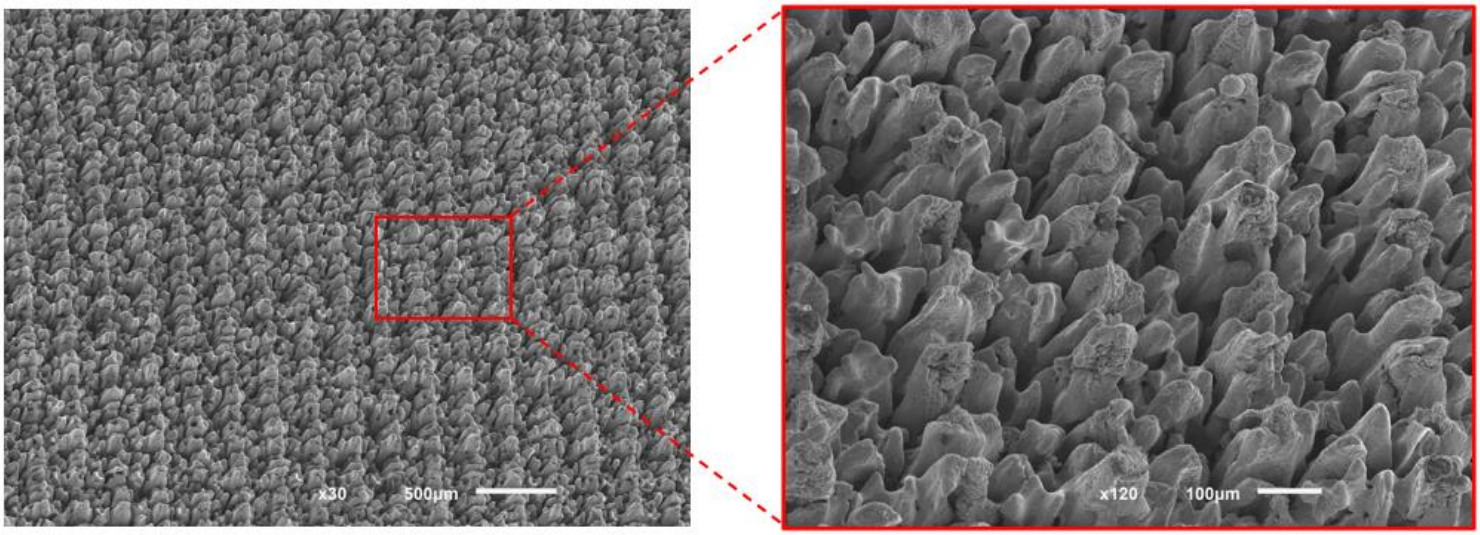

Figure 55 - SEM micrographs (x30, x120) of the textured Ti6Al4V samples: 0.25 mm.

2.2) Hap Coating Characterization

2.2.1) Laser Sintering

A few preliminary studies were conducted in order to optimize the laser sintering process, varying different parameters such as power and scanning speed, following the combinations presented in table 13. It is important to mention, however, that this optimization was performed using dip-coated samples, and the optimal conditions were posteriorly applied to the spin-coated samples. Therefore, the acquired top-view SEM images (50x and 100x) of each condition are depicted in figure 56 and 57, as well as the respective Ca/P ratio obtained through EDS chemical analysis. Previously to any analysis, each coated disk was put through ultrasonic cavitation, in order to evaluate the adherence of the coating created. They were tested one by one, using isopropanol, with 100 W of power for 2 minutes. Appendix B a) and b) presents detailed micrographs of the samples.

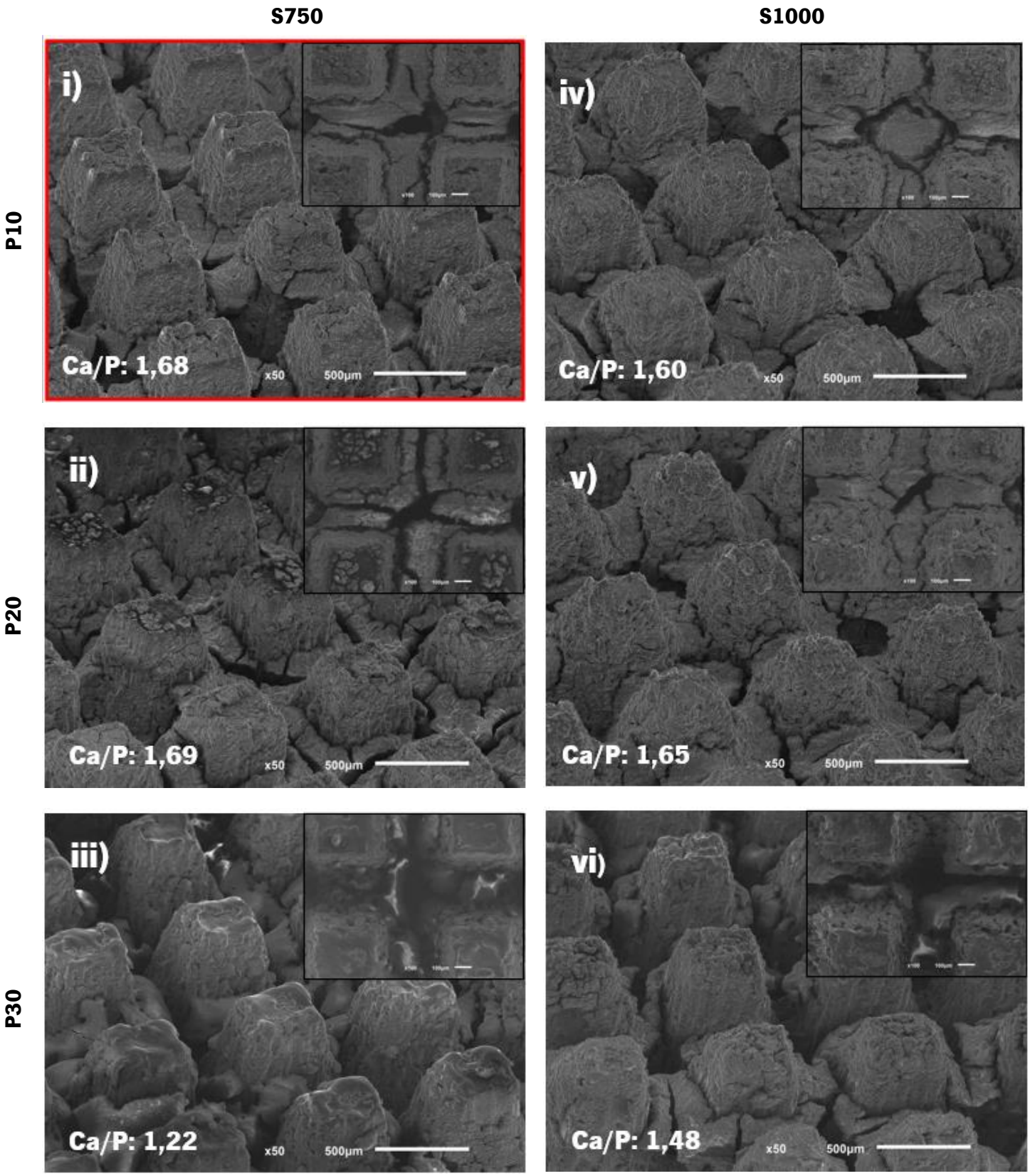

Figure 56 - SEM micrographs (x50, x120) of the laser sintered Hap-coated titanium samples: 0.8mm.

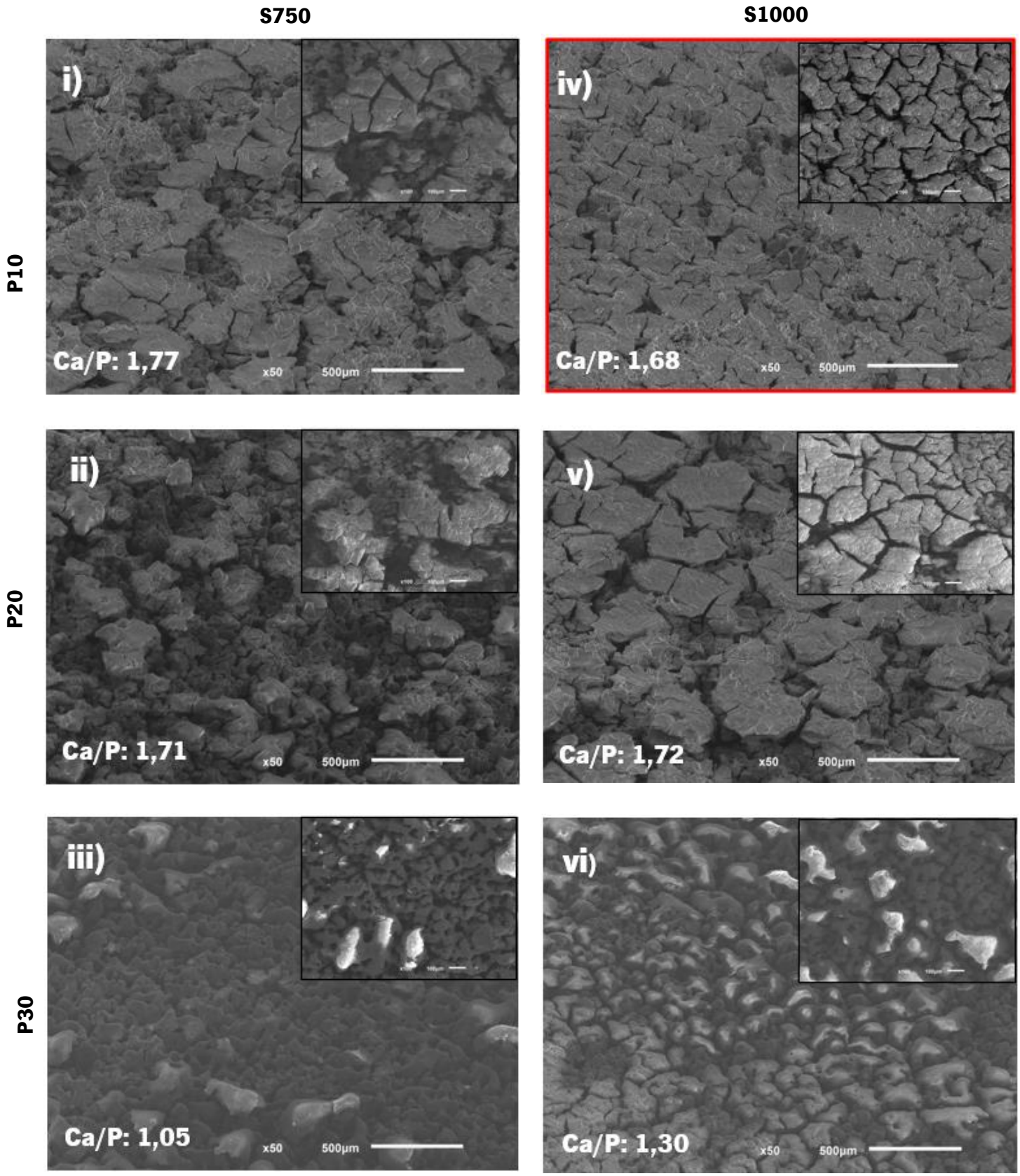

Figure 57 - SEM micrographs (x50, x120) of the laser sintered Hap-coated titanium samples: 0.25mm.

Firstly, it is important to point out some clear flaws that are present in the figures above: the Hap layers formed through dip-coating are not uniform, presenting some major areas of titanium that are not covered by the bioactive material. In fact, and regarding the 0,8 mm texture, the Hap suspension did not reach the bottom of the grooves, and instead unevenly accumulated on the walls and on top of the pillars. This defect was resolved with the change of the mechanism of deposition from dip to spin-coating, as discussed below. Additionally, some major cracks can be observed on every condition tested. However, this is related to the shrinkage of the Hap during laser sintering and is not expected to affect the mechanical interlocking of the coating.

Regarding the 0,8 mm texture, very different morphologies can be observed. Firstly, it can be inferred that 30 W is an excessive amount of power to be used in the laser sintering process, since the Ca/P ratios fall far below the ideal ratio indicated in literature (1,67), which plays a crucial role in the evaluation of the bioactivity of the established coating. In fact, image 56vi) and (especially) image 56iii) seem to indicate that even some melting of the coating occurred, as the amount of energy applied to the surface is too high. Apart from this, the remaining combinations (figure 56i),56ii),56iv) and 56v)) appear to produce adhesive films of sintered Hap, with a normal level of bioactivity. Therefore, in the case of this macrotexture, the ideal condition was chosen according to the Ca/P ratio: **P10S750** registers the closest value to the ideal ratio and was therefore selected (highlighted in red).

Regarding the 0,25 mm texture, a similar conclusion can be drawn: 30 W of power is an excessive value, as images 57iii) and 57vi) register a lamination and partial removal of the Hap film, as well as a very low Ca/P ratio. Additionally, the P20S750 condition also presents a major removal of the coating and is therefore discarded. The remaining combinations can be considered mechanically stable and with a high degree of bioactivity. Between them, the **P10S1000** condition presents the best Ca/P ratio, in addition to the smoothest, most compact and most even coating out of the three. This combination was therefore selected (highlighted in red).

As mentioned, in an initial phase the Hap coating was applied to the surface of the samples by means of dip-coating, before it was altered to a spin-coating method due to defects in the created surfaces. Figure 58 presents the differences in morphology between two sintered coatings obtained through each method (SEM x500 and x100). These samples were created using the same concentration of Hap (0,133 g/mL) and sintering conditions.

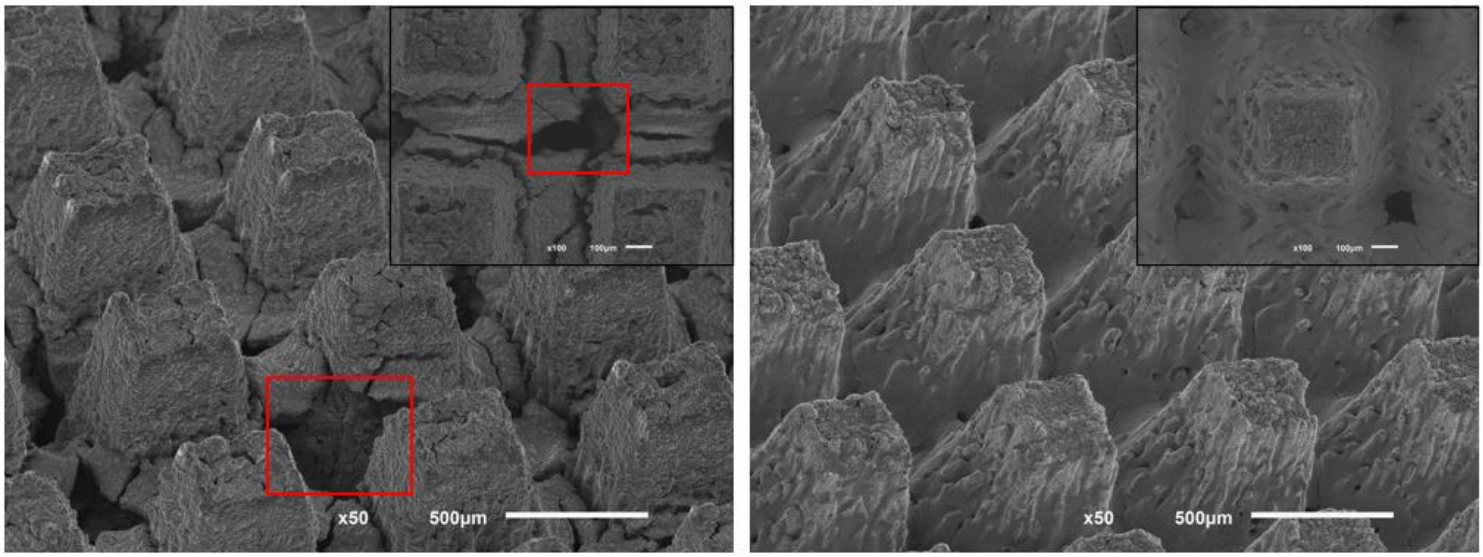

Figure 58 - SEM images (x50, x100) of the Hap-coated Ti6Al4V samples through two different mechanisms: dip-coating (left) and spin-coating (right).

The differences between the two methods are easily spotted. In fact, the Hap layers formed through dip-coating are not uniform, presenting some major areas of titanium that are not covered by the bioactive material (indicated by the red squares). The Hap suspension did not reach the bottom of the grooves, and instead unevenly accumulated on the walls and on top of the pillars. On the other hand, the coating created through spin-coating mechanisms is defined by a uniform deposition of Hap, covering the entire texture and reaching the lower levels of the sample surface. The top of the pillars, however, are not covered by the Hap film.

Figure 59 depicts the final obtained SEM images of the 0,8 mm and 0,25 mm laser sintered Hap-coated surfaces, according to the previously selected conditions. Both with a concentration of 0,133 g/mL, the sintering combinations selected were considered adequate, as the films created are thin but ultrasound resistant, without the presence of major defects, with an appropriate Ca/P ratio that proves their bioactivity, and evenly spread throughout the surface.

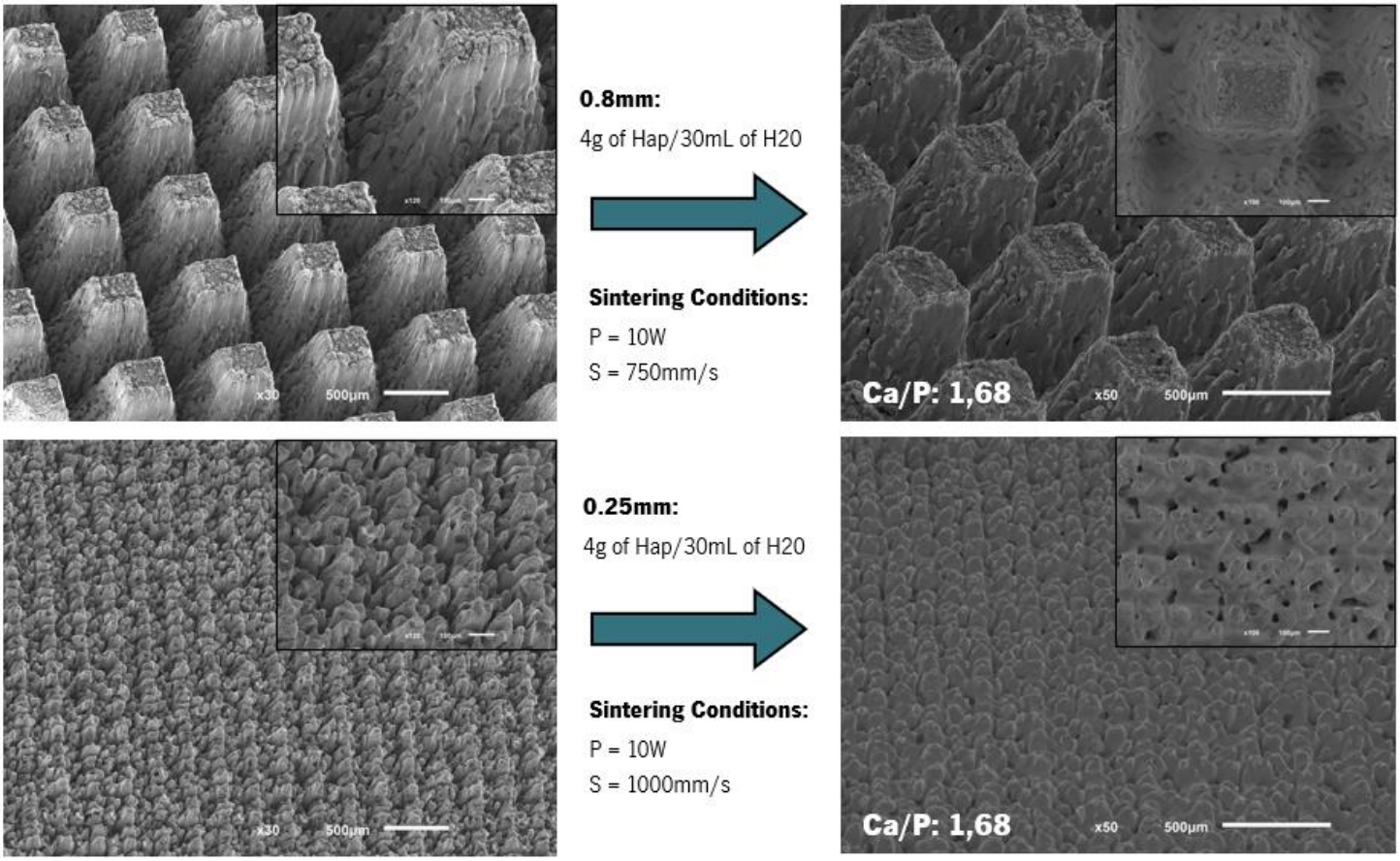

Figure 59 - Ideal Conditions for the laser sintering of the Hap-coated samples.

2.2.2) Conventional Sintering

Conventional sintering was performed in the spin-coated samples, as the dip-coating ones were discarded after the laser sintering procedure, and three different conditions were tested according to table 15. Preliminary studies were conducted involving different furnaces, temperatures, heating rates and pressures for both textures, so that the process was optimized and a uniform active coating was achieved. The concentration of the suspension used was 0,133 g/mL, similar to the laser sintering procedure. Figure 60 presents the top-view SEM images (500x and 100x) of the obtained furnace-sintered samples, as well as their respective Ca/P ratio obtained through EDS. Following the protocol applied to all other coated samples, ultrasound cavitation was performed on all furnace-sintered surfaces (isopropanol, 100 W for 2 minutes) to evaluate their adhesion to the bulk material. Appendix B c) presents detailed micrographs of the samples.

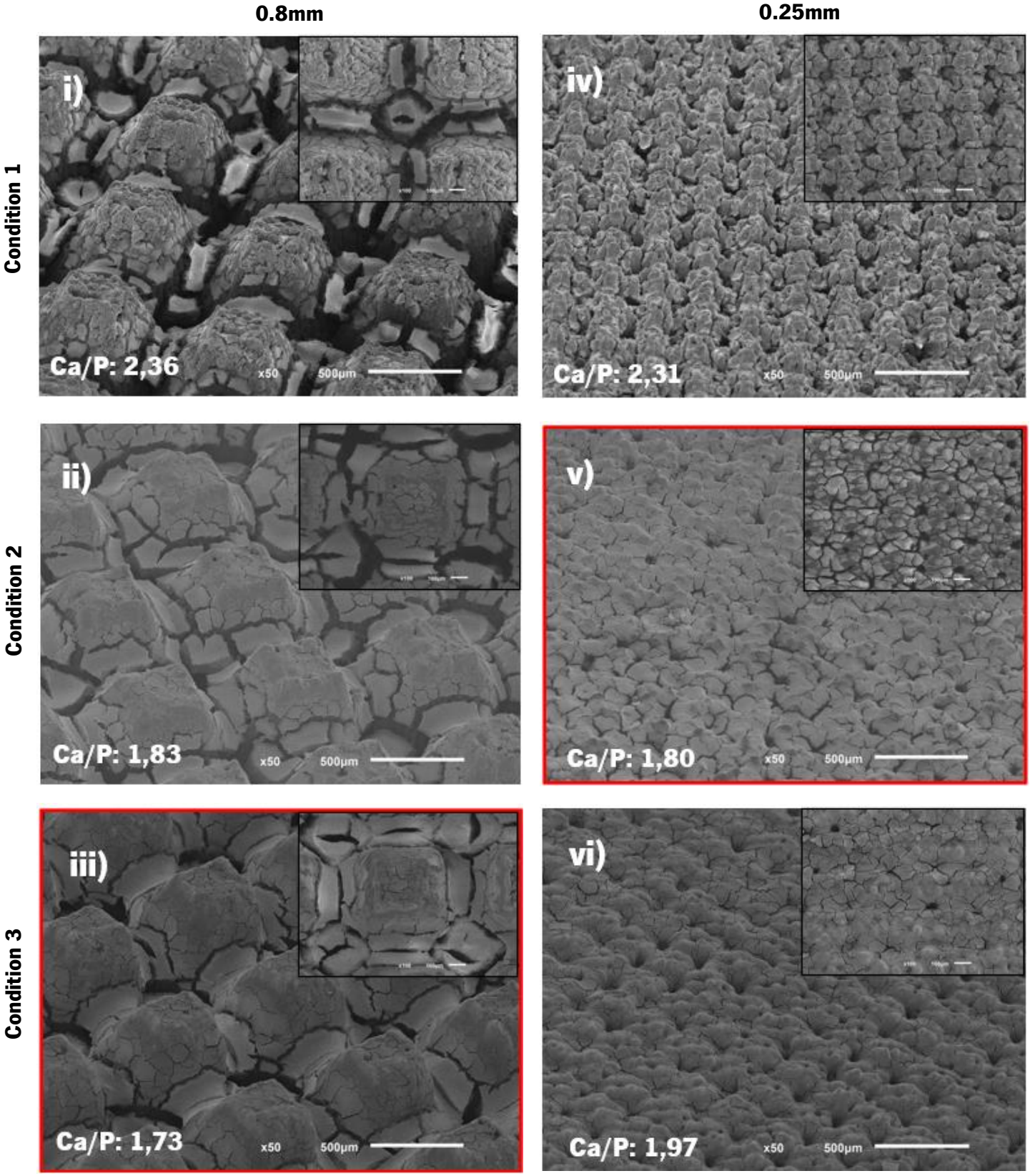

Figure 60 - SEM micrographs (x50, x100) of the Hap-coated titanium samples: 0.8mm (i to iii); 0.25mm (iv to vi).

Regarding the effect of the different conditions on the textures obtained, it can be concluded that the parameters selected for strategy 1 are not ideal. In fact, the created coatings are not as uniform as the other tested conditions, as the material seems to have contracted heavily during the sintering process, and the Ca/P ratio is high, indicating a change in the Hap phase and a transformation into other phosphates, such as TCP. As referred to in Chapter 2, the decomposition of Hap has been shown to commence at around 1150°C, affecting its mechanical and biological properties. However, Weng et al [186] studied the interaction between Ti and Hap during vacuum sintering, analysing the evolution of the composition of the bioactive material through XRD mechanisms. The study concluded that a combination of titanium and a vacuum atmosphere catalysed the thermal decomposition of hydroxyapatite, as the bioactive material started decomposing at 800-900°C, forming α-TCP. Therefore, it can be concluded that in condition 1 the Hap coating is already partially decomposed and compromised. Consequently, this strategy is discarded.

Regarding the morphology of the remaining textures in conditions 2 and 3, it is observed that they are similar both for the 0.8 mm and 0.25 mm textures, presenting uniform and ultrasound resistant coatings. However, the Ca/P ratios vary. It is reported in literature that the range of expected Ca/P for sintering temperatures between 800°C and 1200°C is 1.4 to 2 [187]. Therefore, every texture produced from these conditions can be considered adequate.

The ideal combinations were chosen based on the ratio closest to the ideal value for pure Hap (1,67). Therefore, the chosen textures are highlighted in red: **condition 3** was used to produce **0.8 mm** samples and **condition 2** to produce **0.25 mm** samples. Consequently, both the tubular furnace and the conventional muffle were used to sinter titanium-coated disks. The before and after-coating top-view SEM images (500x and 100x) are presented in figure 61, as well as the different sintering conditions used for each texture and consequent Ca/P ratios obtained.

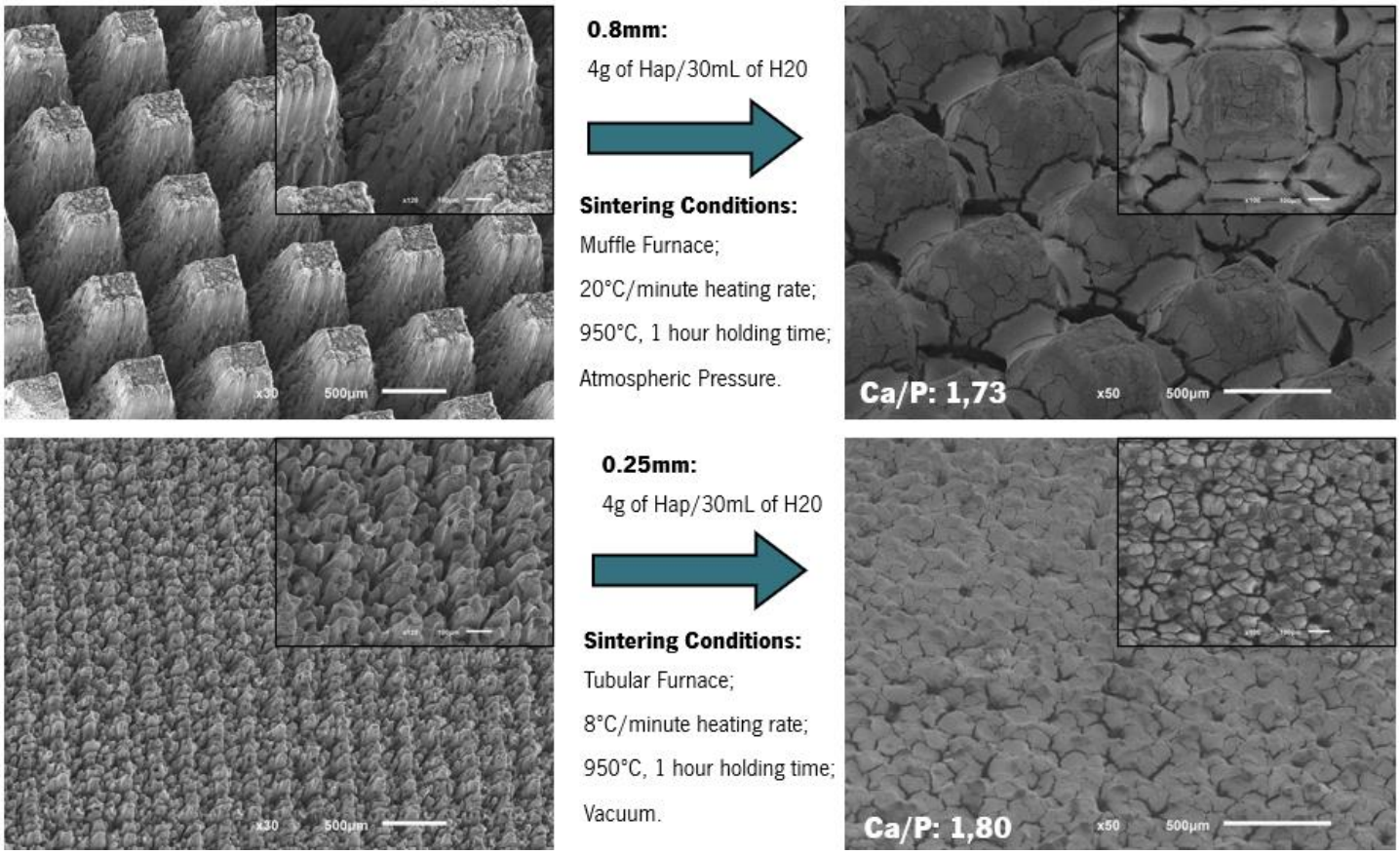

Figure 61 - Ideal Conditions for the furnace sintering of the Hap-coated samples.

2.3) Wettability

In order to investigate the influence of the different combinations of micropatterns produced by LST, the incorporation of a Hap coating on the titanium surface wettability and the different sintering conditions applied, contact angle measurements were performed. Ultrapure water (at 18.2 Ohm), with a volume of 5 µL and a dosing rate of 2.5 µL/s, was used as testing media. This solution was dispensed from a micrometric syringe, brought in contact with the sample surface and allowed to stabilize before the reading was taken. Figure 62 shows the contact angles obtained for each tested condition, as well as the profile image of one of the measurements performed for each condition.

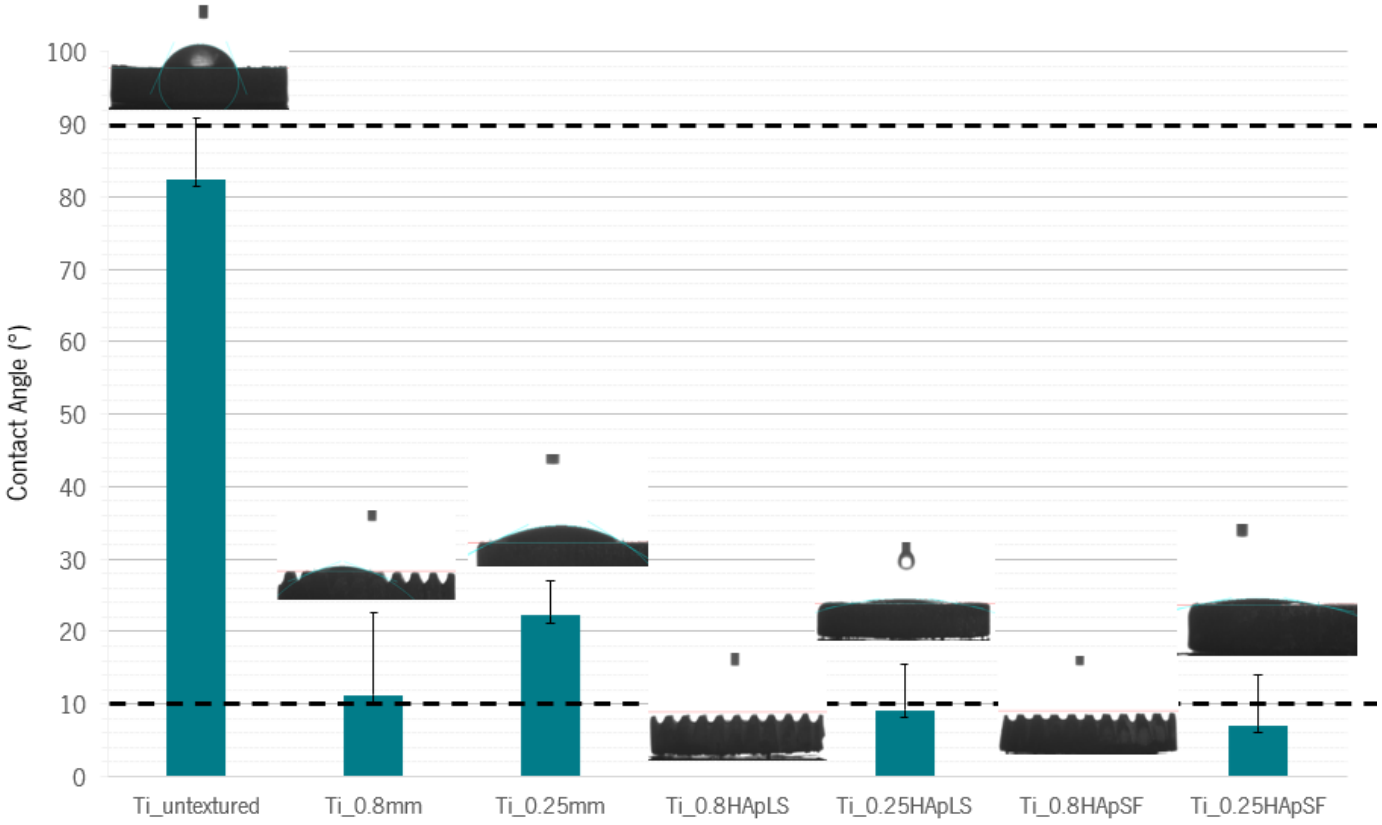

Figure 62 - Apparent contact angles obtained by sessile drop measurements from all the tested conditions.

The results obtained show that the smooth titanium surface, that serves as control group, already has a WCA below 90° (82.5 ± 8.34°), therefore being described as a hydrophilic surface. However, the texturization of said surface enhances that hydrophilicity, as can be observed by the contact angles obtained for the 0.8 mm (11.25 ± 11.31°) and 0.25 mm (22.22 ± 4.83°) textures. The macrotextures present a lower contact angle when compared to the microtextures, demonstrating a contact angle almost in the range of the superhydrophilic behavior ($\theta < 10^{\circ}$). Therefore, the textured samples follow the Wenzel model, as water tends to spread easily throughout the surface with the increase of roughness, and a homogeneous wetting is achieved.

The addition and sintering of the Hap coating had similar effects on the wettability of said surfaces. In fact, a further reduction in WCA is accomplished in every coating condition, although more accentuated in some than in others. Regarding the laser sintering process, it can be observed that the 0.8mm textures present a lower contact angle (0 ± 0°) than the 0.25 mm textures (9.14 ± 6.3°), although both surfaces are superhydrophilic. In fact, the 0.8 mm disks behave as an ideal wetting surface, allowing the complete spread of the water drop. According to literature, this is due to the strong electrostatic interactions

established between water molecules and the calcium and phosphate ions present in hydroxyapatite during hydration, which in turn promote bonding and increase surface wettability [188]. In comparison, and as expected, conventional sintered samples also possess superhydrophilic nature. Similarly, the 0.8 mm texture (0 ± 0°) presents a lower contact angle when compared to the 0.25 mm microtexture (6.98 ± 7.14°), behaving as an ideal wetting surface. When contrasting the two sintering methods, it can be concluded that the 0.8mm textures produced are identical, whereas the 0.25 mm texture produced by furnace sintering presents a slightly lower WCA than the one produced by laser sintering and, consequently, a slightly more hydrophilic behaviour.

2.4) Friction Tests

In order to evaluate the tribological performance of the created samples, as well as the structural integrity of the produced micropatterns in an environment mimicking the insertion of a knee prosthesis, reciprocating friction tests were employed. The tests were performed according to the conditions reported in Chapter 3, and the COF results for each tested condition are present in figure 63. Appendix B d) presents detailed micrographs of the samples.

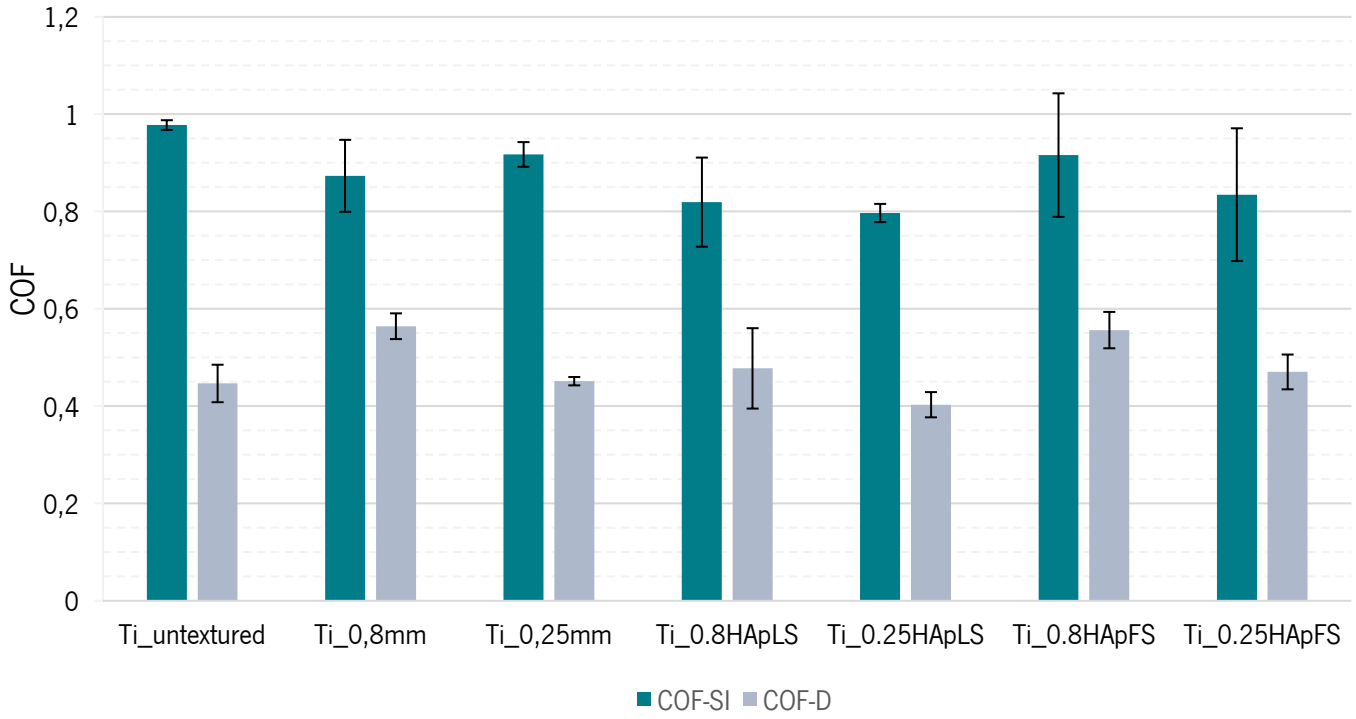

Figure 63 - Average coefficient of friction (COF) obtained for all tested conditions. COF-SI and COF-D denotes the static and dynamic coefficient of friction, respectively.

Similarly to what was registered in the zirconia samples, it can be observed that the static COF was higher than the dynamic COF for all tested conditions. These results were expected, as this behaviour emulates that of the mechanism of adhesion and compaction of bone: the sliding causes bone debris to

accumulate in the asperities of the titanium surfaces, which leads to the contact interface gradually transitioning from bone-sample to bone-bone. This leads to a decrease in the dynamic COF, and the required friction force to maintain the relative motion is lower compared to the one that is required to initiate relative motion.

Another phenomena registered during the reciprocating friction tests for the zirconia samples can be observed in figure 63: the static COF of the untextured samples was slightly higher than any other condition tested. This was not expected, since there is evidence in literature that an increase in surface roughness is typically accompanied with an increase in the static COF of said surface and respective tribological performance [124,129]. As already referred for the zirconia samples, the explanation for this occurrence may reside in the normal load that was used, which may be too small to cause bone deformation in the initial sliding moment, which in turn does not cause bone debris to accumulate in the sample surface. Since the static COF is dependent on the apparent contact area of the surface [184], and the smooth titanium surfaces possess a bigger apparent contact area than the textured samples, the static COF of said samples will also be higher. However, the sliding movement during the rest of the friction tests eventually deforms the bone and causes its entrapment in the asperities of the textured samples, which is indicated by the higher dynamic COF of these samples, when compared to the untextured surfaces. It is fundamental to validate this theory through the analysis of the SEM images regarding the various titanium samples, focusing on the bone retention process.

Regarding the textured surfaces, the static COF is practically the same for both patterns, as the 0.25 mm samples present a COF 5% higher than the 0.8 mm pattern. Additionally, both textures seem to hold said friction performance after the addition and sintering of the Hap coatings. In fact, the 0,8mm pattern registers a variation (decrease and increase) of about 6% after the addition of laser and furnace sintered coatings, which can be considered as residual. This preservation of tribological performance occurs since the Hap layer added does not fully cover the grooves of the titanium samples, allowing for the preservation of some sample depth, which leads to a similar friction behaviour in all tested conditions. Regarding the 0.25 mm samples, and even though the variation registered was more significant, especially for the laser sintered condition (12% decrease), the friction performance of the coated samples can also be considered constant. Therefore, in contrast to what is registered in the zirconia surfaces, it can be concluded that the main factor dictating the tribological behaviour of the titanium surfaces is the pattern created, not the added Hap coating.

In order to verify the above-mentioned assumptions, the morphology of both the zirconia and the bone worn samples was observed by SEM. Figure 64,65 and 66 shows the SEM micrographs (x150; x40) of the bone and zirconia surfaces after the friction tests. EDS analysis was also performed in said samples.

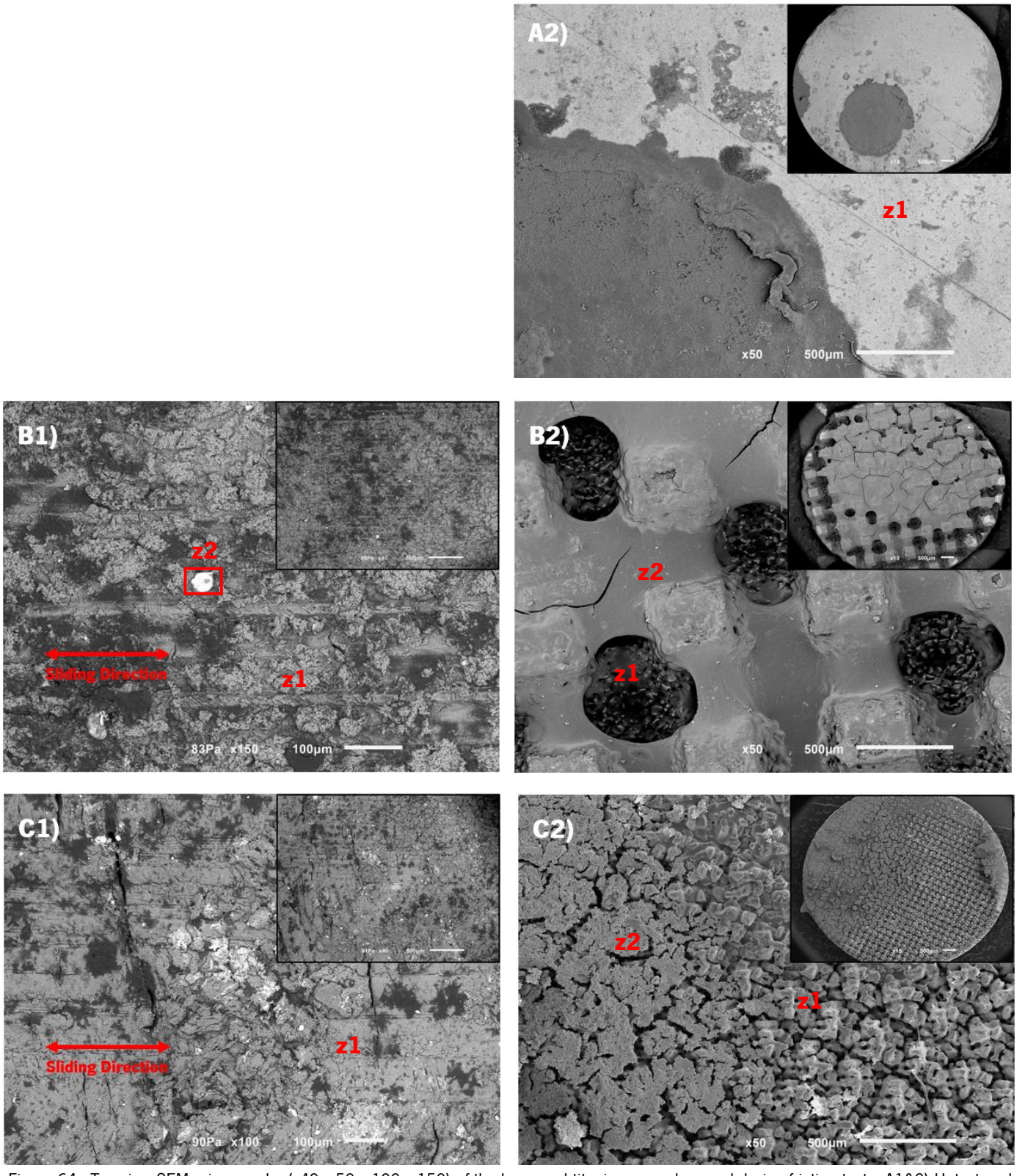

Figure 64 - Top-view SEM micrographs (x40, x50, x100, x150) of the bone and titanium samples used during friction tests. A1&2) Untextured sample; B1&2) 0.8mm sample; C1&2) 0.25mm sample.

Bone samples: z1 – Bone; z2 – Ti6Al4V. **Ti6Al4V samples:** z1 – Ti6Al4V; z2 – Bone; z3 – HAp.

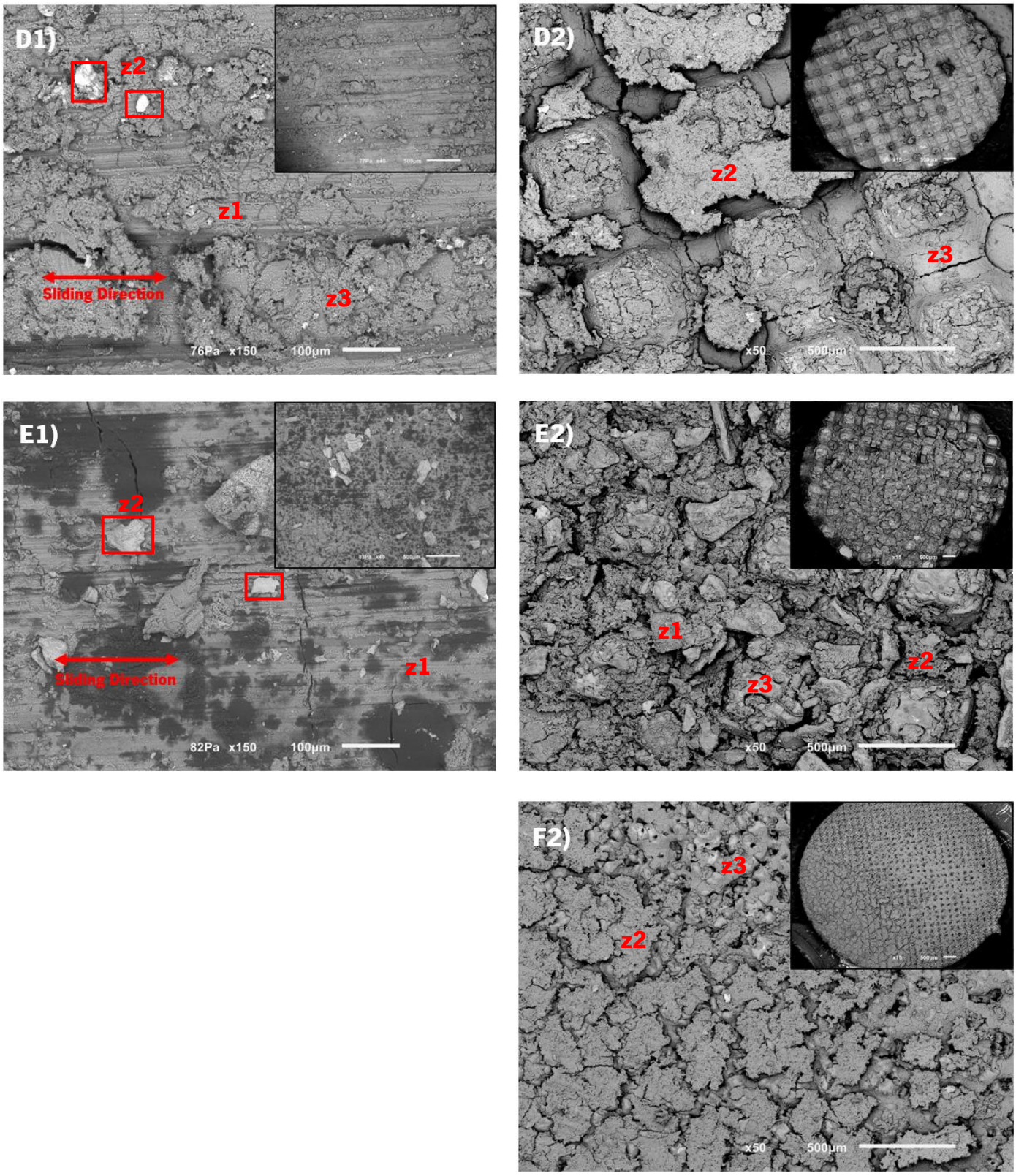

Figure 65 - Top-view SEM micrographs (x40, x50, x100, x150) of the bone and titanium samples used during friction tests. D1&2) 0.8mm_LS sample; E1&2) 0.8mm_CS sample; F1&2) 0.25mm_LS sample.

Bone samples: z1 – Bone; z2 – Ti6Al4V; z3 – HAp. **Ti6Al4V samples:** z1 – Ti6Al4V; z2 – Bone; z3 – HAp.

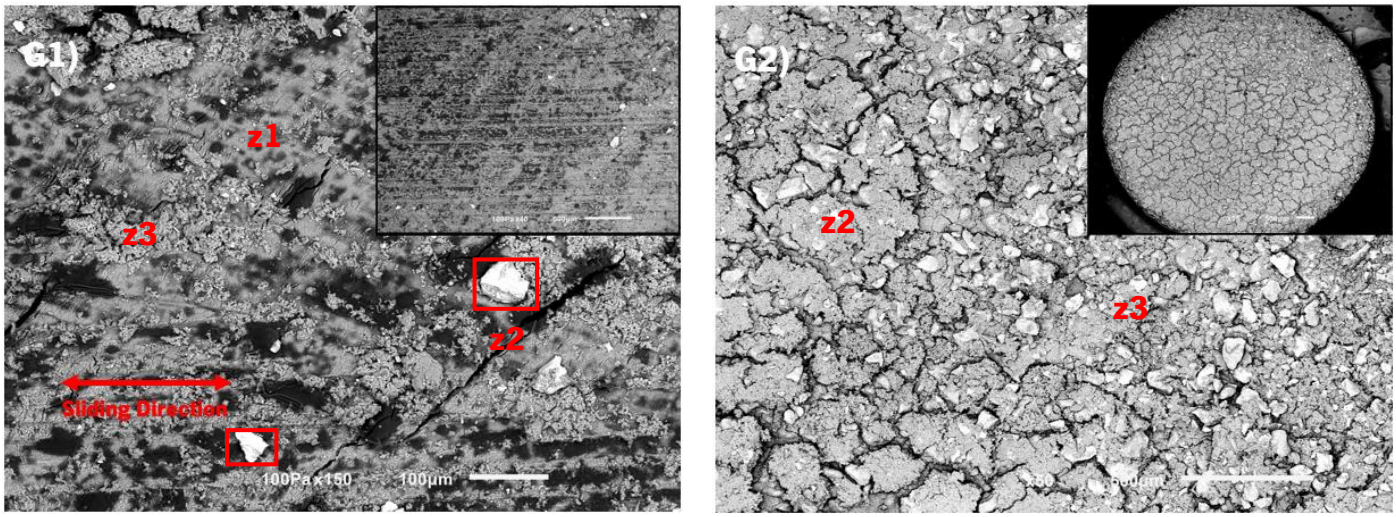

Figure 66 - Top-view SEM micrographs (x40, x50, x100, x150) of the bone and titanium samples used during friction tests. G1&2) 0.25mm_CS sample.

Bone samples: z1 – Bone; z2 – Ti6Al4V; z3 - HAp. **Ti6Al4V samples:** z1 – Ti6Al4V; z2 – Bone; z3 – HAp.

Analysing the images obtained by SEM technology, it seems clear the presence of adhesive mechanism on the titanium samples (bone material adhered to the samples surface) and abrasion mechanisms on the bone surfaces (grooves aligned with the sliding direction). The adhesion of bone can clearly be seen in the micrographs of the samples, as well as in the EDS analysis performed in all studied samples.

The main elements found on the surface of the titanium surfaces were Titanium (Ti), Aluminium (Al), Vanadium (V), Calcium (Ca) and Phosphorus (P). The Ti, Al and V elements come from the bulk titanium disk (z1), while Ca and P are the main components of bone (z2). The phenomena of bone retention can be seen in all the tested conditions, with the exception of the smooth-untextured surfaces. The 0.8 mm patterned samples seem to present a higher rate of bone retention when compared to the 0.25 mm patterns, as well as a more uniform debris spread throughout the texture. In fact, this debris tends to cover the lower levels of the titanium samples such as grooves and deeper pits, except in the case of the 0.8mm textured pattern, in which a bone layer was formed on top of the ridges (figure 64B2). The presence of this titanium structures leads to a higher connection between the substrate and the bone surface, which in turn results in a better friction performance. The mechanical integrity of said structures remains intact during the entirety of the tests and is not compromised by the friction mechanisms. However, the titanium oxides formed on the sample surface tended to break under sliding, and were, as a result, deposited on the bone surface in almost all tested conditions.

Regarding the bone surfaces, figure 64, 65 and 66 shows the difference between the various conditions tested. It can clearly be concluded that all textured samples produced pronounced grooves on the substrate. These grooves are well-defined and aligned with the sliding direction of the titanium samples. In contrast, the untextured samples do not produce any major marks, which means that bone deformation does not occur in these conditions. Therefore, the theory previously formulated is valid: the low normal load applied to the textured samples is not enough to penetrate and remove bone matter, which explains the low static COF. However, as the friction test progresses, the textured samples eventually deform the substrate, producing bone debris and entrapping it in surface asperities. Regarding the coated samples, small Hap particles can be observed in some areas of the bone surface, mainly composed of Ca and P, which were detached from the titanium samples and lodged in the bone interface (z3). Additionally, and as previously mentioned, small pieces of titanium oxides can also be identified (red squares – z2). The size of the grooves produced by the 0.8 mm patterned samples seem to be slightly more pronounced when compared to the 0.25 mm patterned samples. The incorporation of coatings to said textures does not influence the topography of the marks produced in the bone samples, as the grooves maintain similar sizes and topography after the addition of the sintered Hap layers. Therefore, it can be concluded that the main agent that dictates the adhesion of bone and regulates the friction performance of the titanium samples is the topography of the surface and the microstructures produced.

3) Summary

3.1) Zirconia

Regarding the zirconia surfaces, different patterns were successfully created and characterized without major distortions or cracks. Two different strategies were adopted for the texturing process: the L16Pn strategy, that created macrotextures, and the D20PnSm strategy, that produced microtextures. The variation of the machining parameters was studied and, in the case of the macrostructures, different types of structures and depths were achieved. The dimensions of grooves, ridges and ridge walls were measured, as well as the distance between said structures. In the microtextures, the roughness values obtained were relatively identical. Three distinct textures, two macro (L16P35N=2 and L16P40N=3) and one micro (D20P20S128N=1) were then selected and the MTA coating procedure was tested in said samples. Good mechanical interlocking was achieved in the macrotextures, while the microtexture was discarded since the coating disintegrated after polishing and ultrasonic cleaning. The L16P40N=3 was considered the optimal texture, due to its appropriate depth and topography.

Wettability tests revealed a higher contact angle in the textured samples in comparison to smooth and MTA-coated surfaces. It was therefore concluded that the produced structures lead to the creation of a Cassie-Baxter modelled surface, in which the air was entrapped beneath the drop and prevented the water reaching the lower depths of the grooves. The MTA coating presented the lowest surface contact angle out of the three measured conditions since the porosity of the bioactive layer enhanced surface hydrophilicity.

Subsequent reciprocating friction tests showed that the static COF was higher than the dynamic COF for all tested conditions. However, the static COF of untextured samples was higher than that of textured samples, which was not expected. This was explained by the low normal load applied to the samples, which prevented the initial deformation of bone and lead to the simple sliding of the surface, without the formation of debris. Since the smooth samples have a higher apparent contact area, the static COF obtained for said surfaces was higher. After examining the bone surface, it was concluded that only the textured samples produced grooves on the bone surface, which means that, with the progression of the test, the samples eventually penetrated the surface. This is evident by the higher dynamic COF presented by these samples, in comparison to the smooth samples. Additionally, analysis of the tested zirconia samples shows that only the textured samples retain bone matter. Regarding the MTA-coated surfaces, these samples exhibited an increase in static COF compared to the textured surfaces. This is due to the higher chemical affinity of the bioactive material since the chemical structure of the coating is similar to that of the bone. Therefore, MTA has an important role in the adhesion of bone and in regulating the friction performance of zirconia samples.

Finally, the biological tests revealed that the MTA samples present slightly higher numbers of fibroblasts when compared to the two smooth surfaces, and almost identical numbers to the control group, which is a testament to their higher biocompatibility. The textured zirconia samples obtained the lowest percentage of alive cells out of all conditions, and there was no significant difference between the two used materials (zirconia and titanium) regarding smooth surfaces.

3.2) Titanium

Regarding the titanium surfaces, different patterns were successfully created and characterized without major distortions or cracks. Three different strategies were employed in the texturing process: 1 mm, 0.8 mm and 0.25 mm textures, which represent the length of a pillar and respective groove. Much like what happened with the zirconia samples, the texturing procedure created two types of textures: macrotextures (1 mm and 0.8 mm) and microtextures (0.25 mm). The dimensions of grooves and ridges

were measured, as well as the distance between said structures. In the microtextures, the average roughness was also obtained. One macrotexture (0.8 mm) and one microtexture (0.25 mm) were then selected and the Hap coating procedure was tested in said samples. Two different forms of sintering were used in order to compact and consolidate the bioactive layer: laser and furnace sintering. Optimization tests were developed in order to assess the ideal sintering conditions for each technique, and two different types of furnaces were used in the conventional sintering technique. Good mechanical interlocking was achieved in both textures, even after polishing and ultrasonic cleaning, as well as acceptable Ca/P ratios through EDS technology.

Even though smooth-untextured samples presented the highest contact angle out of all tested conditions, the WCA showed that this surface was already hydrophilic. Therefore, every obtained condition obeyed the Wenzel model, as water tends to spread easily throughout the surface with the increase of roughness, and a homogeneous wetting was achieved. In fact, the texturization of the samples led to a considerable decrease in the WCA for both patterns studied, and all coated samples presented superhydrophilic behaviour, especially the 0.8 mm samples, that were considered ideal wetting surfaces. This is due to the strong electrostatic interactions established between water molecules and the calcium and phosphate ions present in hydroxyapatite during hydration, which in turn promotes bonding and increases surface wettability.

Similarly to what was registered in the zirconia samples, reciprocating friction tests showed that the static COF was higher than the dynamic COF for all tested conditions, which signifies that the mechanism of adhesion and compaction of bone was also present in these titanium samples. Another phenomena registered during the reciprocating friction tests for the zirconia samples was observed: the static COF of the untextured samples was slightly higher than any other condition tested. This was due to the low normal load imposed on the samples, which causes the sample to simply slide on the surface of the bone, without deforming the bone or producing debris. After observing the SEM images regarding the bone samples, it is observed that only the textured and coated samples produced grooves on the substrate, which clearly corroborates the previously made assumption: with time, the titanium sample penetrates and removes bone from the surface. The static COF is practically the same for both patterns, and both textures seem to hold said friction performance after the addition and sintering of the Hap coatings. This preservation of tribological performance occurs since the Hap layer added does not fully cover the grooves of the titanium samples, allowing for the conservation of some sample depth, which leads to a similar friction behaviour in all tested conditions. The analysis of the SEM images regarding the

titanium samples shows that the 0.8 mm patterned samples seem to present a higher rate of bone retention when compared to the 0.25 mm patterns, as well as a more uniform debris spread throughout the texture. The mechanical integrity of the textures remains intact during the entirety of the test, but the titanium oxides formed on the sample surface tended to break under sliding, and were, as a result, deposited on the bone surface in almost all tested conditions. Therefore, in contrast to what is registered in the zirconia surfaces, it can be concluded that the main factor dictating the tribological behaviour of the titanium surfaces is the pattern created, not the added Hap coating.

CHAPTER V

CONCLUSIONS

Chapter V presents the main conclusions drawn from this work, as well as some suggestions for future works.

1) Conclusions

The present dissertation reports the production, characterization and optimization of various surface patterns produced via laser surface texturing on two different bulk materials, as well as the creation of various bioactive coatings through different methods. The main purpose of the work was to develop novel bioactive surfaces in order to improve the stability and osseointegration of the knee implants. After the completion of this work, it was possible to conclude the following:

- Cross-hatched textures were successfully produced in both bulk materials. The variation of the texturing parameters created samples with various depths and distinct structures, while the usage of different patterns provided samples with macrotextures and microtextures. No major problems were encountered, as the texturing produced samples with regular porosity, no major cracks and adequate sizing;

- Coatings were created through different techniques: cold pressing in the creation of the MTA coatings, and laser/furnace sintering in the creation of the Hap coatings. The initial MTA coatings obtained were not optimized, as most of the coating was removed during ultrasonic cleaning. After the alteration of the cold-pressing technique, compact and thick layers were achieved, without the presence of major flaws. Regarding the Hap coatings, the optimization process involving different parameter combinations led to the creation of samples with adequate Ca/P ratios and morphology, while the change from dip-coating to spin-coating produced a uniform deposition of the bioactive suspension;

- The characterization techniques employed in the work were fundamental to understand the results. SEM observations allowed to characterize the surface topography and morphology with respect to precision of the laser texturing process, surface micro and nanofeatures and coating defects such as microcracks. EDS analysis enabled the inspection of Ca/P ratios, while the roughness evaluations allowed the characterization of the microtextures;

- Surface topography had a significative impact in controlling the wetting behaviour of the surfaces. In the case of the zirconia samples, the texturing process increased the WCA due to the retention of air in the grooves beneath the drop, following a Cassie-Baxter model, while in the titanium samples the texturing process enhanced hydrophilicity, as the interface presented very low values

of WCA. The addition of the bioactive coatings resulted in the reduction of the contact angle in both materials and for all tested patterns. In fact, the titanium Hap-coated samples revealed a superhydrophilic behaviour, while the addition of the MTA coating to the zirconia surfaces enhanced wetting conditions, achieving a WCA lower than the smooth-untextured samples;

- The friction tests revealed that the adhesion of bone to the created samples occurred in every condition, apart from the untextured original samples. The initial static COF of textured samples was lower than that of the smooth surfaces, mainly due to the low normal load imposed during testing. Bone surfaces reveal that grooves were obtained for all textured conditions, which, in combination with high dynamic COFs, reveals that the samples eventually remove bone matter and created debris that accumulates in the surface asperities. The addition of coatings did not cause the loss of friction performance in any of the tested conditions.

- Cell viability tests shown that the MTA-coated samples presented better numbers when compared to zirconia and titanium smooth surfaces, with numbers almost identical to the control group. However, the textured samples revealed the lowest percentage of alive cells out of all conditions, and there was no difference between the bulk materials.

2) Suggestions for future works

Considering the previous conclusions, here are some suggestions for future works:

- ✓ Explore the adaptation of other bioactive and bulk materials used in the biomedical field, creating different combinations that may result in viable and enhanced solutions (PEEK and β-TCP, for example);

- ✓ Adapt the coating technique used in the zirconia samples and test the production of MTA coatings in the titanium textured samples;

- ✓ The titanium samples presented oxides in the surface, which tended to break during sliding tests. It would be interesting to remove these oxides using acid treatment before the friction analysis.

- ✓ Investigate the effect of depth in the mechanical interlocking of the MTA coating to the zirconia substrate, since in this work only two different conditions were evaluated;

- ✓ In this work, the created microtextures did not successfully retain the MTA coating, since the bioactive layer was destroyed after a single ultrasonic cavitation test. Therefore, it would be interesting to investigate and develop a microtexture that mechanically accommodates said coating, as these patterns are easier and faster to produce;

- ✓ Mechanical validation of the functionalized samples through flexural strength tests, since the laser processing of the surfaces may influence the base material;

- ✓ Investigate the low cell viability exhibited in the textured zirconia samples, which was not expected;

- ✓ Expand the cell viability tests using fibroblasts, testing more conditions and extending the cell culture time;

- ✓ Explore the antibacterial properties of the MTA layer through bacterial incubation tests;

REFERENCES

[1] Gray, H. (2013). *Grays Anatomy*. Arcturus Publishing.

[2] Shapiro, F. (2008). Bone development and its relation to fracture repair. The role of mesenchymal osteoblasts and surface osteoblasts. *European Cells and Materials*, *15*, 53–76.

[3] Black, J. D., & Tadros, B. J. (2020, June). Bone structure: from cortical to calcium. *Orthopaedics and Trauma*, *34* (3), 113–119.

[4] HADJIDAKIS, D. J., & ANDROULAKIS, I. I. (2006, December 1). Bone Remodeling. *Annals of the New York Academy of Sciences*, *1092* (1), 385–396.

[5] Rucci N. (2008). Molecular biology of bone remodelling. *Clin Cases Miner Bone Metab.*;5(1):49-56.

[6] Yuan, X., Kang, Y., Zuo, J., Xie, Y., Ma, L., Ren, X., Bian, Z., Wei, Q., Zhou, K., Wang, X., & Yu, Z. (2018). Micro/nano hierarchical structured titanium treated by NH4OH/H2O2 for enhancing cell response. *PLOS ONE*, *13* (5).

[7] Dhinakarsamy, V., & Jayesh, R. (2015). Osseointegration. *Journal of Pharmacy and Bioallied Sciences*, *7*(5), 228.

[8] Koh, C. K., Zeng, I., Ravi, S., Zhu, M., Vince, K. G., & Young, S. W. (2017). Periprosthetic Joint Infection Is the Main Cause of Failure for Modern Knee Arthroplasty: An Analysis of 11,134 Knees. *Clinical Orthopaedics &Amp; Related Research*, *475*(9), 2194–2201.

[9] Koh, C. K., Zeng, I., Ravi, S., Zhu, M., Vince, K. G., & Young, S. W. (2017). Periprosthetic Joint Infection Is the Main Cause of Failure for Modern Knee Arthroplasty: An Analysis of 11,134 Knees. *Clinical Orthopaedics &Amp; Related Research*, *475* (9), 2194–2201.

[10] Carr, A. J., Robertsson, O., Graves, S., Price, A. J., Arden, N. K., Judge, A., & Beard,D. J. (2012). Knee replacement. *The Lancet*, *379* (9823), 1331–1340.

[11] Arden N, Nevitt MC. (2006). Osteoarthritis: epidemiology. *Best Pract Res Clin Rheumatol*; 20: 3–25.

[12] Price A, Allum R. (2010). Management of osteoarthritis of the knee. *Ann R Coll Surg Engl*; 92: 459–62.

[13] Emsley D, Newell C, Pickford M, Royall M, Swanson M. (2008). National Joint Registry for England and Wales, 5th annual report.

[14] Varacallo M, T David Luo, N. A. Johanson. (n.d). Total Knee Arthroplasty Techiques.

[15] Diane M. Heislein, Eric O. Eisemon. (2016). Pathology and Intervention in Musculoskeletal Rehabilitation (Second Edition).

[16] Kennedy. W. R., White, R. P. (1985). Unicompartmental Arthroplasty of the Knee. Postoperative Alignment and Its Influence on Overall Results. *Clin. Orthop.* 221: 278-285.

[17] Hunt LP, Ben-Shlomo Y, Clark EM. (2014). National Joint Registry for England and Wales. 45-day mortality after 467,779 knee replacements for osteoarthritis from the National Joint Registry for England and Wales: an observational study. *Lancet*; 384:1429-36.

[18] Liddle AD, Judge A, Pandit H, Murray DW. (2014). Adverse outcomes after total and unicompartmental knee replacement in 101,330 matched patients: a study of data from the National Joint Registry for England and Wales. *Lancet* ;384:1437-45.

[19] Homayoun Siman, MD, Atul F. Kamath, MD, Nazly Carrillo, MD, William S. Harmsen, MS, Mark W. Pagnano, MD, Rafael J. Sierra, MD. (n.d). Unicompartmental Knee Arthroplasty vs Total Knee Arthroplasty for Medial Compartment Arthritis in Patients Older Than 75 Years: Comparable Reoperation, Revision, and Complication Rates.

[20] *Partial Knee Replacement*. (2021, December 8). Dr. Craig J. Della Valle, Hip and Knee Surgeon. https://dellavalleortho.com/education/partial-knee-replacement/

[21] P. Maressa, L. Anodio, A. Bernasconi, A. G. Demir, and B. Previtali. (2014). "Effect of surface texture on the adhesion performance of laser treated Ti6Al4V alloy," Journal of Adhesion, vol. 91, no. 7, pp. 518– 537.

[22] Z. Ozkurt, E. Kazazoglu. (2011). Zirconia dental implants: a literature review, *J. Oral Implantol*. XXXVII 367–376.

[23] Y.-D. Cho, J.-C. Shin, H.-L. Kim, M. Gerelmaa, H.-I. Yoon, H.-M. Ryoo, D.-J. Kim, J.-S. Han. (2014). Comparison of the osteogenic potential of titanium and modified zirconia based bioceramics, *Int. J. Mol. Sci. 15* 4442–4452

[24] M. Buciumeanu, D. Faria, J. Mesquita-Guimaraes, F.S. Silva. (2018). Tribological characterization of bioactive zirconia composite layers on zirconia structures, *Ceram. Int. 44* 18663–18671

[25] M. Dehestani, L. Ilver, E. Adolfsson. (2012). Enhancing the bioactivity of zirconia and zirconia composites by surface modification, *J. Biomed. Mater. Res. Part B. 100B* 832–840

[26] Nishiyabu, K. (2012). Powder space holder metal injection molding (PSH-MIM) of micro-porous metals. *Handbook of Metal Injection Molding*, 349–390

[27] Sahoo, P., Das, S. K., & Paulo Davim, J. (2019). Tribology of materials for biomedical applications. *Mechanical Behaviour of Biomaterials*, 1–45.

[28] Melo-Fonseca, F., Lima, R., Costa, M., Bartolomeu, F., Alves, N., Miranda, A., Gasik, M., Silva, F., Silva, N., & Miranda, G. (2018). 45S5 BAG-Ti6Al4V structures: The influence of the design on some of the physical and chemical interactions that drive cellular response. *Materials & Design*, *160*, 95–105.

[29] Gräf S, Müller FA. (2014). CO2-laser-assisted surface modification of titanium alloys for biomedical applications. *J Ceram Sci Technol 5:* 281–286.

[30] McKeever DC. The classic (1960). Tibial plateau prosthesis. *Clin Orthop Rel Res 1985*;192:3–12.

[31] Carr, B. C., & Goswami, T. (2009). Knee implants – Review of models and biomechanics. *Materials & Design*, *30*(2), 398–413.

[32] Sadegh, A., & Worek, W. (2017). Marks' Standard Handbook for Mechanical Engineers, 12th Edition (12th ed.). *McGraw Hill*.

[33] A. Aherwar, A. K Singh, A. Patnaik. (2015). Current and future biocompatibility aspects of biomaterials for hip prosthesis, *AIMS Bioeng*. 3 23 43.

[34] D. Faria, J.M. Pires, A.R. Boccaccini, O. Carvalho, F.S. Silva, J. Mesquita-Guimaraes. (2019). Development of novel zirconia implant's materials gradated design with improved bioactive surface, *J. Mech. Behav. Biomed. Mater. 94* 110–125.

[35] Stein, H. L. (1998). Ultrahigh molecular weight polyethylenes (uhmwpe). *Engineered Materials Handbook, 2,* 167–171.

[36] Freeman, M. A. R., Samuelson, K. M., Elias, S. G., Mariorenzi, L. J., Gokcay, E. I., & Tuke, M. (1989). *The patellofemoral joint in total knee prostheses. The Journal of Arthroplasty, 4,* S69–S74.

[37] Hurson, C., Kashir, A., Flavin, R., & Kelly, I. (2009). *Routine patellar resurfacing using an inset patellar technique. International Orthopaedics, 34(7),* 955–958.

[38] Fraser JF, Spangehl MJ. (2017). International rates of patellar resurfacing in primary total knee arthroplasty, 2004-2014. *J Arthroplasty 32*:83–6.

[39] Swan JD, Stoney JD, Lim K, Dowsey MM, Choong PFM. (2010). The need for patellar resurfacing 227 in total knee arthroplasty:a literature review. *ANZ J Surg*: 80:223–33.

[40] Molfetta, L., Casabella, A., & Palermo, A. (2021). The Patellar Resurfacing in Total Knee Prosthesis: Indications for Bone Stock and Patellar Morphology. *Frontiers in Medicine*, *7*.

[41] Robinson RP. 2005. The early innovators of today's resurfacing condylar knees. *J Arthrop, 20(Suppl. 1)*:2–26.

[42] Fixed or mobile-bearing total knee arthroplasty. Huang CH, Liau JJ, Cheng CK. *J Orthop Surg Res. 2007 Jan 5; 2():1.*

[43] Callaghan JJ, Insall JN, Greenwald AS, Dennis DA, Komistek RD, Murray DW, Bourne RB, Rorabeck CH, Dorr LD. (2001). Mobile-bearing knee replacement: concepts and results. *Instr Course Lect.50:*431-49.

[44] Urwin SG, Kader DF, Caplan N, St Clair Gibson A, Stewart S. (2014). Gait analysis of fixed bearing and mobile bearing total knee prostheses during walking: do mobile bearings offer functional advantages? *Knee. Mar; 21(2):*391-5.

[45] Okamoto N, Nakamura E, Nishioka H, Karasugi T, Okada T, Mizuta H. (2014 Dec). In vivo kinematic comparison between mobile-bearing and fixed-bearing total knee arthroplasty during step-up activity. *J Arthroplasty.; 29(12):2393-6.*

[46] InformedHealth.org. Cologne, Germany: Institute for Quality and Efficiency in Health Care (IQWiG); 2006. «https://www.ncbi.nlm.nih.gov/books/NBK65083/»

[47] Callaghan, J. J. and Liu, S. S. (2010) Cementless tibial fixation in TKA: not a second coming. Orthopedics, 33, 655.

[48] Price, A. J., Alvand, A., Troelsen, A., Katz, J. N., Hooper, G., Gray, A., Beard, D. (2018). *Knee replacement. The Lancet, 392(10158),* 1672–1682.

[49] 18th annual report 2020. National Joint Registry for England, Wales, Northern Ireland and the Isle of Man: surgical data to 31 December 2019. https://www.njrcentre.org.uk/. Accessed 2/01/2022.

[50] Annual report 2020-The Swedish Knee Arthroplasty Register. Accessed 2/01/2022.

[51] American Joint Registry 2020 annual report. Accessed 2/01/2022.

[52] Kalore, N. V., Gioe, T. J., & Singh, J. A. (2011). Diagnosis and Management of Infected Total Knee Arthroplasty§. *The Open Orthopaedics Journal*, *5* (1), 86–91.

[53] Canton, G., Ratti, C., Fattori, R., Hoxhaj, B., & Murena, L. (2017). Periprosthetic knee fractures. A review of epidemiology, risk factors, diagnosis, management and outcome. *Acta Biomed.*, *8* (2), 118–128.

[54] Cheuy, V. A., Foran, J. R. H., Paxton, R. J., Bade, M. J., Zeni, J. A., & Stevens-Lapsley, J. E. (2017, February 14). Arthrofibrosis Associated With Total Knee Arthroplasty. *J Arthroplasty*, *32* (8), 2604–2611.

[55] A. Aherwar, A. K Singh, A. Patnaik. (2015). Current and future biocompatibility aspects of biomaterials for hip prosthesis, *AIMS Bioeng. 3* 23–43.

[56] Postler, Anne; Lützner, Cornelia; Beyer, Franziska; Tille, Eric; Lützner, Jörg (2018). Analysis of Total Knee Arthroplasty revision causes. *BMC Musculoskeletal Disorders, 19(1), 55–.*

[57] Trampuz, A., Osmon, D. R., Hanssen, A. D., Steckelberg, J. M., & Patel, R. (2003). Molecular and Antibiofilm Approaches to Prosthetic Joint Infection. *Clinical Orthopaedics and Related Research*, *414*, 69–88.

[58] Fehring, T. K., Odum, S., Griffin, W. L., Mason, J. B., & Nadaud, M. (2001). *Early Failures in Total Knee Arthroplasty. Clinical Orthopaedics and Related Research, 392, 315–318.*

[59] Abu-Amer, Y., Darwech, I., & Clohisy, J. C. (2007). *Aseptic loosening of total joint replacements: mechanisms underlying osteolysis and potential therapies. Arthritis Research & Therapy, 9(Suppl 1), S6.*

[60] Zhang, Q. H., Cossey, A., & Tong, J. (2016). Stress shielding in periprosthetic bone following a total knee replacement: Effects of implant material, design and alignment. *Medical Engineering & Physics*, *38*(12), 1481–1488.

[61] Koh, C. K., Zeng, I., Ravi, S., Zhu, M., Vince, K. G., & Young, S. W. (2017). Periprosthetic Joint Infection Is the Main Cause of Failure for Modern Knee Arthroplasty: An Analysis of 11,134 Knees. *Clinical Orthopaedics and Related Research®, 475(9),* 2194–2201.

[62] Petersen, W., Rembitzki, I. V., Brüggemann, G.-P., Ellermann, A., Best, R., Koppenburg, A. G.-, & Liebau, C. (2013). Anterior knee pain after total knee arthroplasty: a narrative review*. International Orthopaedics, 38(2),* 319–328.

[63] Jibri, Z., Jamieson, P., Rakhra, K. S., Sampaio, M. L., & Dervin, G. (2019). Patellar maltracking: an update on the diagnosis and treatment strategies. *Insights into Imaging, 10(1).*

[64] Lin F, Wilson NA, Makhsous M, Press JM, Koh JL, Nuber GW, Zhang LQ. (2010). In vivo patellar tracking induced by individual quadriceps components in individuals with patellofemoral pain. *J Biomech.* ;43(2):235–241.

[65] Putman, S., Boureau, F., Girard, J., Migaud, H., & Pasquier, G. (2019). Patellar complications after total knee arthroplasty. *Orthopaedics & Traumatology: Surgery & Research*, *105*(1), S43–S51.

[66] E.P.Sue. (2018). Instability after TKA: Wobble & Buckle. *Orthopaedic Proceedings Vol. 97-B.*

[67] A. S. da S. Mello, P. L. dos Santos, A. Marquesi, T. P. Queiroz, R. Margonar, A. P. de S. Faloni. (2016). Some aspects of bone remodeling around dental implants, *Revista Clínica de Periodoncia, Implantología y Rehabilitación Oral*, pp. 1–9,

[68] Onuki, Y., Bhardwaj, U., Papadimitrakopoulos, F., Burgess, D.J. (2008). A review of biocompatibility of implantable devices: Current challenges to overcome foreign body response. *J. Diab. Sci. Technol.* 2(6), 1003–1015

[69] Williams, D. (2008). On the mechanisms of biocompatibility. *Biomaterials 29*, 2941–2953

[70] Tagaya, M., Ikoma, T., Hanagata, N., & Tanaka, J. (2012). Analytical Investigation of Protein Mediation Between Biomaterials and Cells. *Materials Express*, *2*(1), 1–22.

[71] Rodrigues, L.R. (2011). Inhibition of bacterial adhesion on medical devices. In: Linke, D., Goldman, A. (eds.) *Bacterial Adhesion: Biology, Chemistry, and Physics*, *Series: Advances in Experimental Medicine and Biology*, vol. 715, pp. 351–367. Springer, Germany

[72] S. Morelli and A. Piscioneri. (2002). Cell-material Interactions. *Biomaterials for Stem Cell Therapy: State of Art and Vision for the Future*, pp. 153–180.

[73] P. J. Marie, E. Haÿ, and Z. Saidak. (2014). Integrin and cadherin signaling in bone: Role and potential therapeutic targets. *Trends in Endocrinology and Metabolism*, vol. 25, no. 11, pp. 567–575.

[74] Garcia, A.: Get a grip: integrins in cell-biomaterial interactions. (2005). *Biomaterials* 26(36), 7525–7529.

[75] Siebers, M., Brugge, P., Walboomers, X., Jansen, J. (2005). Integrins as linker proteins between osteoblasts and bone replacing materials. A Crit. Rev. *Biomater*. 26(2), 137–146.

[76] Eisenbarth, E., Meyle, J., Nachtigall, W., Breme, J. (1996). Influence of the surface structure of titanium materials on the adhesion of fibroblasts. *Biomaterials* 17, 1399–1403

[77] Hoerstrup, S.P., Sodian, R., Daebritz, S., Wang, J., Bacha, E.A., Martin, D.P., Moran, A.M., Guleserian, K.J., Sperling, J.S., Kaushal, S., Vacanti, J.P., Schoen, F.J., Mayer Jr, J.E. (2000). Functional living trileaflet heart valves grown in vitro. *Circulation* 102, 44–49 .

[78] Patel, N.R., Gohil, P.P. (2012). A review on biomaterials: scope, applications and human anatomy significance. *Int. J. Emerg. Technol. Adv. Eng. 2*, 91–101.

[79] Anselme, K., Ponche, A., Bigerekke, M. (2010). Relative influence of surface topography and surface chemistry on cell response to bone implant materials. Part 2: biological aspects. *Proc. Inst. Mech. Eng H: J. Eng. Med. 224*, 1487–1507.

[80] Chang, H.I., Wang, Y. (2011). Cell responses to surface and architecture of tissue engineering scaffolds. In: Eberli D (ed.) *Cells and Biomaterials*, Chap 27, InTech, Croatia.

[81] Ballet, T.L.B., Brechet, Y., Bruckert, F., Weidenhaupt, M. (2010). Protein conformational changes induced by adsorption onto material surfaces: an important issue for biomedical applications of material science. *Bull. Pol. Acad. Sci. 58*, 303–315.

[82] Tang, L., Thevenot, P., & Hu, W. (2008). Surface Chemistry Influences Implant Biocompatibility. *Current Topics in Medicinal Chemistry*, *8* (4), 270–280.

[83] Evans-Nguyen KM, Tolles LR, Gorkun OV, Lord ST, Schoenfisch MH. (2005). Interactions of thrombin with fibrinogen adsorbed on methyl-, hydroxyl-, amine-, and carboxyl-terminated self-assembled monolayers. *Biochemistry.* 44(47):15561–15568.

[84] Zreiqat, H., Valenzuela, S. M., Nissan, B. B., Roest, R., Knabe, C., Radlanski, R. J., Renz, H., & Evans, P. J. (2005). The effect of surface chemistry modification of titanium alloy on signalling pathways in human osteoblasts. *Biomaterials*, *26*(36), 7579–7586.

[85] Keselowsky, Benjamin G., David M. Collard, and Andrés J. García. (2003). Surface chemistry modulates fibronectin conformation and directs integrin binding and specificity to control cell adhesion. *Journal of Biomedical Materials Research Part A: An Official Journal of The Society for Biomaterials, The Japanese Society for Biomaterials, and The Australian Society for Biomaterials and the Korean Society for Biomaterials* 66.2, 247-259.

[86] Tran, R., Xu, Z., Radhakrishnan, B. *et al.* (2016). Surface energies of elemental crystals. *Sci Data* **3**, 160080.

[87] Michiardi, A., Aparicio, C., Ratner, B. D., Planell, J. A., & Gil, J. (2007). The influence of surface energy on competitive protein adsorption on oxidized NiTi surfaces. *Biomaterials*, *28*(4), 586–594.

[88] Hallab, N. J., Bundy, K. J., O'Connor, K., Moses, R. L., & Jacobs, J. J. (2001). Evaluation of Metallic and Polymeric Biomaterial Surface Energy and Surface Roughness Characteristics for Directed Cell Adhesion. *Tissue Engineering*, *7*(1), 55–71.

[89] Riveiro, A., Maçon, A. L. B., del Val, J., Comesaña, R., & Pou, J. (2018). Laser Surface Texturing of Polymers for Biomedical Applications. *Frontiers in Physics*, *6*.

[90] Majhy, B., Priyadarshini, P., & Sen, A. K. (2021). Effect of surface energy and roughness on cell adhesion and growth – facile surface modification for enhanced cell culture. *RSC Advances*, *11*(25), 15467–15476.

[91] B. S. Kopf, S. Ruch, S. Berner, N. D. Spencer, K. Maniura-Weber. (2015). The role of nanostructures and hydrophilicity in osseointegration: In-vitro protein-adsorption and blood-interaction studies. *Journal of Biomedical Materials Research - Part A*, vol. 103, no. 8, pp. 2661–2672.

[92] Y. Liu, X. Zhang, P. Hao. (2016). The effect of topography and wettability of biomaterials on platelet adhesion. *Journal of Adhesion Science and Technology*, vol. 30, no. 8, pp. 878–893.

[93] Xu, L. C., & Siedlecki, C. A. (2007). Effects of surface wettability and contact time on protein adhesion to biomaterial surfaces. *Biomaterials*, *28*(22), 3273–3283.

[94] Tamada Y, Ikada Y. (1986). Cell attachment to various polymer surfaces. In: Chiellini E, Giusti P, Migliaresi C, Nicolais L, editors. *Polymers in medicine II. New York: Plenum Press*; p. 101–15.

[95] Lim, J. Y., Shaughnessy, M. C., Zhou, Z., Noh, H., Vogler, E. A., & Donahue, H. J. (2008). Surface energy effects on osteoblast spatial growth and mineralization. *Biomaterials*, *29*(12), 1776–1784.

[96] R. A. Gittens et al. (2014). A review on the wettability of dental implant surfaces II: Biological and clinical aspects. *Acta Biomaterialia*, vol. 10, no. 7, pp. 2907–2918,

[97] Flink, S., Veggel, F. C. J. M. V., & Reinhoudt, D. N. (2000). Sensor Functionalities in Self-Assembled Monolayers. *Advanced Materials*, *12*(18), 1315–1328.

[98] Ulman, A. (1996). Formation and Structure of Self-Assembled Monolayers. *Chemical Reviews*, *96*(4), 1533–1554.

[99] Liu, X., Ye, Q., Yu, B., Liang, Y., Liu, W., & Zhou, F. (2010). Switching Water Droplet Adhesion Using Responsive Polymer Brushes. *Langmuir*, *26*(14), 12377–12382.

[100] Martin, T. A., Caliari, S. R., Williford, P. D., Harley, B. A., & Bailey, R. C. (2011). The generation of biomolecular patterns in highly porous collagen-GAG scaffolds using direct photolithography. *Biomaterials*, *32*(16), 3949–3957.

[101] Zareidoost, A., Yousefpour, M., Ghaseme, B., & Amanzadeh, A. (2012). The relationship of surface roughness and cell response of chemical surface modification of titanium. *Journal of Materials Science: Materials in Medicine*, *23*(6), 1479–1488.

[102] Deligianni, D. D., Katsala, N. D., Koutsoukos, P. G., & Missirlis, Y. F. (2000). Effect of surface roughness of hydroxyapatite on human bone marrow cell adhesion, proliferation, differentiation and detachment strength. *Biomaterials*, *22*(1), 87–96.

[103] Tong, C., & Derek, C. (2022). Membrane surface roughness promotes rapid initial cell adhesion and long term microalgal biofilm stability. *Environmental Research*, *206*, 112602.

[104] le Guehennec, L., Lopez-Heredia, M. A., Enkel, B., Weiss, P., Amouriq, Y., & Layrolle, P. (2008). Osteoblastic cell behaviour on different titanium implant surfaces. *Acta Biomaterialia*, *4*(3), 535–543.

[105] S. Morelli and A. Piscioneri, (2002). Cell-material Interactions. *Biomaterials for Stem Cell Therapy: State of Art and Vision for the Future*, pp. 153–180.

[106] Mesquita-Guimarães, J., Detsch, R., Souza, A., Henriques, B., Silva, F., Boccaccini, A., & Carvalho, O. (2020). Cell adhesion evaluation of laser-sintered HAp and 45S5 bioactive glass coatings on micro-textured zirconia surfaces using MC3T3-E1 osteoblast-like cells. *Materials Science and Engineering: C*, *109*, 110492.

[107] Sanyal, M. K., Datta, A., & Hazra, S. (2002). Morphology of nanostructured materials. *Pure and Applied Chemistry*, *74*(9), 1553–1570.

[108] B. Zhu, Q. Zhang, Q. Lu, Y. Xu, J. Yin, J. Hu and Z. Wang, Biomaterials 25. (2004). 4215.

[109] M. J. Dalby, N. Gadegaard, M. O. Riehle, C. D. Wilkinson and A. S. Curtis. *Int J. Biochem. Cell. Biol. 36.* (2004).

[110] Divya Rani, V., Vinoth-Kumar, L., Anitha, V., Manzoor, K., Deepthy, M., & Shantikumar, V. N. (2012). Osteointegration of titanium implant is sensitive to specific nanostructure morphology. *Acta Biomaterialia*, *8*(5), 1976–1989.

[111] Biggs, M. J. P., Richards, R. G., Gadegaard, N., Wilkinson, C. D. W., & Dalby, M. J. (2007). The effects of nanoscale pits on primary human osteoblast adhesion formation and cellular spreading. *Journal of Materials Science: Materials in Medicine*, *18*(2), 399–404.

[112] Lin, L., Wang, H., Ni, M., Rui, Y., Cheng, T. Y., Cheng, C. K., Pan, X., Li, G., & Lin, C. (2014). Enhanced osteointegration of medical titanium implant with surface modifications in micro/nanoscale structures. *Journal of Orthopaedic Translation*, *2*(1), 35–42.

[113] Leclech, C., & Villard, C. (2020). Cellular and Subcellular Contact Guidance on Microfabricated Substrates. *Frontiers in Bioengineering and Biotechnology*, *8*.

[114] Bettinger, C. J., Orrick, B., Misra, A., Langer, R., & Borenstein, J. T. (2006). Microfabrication of poly (glycerol–sebacate) for contact guidance applications. *Biomaterials*, *27*(12), 2558–2565.

[115] Ramirez-San Juan, G. R., P. W. Oakes, and M. L. Gardel. (2017). Contact guidance requires spatial control of leading-edge protrusion. *Molecular biology of the cell* 28.8: 1043-1053.

[116] G. Abagnale et al., (2015). Surface topography enhances differentiation of mesenchymal stem cells towards osteogenic and adipogenic lineages. *Biomaterials*, vol. 61, pp. 316–326,

[117] T. Albrektsson et al., (1983). The interface zone of inorganic implants In vivo: Titanium implants in bone. *Annals of Biomedical Engineering*, vol. 11, no. 1, pp. 1–27,

[118] M. Kulkarni, A. Mazare, P. Schmuki, A. Iglič. (2014). Biomaterial Surface Modification Of Titanium and Titanium Alloys for Medical Applications. In *Nanomedicine*, A. Seifalian, A. de Mel, and D. M. Kalaskar, Eds. One Central Press, pp. 111–136.

[119] J. Miranda-rius, E. Lahor-soler, L. Brunet-llobet, D. De Dios, F. X. Gil. (2016). Treatments to Optimize Dental Implant Surface Topography and Enhance Cell Bioactivity in *Dental Implantology and Biomaterial*, D. M. Almasri, Ed. InTech, pp. 109–127.

[120] E. Ahmed, L. D. Hyun, W. W. CW, C. S. Choon. (2015). The Survival Rate of RBM Surface versus SLA Surface in Geometrically Identical Implant Design, Journal of Oral Biology, vol. 2, no. 1, pp. 1–8.

[121] E. Tranquillo, F. Bollino, Coatings, 2020, 10(6), 589.

[122] C. Aparicio, F. Javier Gil, C. Fonseca, M. Barbosa, and J. A. Planell. (2003). Corrosion behaviour of commercially pure titanium shot blasted with different materials and sizes of shot particles for dental implant applications. *Biomaterials*, vol. 24, no. 2, pp. 263–273,

[123] Faria, D., Henriques, B., Souza, A., Silva, F., & Carvalho, O. (2020). Laser-assisted production of HAp-coated zirconia structured surfaces for biomedical applications. *Journal of the Mechanical Behavior of Biomedical Materials*, *112*, 104049.

[124] Faria, D., Abreu, C. S., Buciumeanu, M., Dourado, N., Carvalho, O., Silva, F. S., & Miranda, G. (2017). Ti6Al4V laser surface preparation and functionalization using hydroxyapatite for biomedical applications. *Journal of Biomedical Materials Research Part B: Applied Biomaterials*, *106*(4), 1534–1545.

[125] S. Mukherjee, S. Dhara, P. Saha. (2015). Enhancing the biocompatibility of Ti6Al4V implants by laser surface microtexturing: an in vitro study, Int. J. Adv. Manuf. Technol. 76 5–15.

[126] Faria, D., Madeira, S., Buciumeanu, M., Silva, F., & Carvalho, O. (2020). Novel laser textured surface designs for improved zirconia implants performance. *Materials Science and Engineering: C*, *108*, 110390.

[127] M. Kulkarni, A. Mazare, P. Schmuki, A. Iglič. (2014). Biomaterial Surface Modification Of Titanium and Titanium Alloys for Medical Applications. in *Nanomedicine*, A. Seifalian, A. de Mel, and D. M. Kalaskar, Eds. One Central Press, pp. 111–136.

[128] Guo, C., & Singh, S.C. (Eds.). (2021). Handbook of Laser Technology and Applications: Lasers: Principles and Operations (2nd ed.). CRC Press.

[129] Hitz, C. B., Ewing, J. J., & Hecht, J. (2012). *Introduction to Laser Technology*. Wiley.

[130] Duval, S. (2022, September 12). *Laser processing of polymer in the mid-infrared - Why ?* Femtum. https://femtum.com/laser-processing-of-polymer-in-the-mid-infrared/

[131] Sugioka, K., Meunier, M., & Piqué, A. (Eds.). (2010). Laser Precision Microfabrication. *Springer Series in Materials Science*.

[132] J. D. Majumdar, I. Manna. (2013). Laser-Assisted Fabrication of Materials, vol. 161. *Springer-Verlag Berlin Heidelberg*.

[133] A. Kurella, N. B. Dahotre (2005). Surface Modification for Bioimplants: The Role of Laser Surface Engineering. *Journal of Biomaterials Applications*, vol. 20, no. 5, pp. 5–50.

[134] Choi, B.; Welch, A. J. (2001-01-01). "Analysis of thermal relaxation during laser irradiation of tissue". *Lasers in Surgery and Medicine*. 29 (4): 351–359.

[135] Moura, C., Pereira, R., Buciumeanu, M., Carvalho, O., Bartolomeu, F., Nascimento, R., & Silva, F. (2017). Effect of laser surface texturing on primary stability and surface properties of zirconia implants. *Ceramics International*, *43*(17), 15227–15236.

[136] A. Cunha et al., (2016). Femtosecond laser surface texturing of titanium as a method to reduce the adhesion of Staphylococcus aureus and biofilm formation. *Applied Surface Science*, vol. 360, pp. 485–493.

[137] B. Su, S. Dhara, L. Wang. (2008). Green ceramic machining: a top-down approach for the rapid fabrication of complex-shaped ceramics, J. Eur. Ceram. Soc. 28 2109–2115.

[138] Costa, M., Miranda, A., Bartolomeu, F., Carvalho, O., Matos, S., Miranda, G., & Silva, F. (2022). NiTi laser textured implants with improved in vivo osseointegration: An experimental study in rats. *Journal of Materials Science & Technology*, *114*, 120–130.

[139] C. Hallgren, H. Reimers, D. Chakarov, J. Gold, A. Wennerberg. (2003). An in vivo study of bone response to implants topographically modified by laser micromachining. *Biomaterials*, vol. 24, no. 5, pp. 701–710.

[140] Zhao, X. (2011). Introduction to bioactive materials in medicine. *Bioactive Materials in Medicine*, 1–13.

[141] D. F. Williams. The Williams Dictionary of Biomaterials. (1999). Liverpool, UK: Liverpool University Press.

[142] Julian R. Jones. Biomaterials, Artificial Organs and Tissue Engineering. (2005)

[143] Shepherd, J.H., Best S.M. (2011). Calcium phosphate scaffolds for bone repair. *JOM* 63, 83–92.

[144] Huang, J. (2017). Design and Development of Ceramics and Glasses. *Biology and Engineering of Stem Cell Niches*, 315–329.

[145] Torabinejad, M., Watson, T., & Pitt Ford, T. (1993). Sealing ability of a mineral trioxide aggregate when used as a root end filling material. *Journal of Endodontics*, *19*(12), 591–595.

[146] Ducheyne, P. (1999). Bioactive ceramics: the effect of surface reactivity on bone formation and bone cell function. *Biomaterials*, *20*(23–24), 2287–2303.

[147] Blokhuis, Taco J., et al. (2000). Properties of calcium phosphate ceramics in relation to their in vivo behavior. *Journal of trauma and acute care surgery* 48.1 179.

[148] Adzila, S., Murad, M., & Sopyan, I. (2012, January 1). Doping Metal into Calcium Phosphate Phase for Better Performance of Bone Implant Materials. *Recent Patents on Materials Science*, *5*(1), 18–47.

[149] Kohrs, N. J., Liyanage, T., Venkatesan, N., Najarzadeh, A., & Puleo, D. A. (2019). Drug Delivery Systems and Controlled Release. *Encyclopedia of Biomedical Engineering*, 316–329.

[150] Mitchell PJC, Pitt Ford TR, Torabinejad M, McDonald F (1999) Osteoblast biocompatibility of mineral trioxide. Biomaterials 20, 167–73.

[151] Zhu Q, Haglund R, Safavi KE, Spa ̊ngberg LS (2000) Adhesion of human osteoblasts on root end filling material. Journal of Endodontics 26, 404–6.

[152] De Deus, G., et al. (2005). Cytotoxicity of MTA and Portland cement on human ECV 304 endothelial cells. *International endodontic journal* 38.9 604-609.

[153] J.P. Kruth, G. Levy, F. Klocke, T.H.C. Childs. (2007). Consolidation phenomena in laser and powder-bed based layered manufacturing. *CIRP Ann. - Manuf. Technol*. 56 730–759.

[154] Schmitt D, Lee J, Bogen G. (2001). Multifaceted use of ProRoot™ MTA root canal repair material. *Pediatr Dent*. 23(4):326-330.

[155] Ginebra MP, Fernández E, De Maeyer EAP, Verbeeck RMH, Boltong MG, Ginebra J, Driessens FCM, Planell JA. (1997). Setting reaction and hardening of an apatitic calcium phosphate cement. *J Dent Res*, 76(4), 905–12.

[156] Y. Cho, J. Hong, H. Ryoo, D. Kim, J. Park, J. Han. (2015). Osteogenic responses to zirconia with hydroxyapatite coating by aerosol deposition, *J. Dent. Res*. 94 491–499.

[157] Somers, N., & Lasgorceix, M. (2021). Surface Treatment of Bioceramics. *Encyclopedia of Materials: Technical Ceramics and Glasses*, 701–715.

[158] Eliaz, N., & Metoki, N. (2017). Calcium Phosphate Bioceramics: A Review of Their History, Structure, Properties, Coating Technologies and Biomedical Applications. *Materials*, *10*(4), 334.

[159] A.P.M. Ferraris, E. Verné, P. Appendino, C. Moisescu, A. Krajewski, A. Ravaglioli. (2000). Coatings on zirconia for medical applications. *Biomaterials*. 21 765–773

[160] S. Lei, X. Yan-Feng, G. Lu, W. Yao, W. Fang, G. Zhong-Wei. (2012). The effect of antibacterial ingredients and coating microstructure on the antibacterial properties of plasma sprayed hydroxyapatite coatings, *Surf. Coatings Technol*. 206 2986–2990.

[161] Nguyen, N. T. (2012). Fabrication technologies. *Micromixers*, 113–161.

[162] Chen, X., Hu, Y., Xie, Z., Wang, H. (2018). Materials and Design of Photocatalytic Membranes. *Current Trends and Future Developments on (Bio-) Membranes*, pp.71-96.

[163] Paras and Kumar, A. (2022). Anti-Wetting Polymeric Coatings. *Encyclopedia of Materials: Plastics and Polymers*, pp.786-795.

[164] Butterfly, B. (2017, December 15). *AR Coating Technique: Thin Film Deposition*. FindLight Blog. https://www.findlight.net/blog/ar-coating-techniques/

[165] Konstanty, J. (2013). Applications of powder metallurgy to cutting tools. *Advances in Powder Metallurgy*, pp.555-585.

[166] Lu, L. and Ishiyama, O. (2015). Iron ore sintering. *Iron Ore*, pp.395-433.

[167] Gupta, N. and Basu, B. (2018). Hot pressing and spark plasma sintering techniques of intermetallic matrix composites. *Intermetallic Matrix Composites*, pp.243-302.

[168] Chang, J., Zhang, X. and Dai, K. (2020). Material characteristics, surface/interface, and biological effects on the osteogenesis of bioactive materials. *Bioactive Materials for Bone Regeneration*, pp.1-103.

[169] Barsoum, Michel. (2019). Fundamentals of ceramics. *CRC press*.

[170] Kruth JP, Wang X, Laoui T, Froyen L. (2003). Lasers and materials in selective laser sintering. *Assem Autom* 23:357–371.

[171] Patel, C. K. N. (1964, November 30). Continuous-Wave Laser Action on Vibrational-Rotational Transitions. *Physical Review Journals Archive*. Retrieved September 9, 2022, from https://journals.aps.org/pr/abstract/10.1103/PhysRev.136.A1187

[172] Ghazali, M., Shaifudin, M., Abdullah, W., Kamaruzzaman, W., Fekeri, M., Zulkifli, M. (2018). Conventional Sintering Effects on the Microstructure and Electrical Characteristics of Low-Voltage Ceramic Varistor. *Sintering Technology - Method and Application*.

[173] Chang, J., Zhang, X., Dai, K. (2020). Material characteristics, surface/interface, and biological effects on the osteogenesis of bioactive materials. *Bioactive Materials for Bone Regeneration*, pp.1-103.

[174] Parada, S. A., Dilisio, M. F., & Kennedy, C. D. (2014). Management of complications after rotator cuff surgery. *Current Reviews in Musculoskeletal Medicine*, *8*(1), 40–52.

[175] Fuchs, F. (2015). Ultrasonic cleaning and washing of surfaces. *Power Ultrasonics*, 577–609.

[176] McMullan, D. (2006). "Scanning electron microscopy 1928–1965". *Scanning*. 17: 175-185.

[177] Ebnesajjad, S. (2014). Surface and Material Characterization Techniques. *Surface Treatment of Materials for Adhesive Bonding*, 39–75.

[178] Mahltig, B. (2016). Smart hydrophobic and soil-repellent protective composite coatings for textiles and leather. *Smart Composite Coatings and Membranes*, 261–292.

[179] D. Quéré (2008). Wetting and Roughness. *Annual Review of Materials Research*, vol. 38, no. 1, pp. 71–99.

[180] V.G. Pina, A. Dalmau, F. Devesa, V. Amigo, A.I. Munoz. (n.d). Tribocorrosion behavior of beta titanium biomedical alloys in phosphate buffer saline solution, *J. Mech. Behav*.

[181] T. Min (2012). Design and Fabrication of Super-Hydrophobic Surfaces by Laser Micro/Nano-Processing. National University of Singapore.

[182] Enamur, R. L., Sen, D., & Kabir, M. R. (2016). Effect of Water to Cement Ratio and Age on Portland Composite Cement Mortar Porosity, Strength and Evaporation Rate. *American Journal of Engineering Research (AJER)*, *5*(8), 120–127.

[183] Pakravan, H., Jamshidi, M., & Latifi, M. (2014, July). Relationship between the surface free energy of hardened cement paste and chemical phase composition. *Journal of Industrial and Engineering Chemistry*, *20*(4), 1737–1740.

[184] Katano, Y., Nakano, K., Otsuki, M., & Matsukawa, H. (2014). Novel Friction Law for the Static Friction Force based on Local Precursor Slipping. *Scientific Reports*, *4*(1).

[185] N. B. Dahotre, S. R. Paital, A. N. Samant, C. Daniel. (2010). Wetting behaviour of laser synthetic surface microtextures on Ti-6Al-4V for bioapplication. *Philosophical Transactions of the Royal Society A: Mathematical, Physical and Engineering Sciences*, vol. 368, no. 1917, pp. 1863–1889.

[186] J. Weng, X. Liu, X. Zhang, X. Ji, J. Mater. Sci. Lett. 1994, 13, 159.

[187] Quilitz, M., Steingröver, K., & Veith, M. (2009, September 19). Effect of the Ca/P ratio on the dielectric properties of nanoscaled substoichiometric hydroxyapatite. *Journal of Materials Science: Materials in Medicine*, *21*(2), 399–405.

[188] Zahn, D., & Hochrein, O. (2003). Computational study of interfaces between hydroxyapatite and water. *Physical Chemistry Chemical Physics*, *5*(18), 4004.

Appendix A

This appendix presents some of the previously introduced zirconia-related figures in a larger scale, for better interpretation and analysis of the obtained results. Therefore, zirconia textured samples obtained through laser texturing are presented in figure a) (L16Pn) and b) (D20PnVm). Figure c) presents the obtained friction tests for all tested conditions.

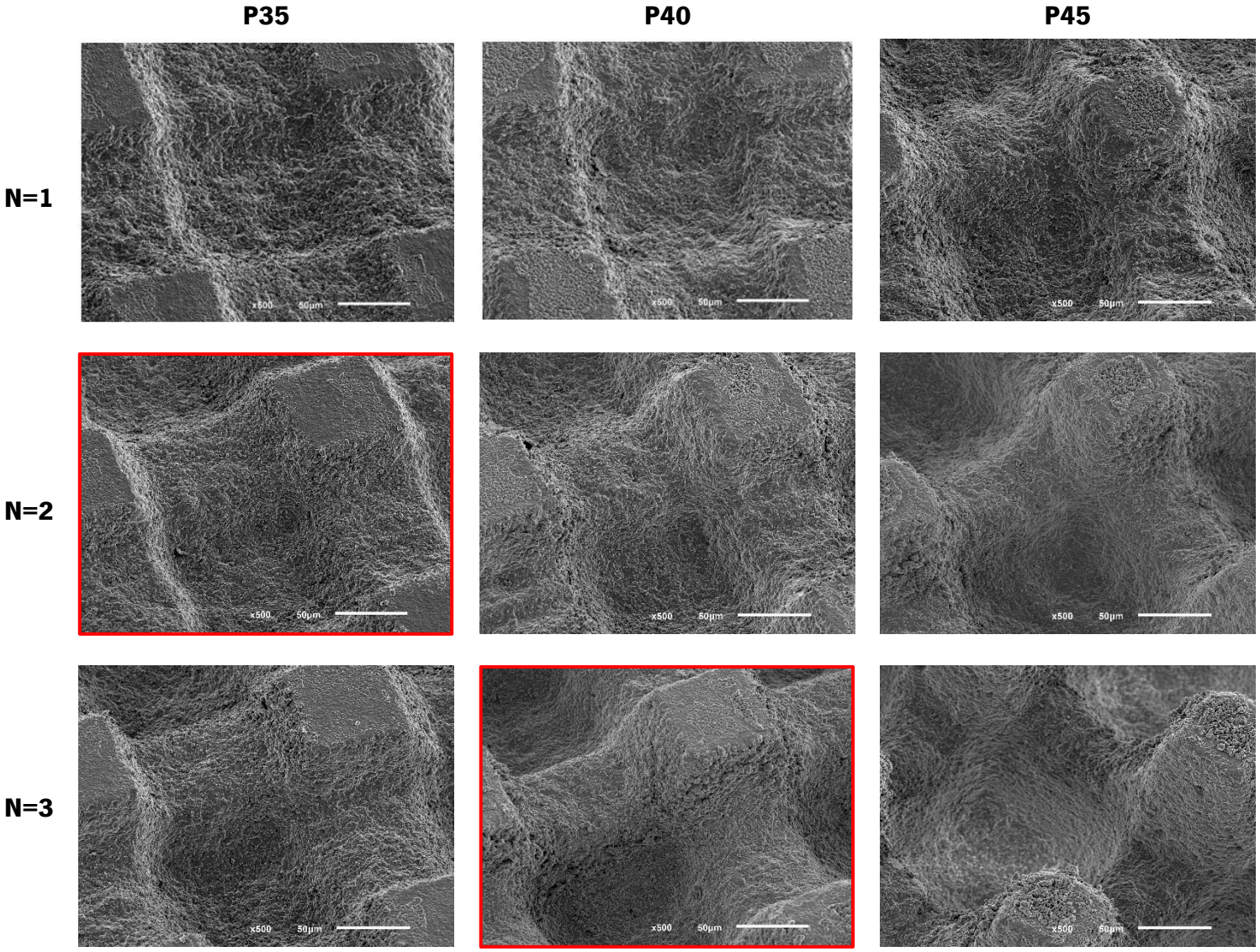

a)

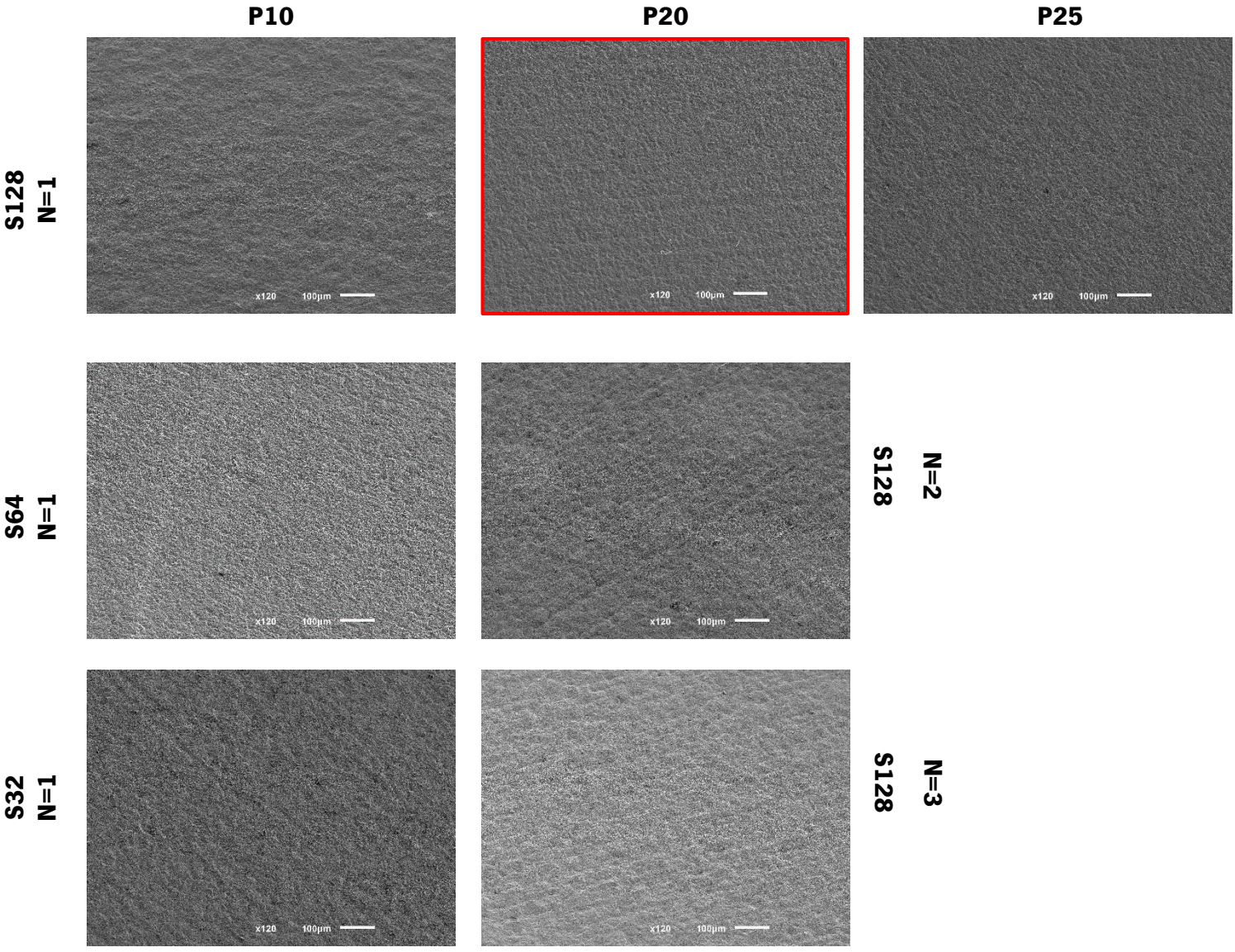

b)

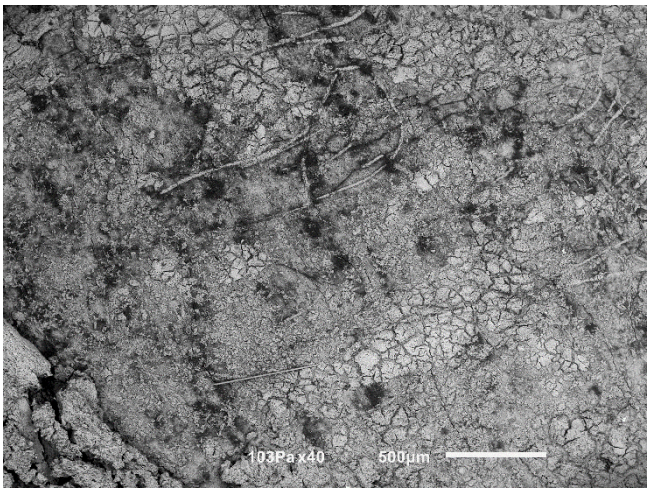
103Pa x40
500µm

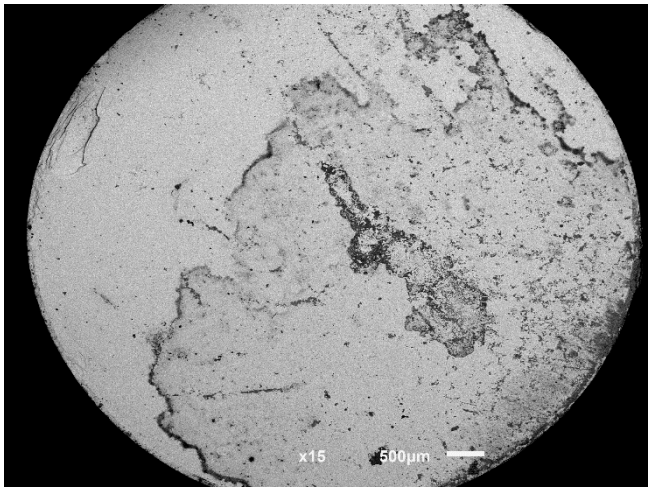
x15
500µm

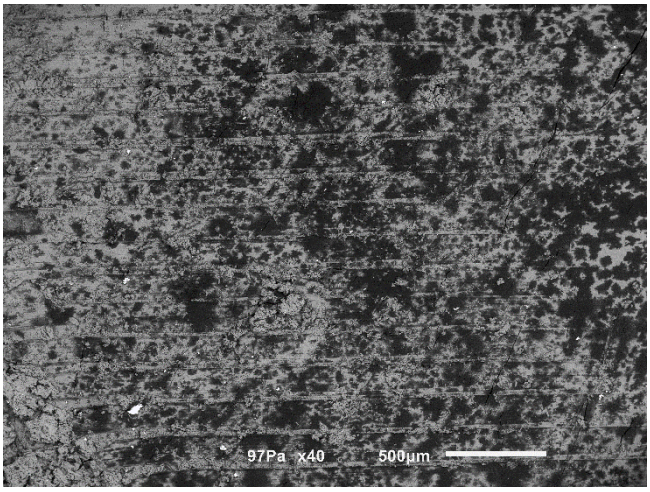
97Pa x40
500µm

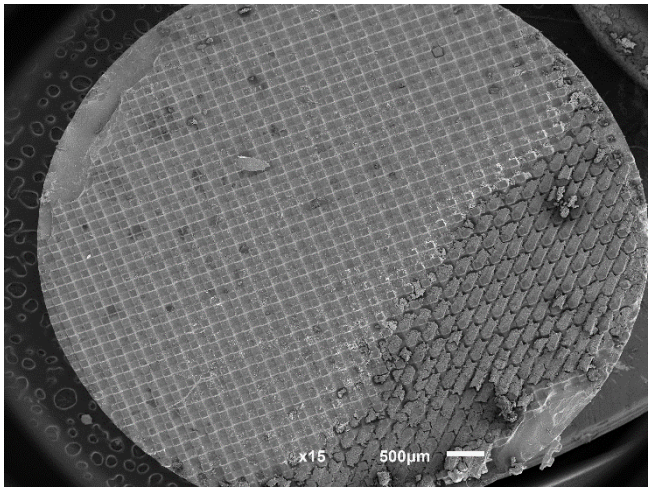
x15
500µm

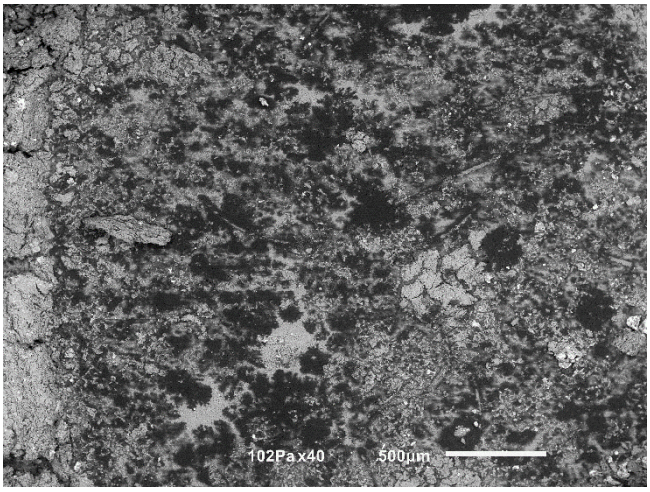
102Pa x40
500µm

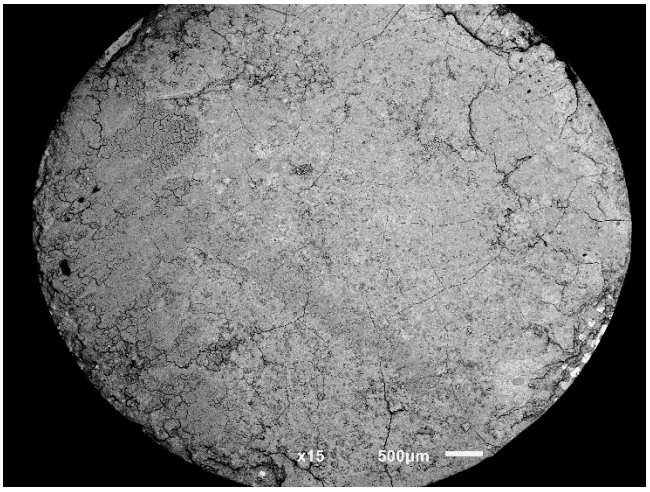
x15
500µm

c)

Appendix B

This appendix presents some of the previously introduced titanium-related figures in a larger scale, for better interpretation and analysis of the obtained results. Therefore, Hap coated samples obtained through laser sintering are presented in figure a) (0.8mm) and b) (0.25mm), while coated samples obtained through conventional sintering are presented in figure c) (0.8mm and (0.25mm). Figure d1), d2) and d3) presents the obtained friction tests for all tested conditions.

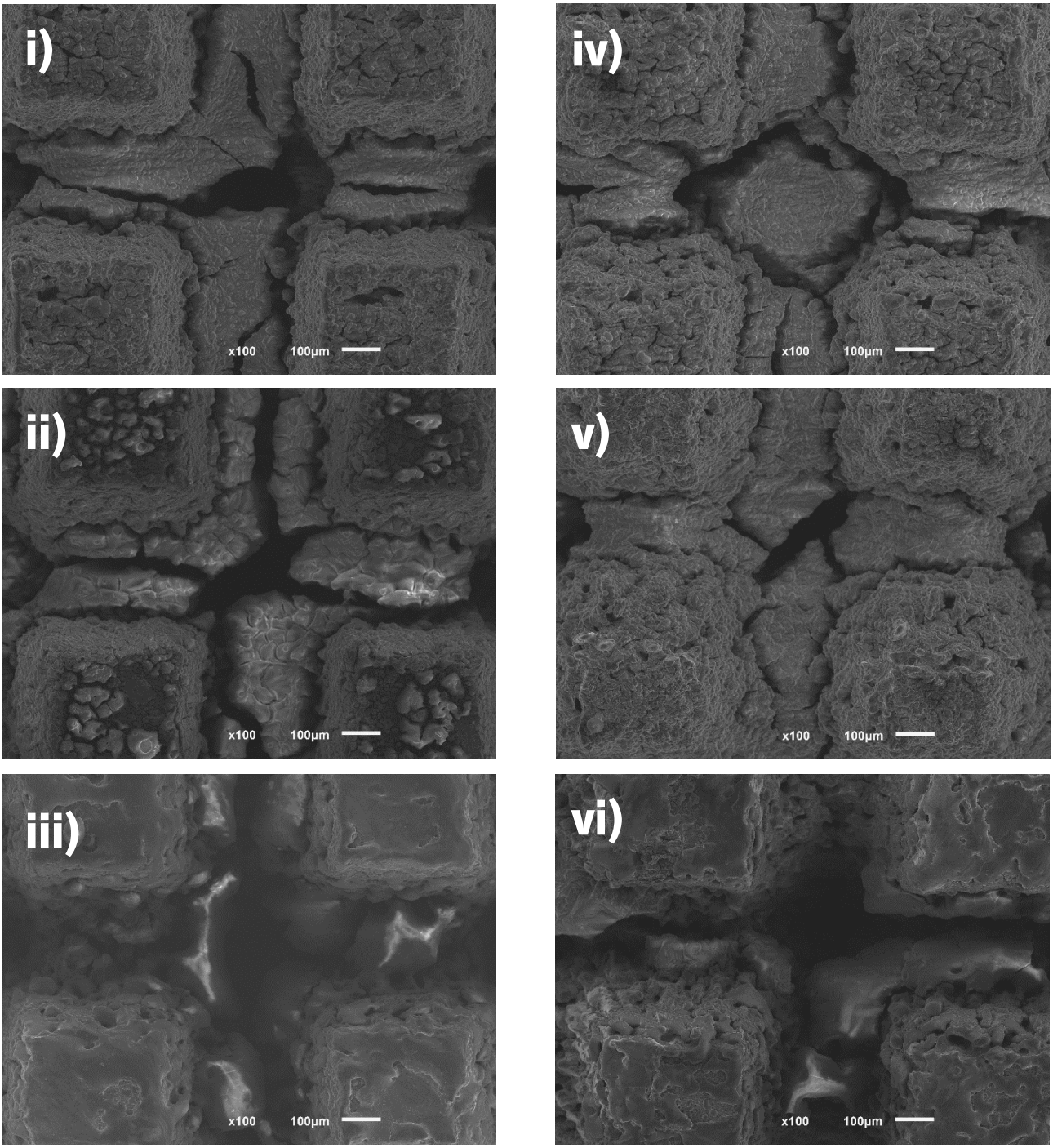

a)

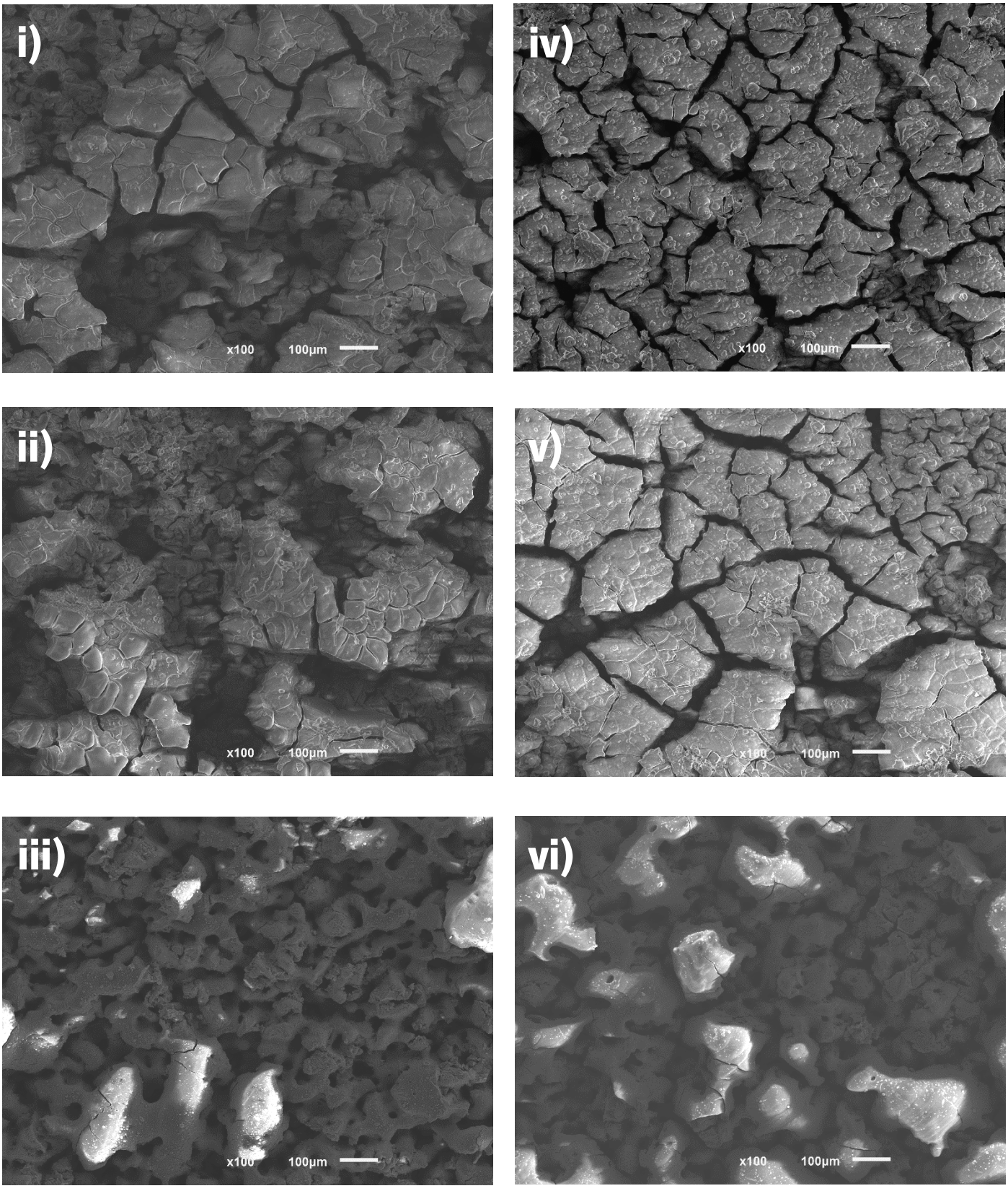
i)
x100
100µm
iv)
x100
100µm
ii)
x100
100µm
v)
x100
100µm
iii)
x100
100µm
vi)
x100
100µm

b)

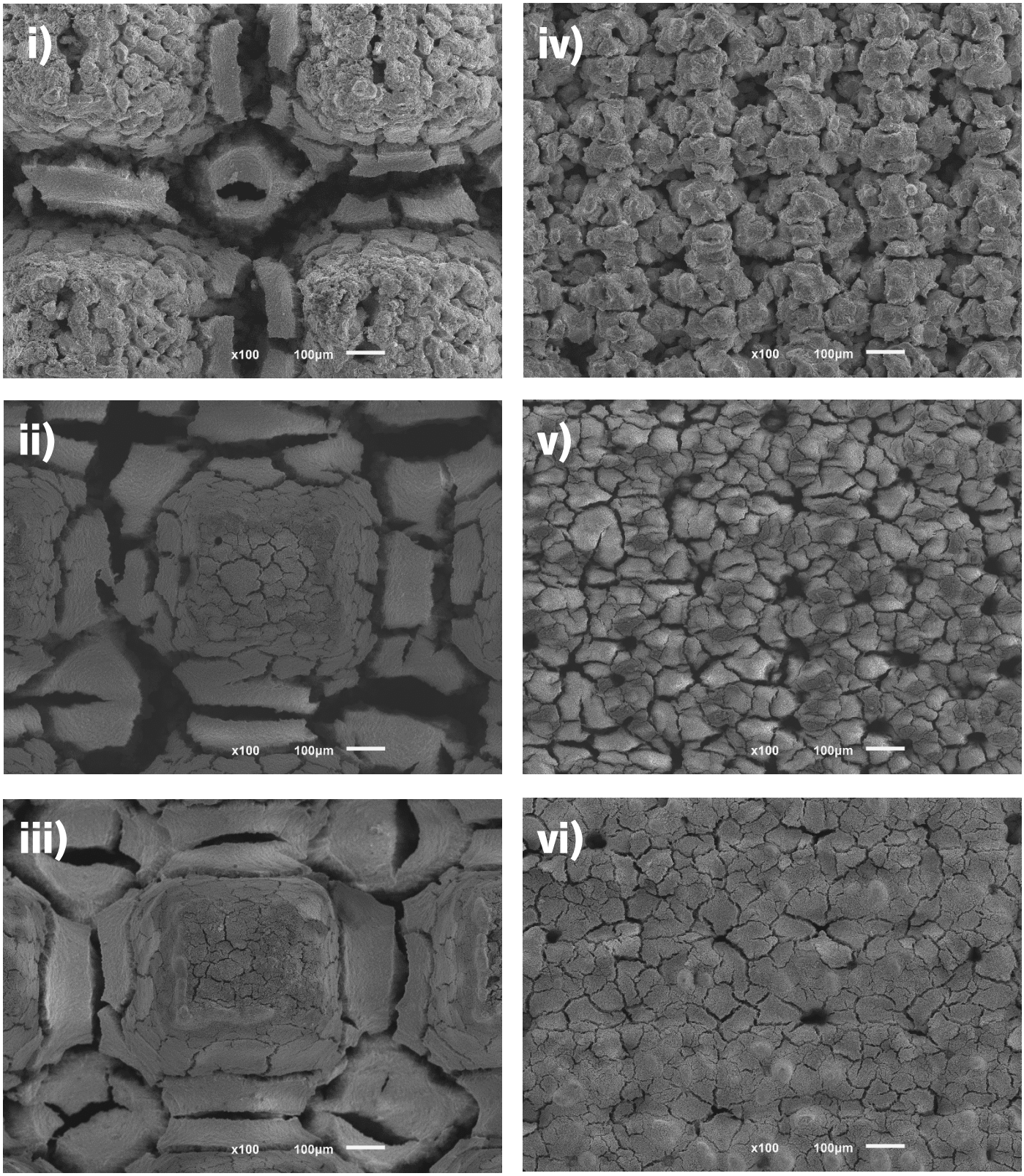
i)
x100 100µm
iv)
x100 100µm
ii)
x100 100µm
v)
x100 100µm
iii)
x100 100µm
vi)
x100 100µm

c)

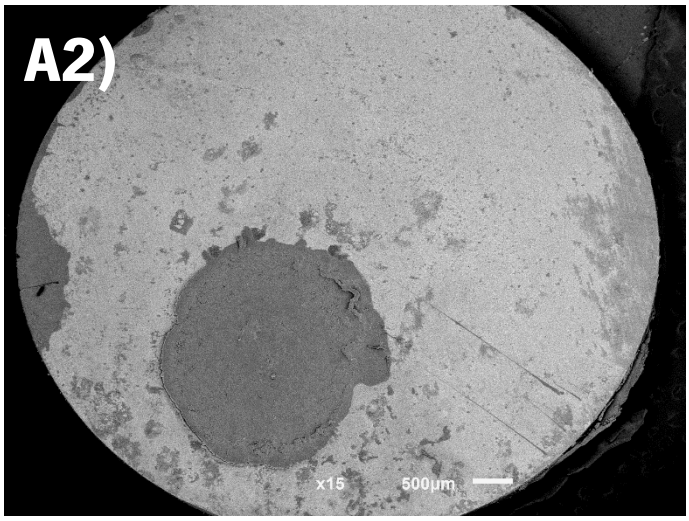
A2)
x15
500µm

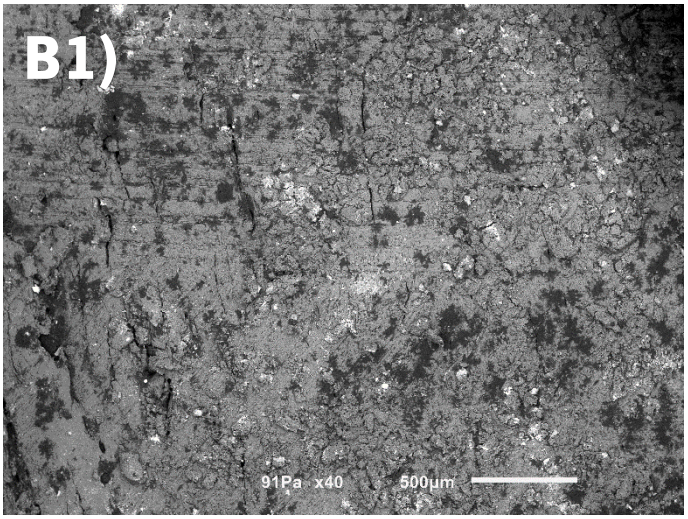
B1)
91Pa x40
500µm

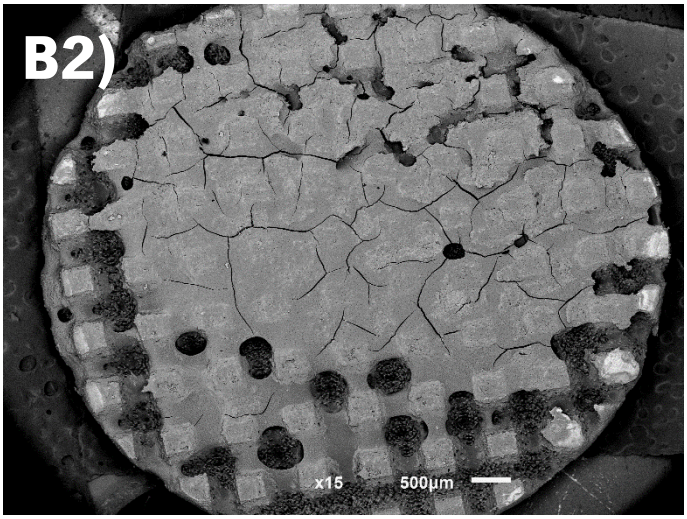
B2)
x15
500µm

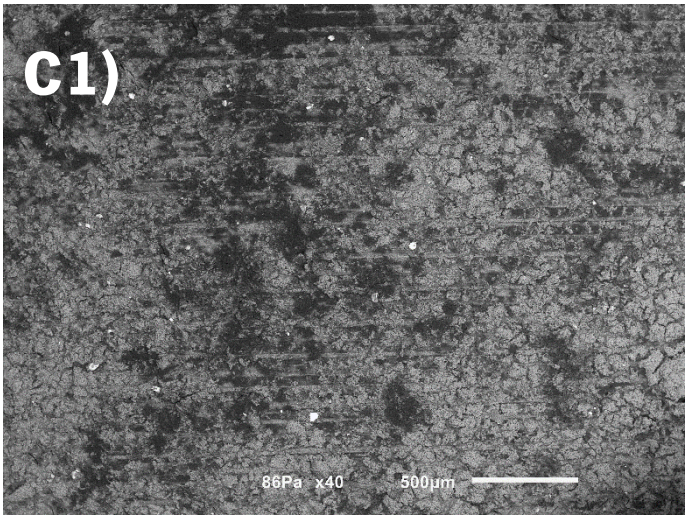
C1)
86Pa x40
500µm

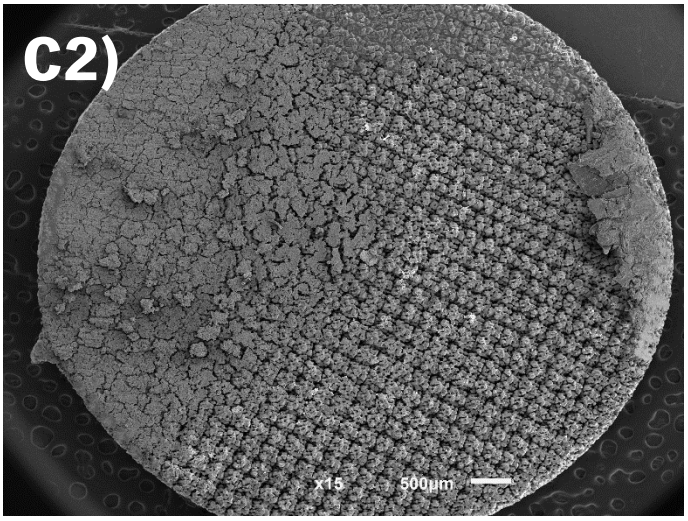
C2)
x15
500µm

d1)

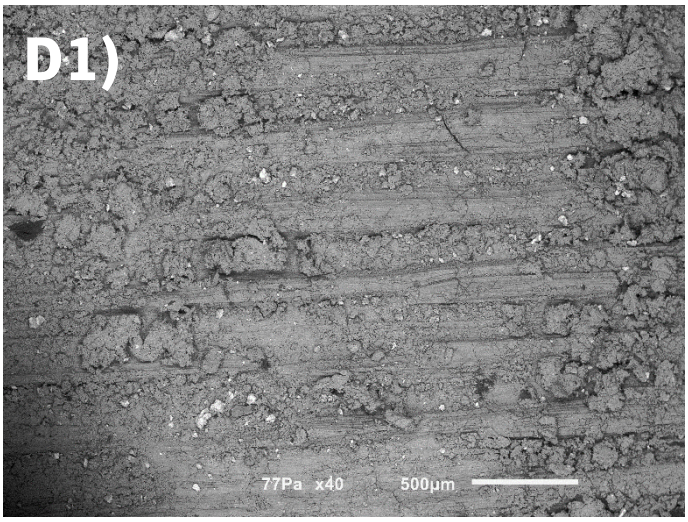
D1)
77Pa x40 500µm

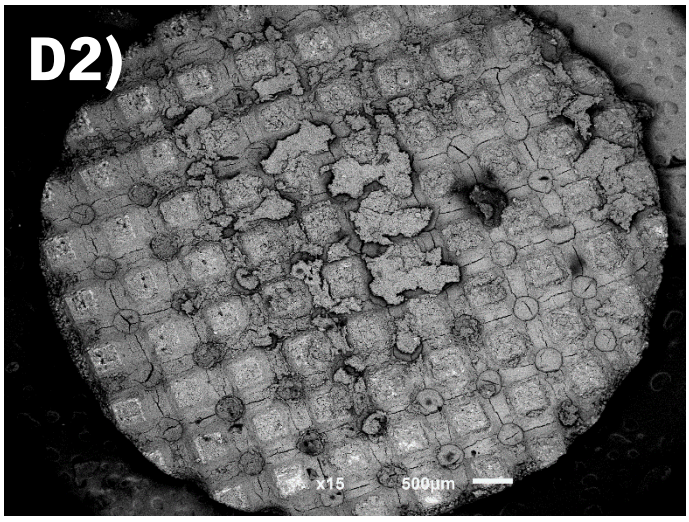
D2)
x15 500µm

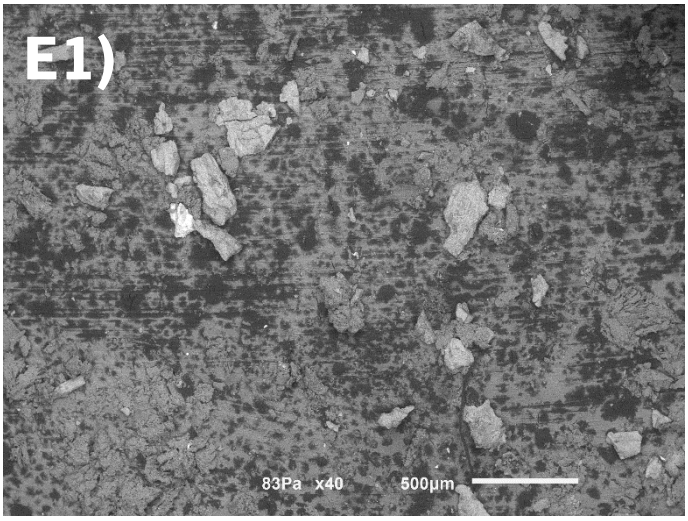
E1)
83Pa x40 500µm

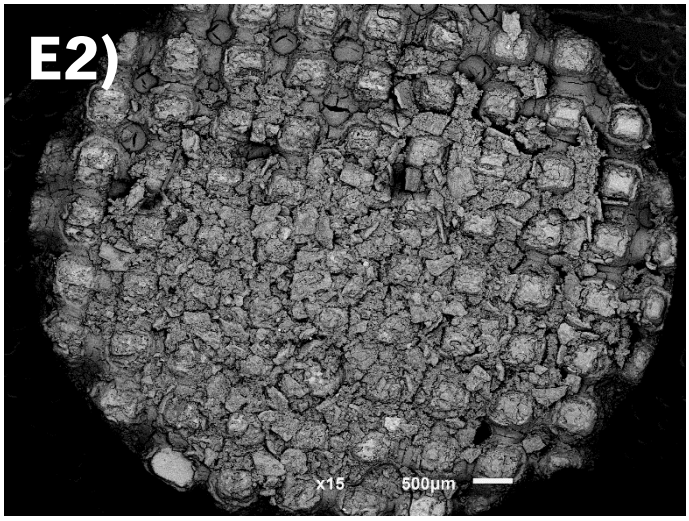
E2)
x15 500µm

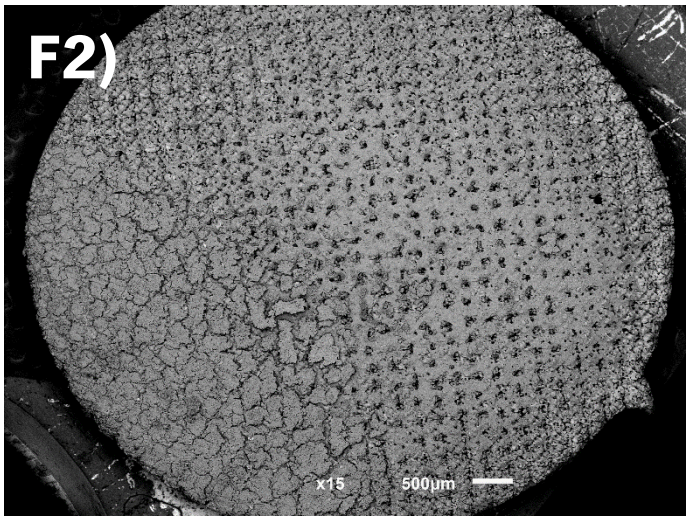
F2)
x15 500µm

d2)

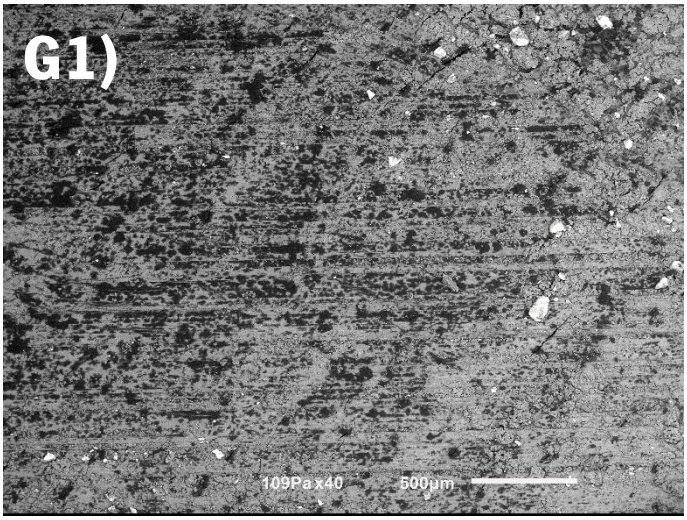

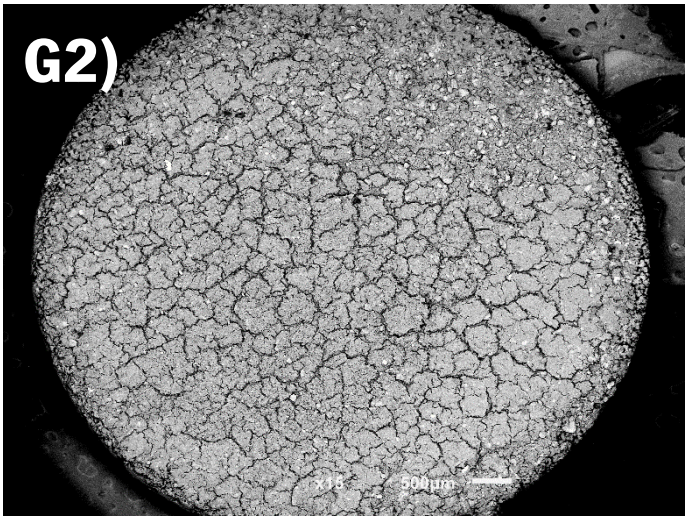

d3)